Study of collisional losses in the Large Hadron Collider for Pb-Pb and p-Pb operation

Tesi di Laurea Magistrale in
Nuclear Engineering - Ingegneria Nucleare

Author: **Alessandro Frasca**

CERN-THESIS-2022-294
/ /2022

Student ID: 943799
Advisor: Prof. Marco Beghi
Co-advisors: Roderik Bruce
Academic Year: 2021-22

To my parents and brother,
my guiding stars

Abstract

During about one month per operational year, the Large Hadron Collider (LHC) at CERN works as a heavy-ion collider. Fully-stripped lead ions ($^{208}Pb^{+82}$) are accelerated up to 7 Z TeV and brought into collision between themselves (Pb-Pb) or with protons (p-Pb). Four one-month Pb-Pb runs have been executed so far as well as two p-Pb runs. The LHC heavy-ion programme is scheduled to continue in the future, featuring increased luminosity and beam energy. Beam losses caused by ions fragmenting in the collision process risk introducing performance limitations. Most notably, when colliding Pb-Pb nuclei, the bound-free pair production (BFPP) causes a localized power deposition downstream of each interaction point (IP), which can induce beam dumps or the quench of superconducting magnets, hence imposing an upper limit on the luminosity. This work aims both at studying alleviations of BFPP losses at the LHCb experiment, as well as setting up a reliable simulation model that can be used to predict collisional losses in future operation. For the first time a full analysis of the BFPP losses at LHCb has been conducted, adopting the simulation code SixTrack. A partial mitigation strategy by means of orbit bumps, which do not require any new hardware to be installed in the LHC, has been proposed. It would allow to safely increase the levelled luminosity of LHCb by a factor 2-3 in future runs. A new simulation approach to simulate the losses arising around the LHC ring during Pb-Pb and p-Pb collisions has been presented and benchmarked. It relies on the SixTrack-FLUKA coupling to simulate the beam-beam collisions at the IPs and track the collision products. Collisional lossmaps have been simulated and compared to the measured data for both 2018 Pb-Pb and 2016 p-Pb runs. The simulation approach proposed has proven capable of providing results with an excellent agreement with experimental data and it can be considered a valid tool to estimate the beam losses for future operation. Consequently, the prediction of Pb-Pb and p-Pb master lossmaps for future runs has been provided, including in the simulation setup all the changes envisaged for the next machine configuration.

Keywords: accelerator physics, CERN, LHC, collider, luminosity, simulation

Abstract in lingua italiana

Ogni anno di funzionamento, per circa un mese, il Large Hadron Collider (LHC) del CERN è utilizzato per collidere ioni pesanti. Ioni di piombo completamente ionizzati ($^{208}Pb^{+82}$) sono accelerati fino a 7 Z TeV e fatti collider tra loro (Pb-Pb) o con protoni (p-Pb). Finora sono state eseguite quattro run Pb-Pb e due run p-Pb. Il programma a ioni pesanti dell'LHC proseguirà in futuro, con maggiori luminosità ed energia del fascio. Le perdite del fascio dovute alla frammentazione degli ioni nelle collisioni possono introdurre limitazioni nelle performance. In particolare, durante le collisioni Pb-Pb, la bound-free-pair-production (BFPP) causa una deposizione di potenza localizzata a valle di ciascun punto di interazione (IP) tale da indurre il dump del fascio o il quench dei magneti superconduttori, imponendo quindi un limite alla luminosità. Questo lavoro si propone di studiare le perdite da BFPP nell'esperimento LHCb, e di creare un modello di simulazione affidabile che possa essere utilizzato per prevedere le perdite collisionali in operazioni future. Per la prima volta è stata condotta un'analisi delle perdite da BFPP in LHCb, utilizzando il codice di simulazione SixTrack. È stata proposta una strategia di mitigazione parziale con orbit bumps, che non richiedono l'installazione di nuovo hardware nell'LHC. Essa consentirebbe di aumentare, senza rischi per la macchina, la luminosità livellata di LHCb di un fattore 2-3 nelle run future. Un nuovo approccio di simulazione, in grado di simulare le perdite che si verificano intorno all'anello dell'LHC durante le collisioni Pb-Pb e p-Pb, è stato presentato e validato. Questo consiste nell'accoppiare i codici SixTrack e FLUKA per simulare le collisioni tra i fasci negli IP e tracciare le traiettorie dei prodotti delle collisioni. Lossmaps collisionali sono state simulate e confrontate con quelle misurate per entrambe le run Pb-Pb del 2018 e p-Pb del 2016. L'approccio di simulazione proposto si è dimostrato in grado di fornire risultati con un eccellente accordo con i dati sperimentali e può essere considerato un valido strumento per predire le perdite del fascio in scenari futuri. Infine, le lossmaps collisionali per le future run Pb-Pb e p-Pb sono state stimate, includendo nel setup di simulazione tutte le modifiche previste per la futura configurazione dell'LHC.

Parole chiave: fisica degli acceleratori, CERN, LHC, collider, luminosità, simulazione

Contents

Introduction

Collisions of particles represent the main way to explore the structure of matter and extend our knowledge of its fundamental constituents and their interactions. The exploration of the sub-nuclear world requires probes with wavelengths of the order of 10^{-18} m, which correspond to energies of the order of TeV. Particle acceleration makes it possible to satisfy such demanding conditions. In this regard, a particle collider, an accelerator able to accelerate and collide two counter-propagating beams of particles, can work as a microscope for the sub-atomic space.

The Large Hadron Collider (LHC) [26], operated at the European Organization for Nuclear Research (CERN) since 2008, is the largest and highest-energy particle accelerator ever built. Along its circumference of 26.7 km, two counter-rotating beams of protons or ions can be accelerated up to a 7 Z TeV/c momentum, and then be brought into collision in the four experiments ATLAS [11], ALICE [8], CMS [30] and LHCb [3]. Here very sophisticated detectors measure the products originating from the collisions, which can reach a center-of-mass energy of up to 1.15 PeV for Pb ion head-on collisions.

In order to study any given physics process, it is desirable to maximize the number of occurring events and collect as much statistics as possible. With reference to the rate of events that can be produced, the performance of a collider is measured by the luminosity $\mathcal{L}$, which is defined as the ratio between the number of events N_{event} per unit time and the cross section of that event σ_{event}:

$$\mathcal{L} \equiv \frac{dN_{event}}{dt}\frac{1}{\sigma_{event}} \ . \tag{1}$$

The luminosity is a machine parameter, independent of the physical event, and in the LHC it has so far reached values of around $2 \times 10^{34}\mathrm{cm}^{-2}\mathrm{s}^{-1}$ for proton operation, and $6.1 \times 10^{27}\mathrm{cm}^{-2}\mathrm{s}^{-1}$ with Pb ions.

These operations are carried out making machine safety a priority: at 7 TeV a LHC nominal proton beam transports with a velocity $v \approx c$ about 360 MJ, the equivalent of 90 kg of TNT. An uncontrolled loss of even a small fraction of the beam could cause damage that would be very costly to recover, both in terms of money and downtime. Machine protection becomes even more critical due to the use of superconductive magnets, employed to generate the magnetic dipolar field of 8.3 T needed to steer the 7 Z TeV beams. The release of 10-20 mW cm^{-3} of power is sufficient to induce a magnet quench [64], i.e. its transition from superconductive to resistive state due to the increase of its temperature above a critical value [14]. If this happens, the beam must very quickly (within a few turns) be extracted ("dumped") before it is mis-steered by the breakdown of the field of the quenched magnet and causes damage to impacted elements. For these reasons, active and passive systems of protection are combined in the LHC to ensure safe operation.

Typically at the end of each operational year, for a month, fully stripped lead ions ($^{208}Pb^{+82}$) are accelerated and made to collide between themselves (Pb-Pb) or with protons (p-Pb) [25, 39]. One of the main purposes is that of recreating and studying the so-called quark-gluon plasma, a state of matter existed few millionths of a second after the Big Bang [8]. Pb-Pb physics runs have been executed in 2010, 2011, 2015 and 2018, whereas two full p-Pb runs took place, in 2013 and 2016. The next Pb-Pb run is scheduled for October 2023, during LHC Run 3, and will feature increased beam energy and luminosity with respect to past runs. A side effect of collisions of Pb-Pb or p-Pb is nuclear fragmentation or electron capture of the Pb ions, where the affected ions with altered charge-to-mass ratio risk to be lost on the aperture downstream of the collision point and trigger beam dumps or magnet quenches. This already gave rise to performance limitations in previous runs, especially in terms of luminosity [18, 39, 45, 62, 64], hence it is very important to study and quantify these beam losses.

This project consists in a study of collisional losses during LHC Pb-Pb and p-Pb operation. The coupling [5, 56, 66] of the two simulation codes SixTrack [2, 20, 59, 65] and FLUKA [6, 15, 36, 61] has been used to simulate the distribution of created ion fragments in Pb-Pb and p-Pb collisions, as well as their trajectories and loss positions. This procedure has been followed for each LHC experiment and both beams in order to reconstruct collisional lossmaps, i.e. the distribution of energy deposited by collision products all along the ring. Pb-Pb and p-Pb collisional lossmaps have been simulated and benchmarked with measured LHC data both for 2018 and 2016 operating conditions. This work therefore provides, for the first time, a well-benchmarked simulation tool that can be used to study collisional losses around the LHC ring in heavy-ion operation, applicable to future machine configurations. Consequently, a first estimate of the collisional losses for the coming heavy-ion runs is also presented.

In addition, a specific study has been carried out on the losses caused by the most dangerous collisional loss process for heavy ions, bound-free pair production (BFPP), in Pb-Pb collisions at the LHCb experiment. BFPP represents the main concern for maximizing LHCb luminosity, which in past runs was levelled to a safe value of 10^{27} cm^{-2}s^{-1} and should now be increased due to a recent request [25]. The BFPP losses have been simulated for past runs and compared to logged LHC data, and simulations have also been done to estimate these losses in future runs. A partial alleviation method has been proposed and studied, which does not require any new hardware to be installed in the LHC. It relies on the use of orbit bumps to shift the losses to a position where the power deposition is less dangerous. In simulation, the proposed method promises a significant increase of the LHCb luminosity, while still staying safe without quenching the impacted magnets. This is very important for the possibilities of fulfilling the future luminosity requests at LHCb.

To have a better understanding of the work presented in this thesis, the first three chapters will introduce the main context and concepts. In Chapter 1 a brief outline of the basic concepts of accelerator physics will be given, focusing on particle dynamics and beam losses; Chapter 2 will give an overview of the LHC accelerator and the LHC ion program in terms of its past achievements and future goals; Chapter 3 will feature a description of the main simulation tools used in the study. Finally, Chapters 4 and 5 will be dedicated to the main work carried out in this thesis and the results regarding the collisional losses for Pb-Pb and p-Pb, respectively.

1 | Basic accelerator physics

A particle accelerator is a machine built to accelerate particle beams for a specific purpose, e.g. experimental physics or biomedical or industrial applications. Every accelerator has its nominal trajectory that a particle beam will follow, guided by electromagnetic fields, and which is fixed by design. However, the motion of a particle inside an accelerator does never exactly correspond to that of the reference particle, i.e. the ideal particle with design momentum following the design trajectory. Small oscillations around reference particle trajectory instead characterize both transverse and longitudinal dynamics of particles inside a beam. Moreover, physical effects and imperfections can increase the transverse amplitude of the particle motion, eventually leading to particles being lost on the walls of the vacuum chamber. This chapter provides first a brief introduction on synchrotrons and circular colliders. Then, a basic description of transverse and longitudinal dynamics as well as the main beam loss mechanisms in circular machines are addressed. The contents of the following sections are based on the more detailed discussions found in [50, 52, 55, 58, 72, 73].

1.1. Circular colliders

Since the 1920s research on particle physics has been pushed by the use of particle accelerators. Several types of machines have been developed through the years, always with the main goal of achieving the maximum possible beam energy. The higher the energy, the smaller the constituents of matter that can be probed and the more the particles that can be produced. As known from the theory of relativity, the amount of energy E required to produce a particle of mass m is given by the fundamental relation

$$E = mc^2 \ , \tag{1.1}$$

where c is the speed of light.

The synchrotron is typically the accelerator-type that can reach the highest energies, in particular for the case of heavy particles that are not limited by synchrotron radiation.

Moreover, to have the highest centre-of-mass energy in the experiments, the idea was born of making two accelerated beams collide each other. This is what is pursued today in the so-called colliders. Before going into detail with the description of beam particle dynamics, it is appropriate to visualize how an accelerator is made. Since the LHC is both a synchrotron and a circular collider, the working principles of these machines will be explained below.

1.1.1. Forces used in particle acceleration

Particle motion inside an accelerator is controlled by means of electromagnetic fields. In the presence of an electromagnetic field, a particle of charge q is subject to the Lorentz force

$$\vec{F} = q(\vec{E} + \vec{v} \times \vec{B}) \ . \tag{1.2}$$

The gain in energy ΔE of a particle moving from $\vec{r}_1$ to $\vec{r}_2$ is given by the work done on it by the Lorentz force:

$$\Delta E = \int_{\vec{r}_1}^{\vec{r}_2} \vec{F} \cdot d\vec{r} = q \int_{\vec{r}_1}^{\vec{r}_2} (\vec{E} + \vec{v} \times \vec{B}) \cdot d\vec{r} = q \int_{\vec{r}_1}^{\vec{r}_2} \vec{E} \cdot d\vec{r} \ . \tag{1.3}$$

As Eq. (1.3) shows, only the electric field $\vec{E}$ is responsible for energy transfer to particles since the vector $\vec{v} \times \vec{B}$ is always perpendicular to the direction of motion and hence $(\vec{v} \times \vec{B}) \cdot d\vec{r} = 0$. The magnetic field $\vec{B}$ instead provides a centripetal force which can be used to guide particles along a trajectory. Considering a constant and uniform magnetic field, i.e. the first term of the multipole expansion of magnetic field, perpendicular to the direction of motion of a particle, then it experiences a force equal to the expression of the centripetal force:

$$qvB = \frac{mv^2}{\rho} \ , \tag{1.4}$$

where m is the mass of the charged particle and ρ is the radius of curvature of its trajectory. Equation (1.4) leads to the expression of **magnetic rigidity** $B\rho$

$$B\rho = \frac{p}{q} \ , \tag{1.5}$$

where p is the particle momentum.

Put simply, in an accelerator the electric field is used to give energy to the particles, whereas the magnetic field is used to bend and focus the beam.

1.1.2. The synchrotron

The compact design of early circular accelerators, such as the cyclotron or the betatron, shows some limitations to the maximization of beam energy [73]. From Eq. (1.5) it follows that for a relativistic particle ($E \approx pc$)

$$\rho \approx \frac{E}{qcB} \ , \tag{1.6}$$

which states that the orbit radius ρ is proportional to the energy E and inversely proportional to the magnetic field of bending B.

Since there are technological limits to the maximum value of magnetic field that can be achieved, typically in an accelerator it does not exceed 10 T. Even for this value, already at energies larger than few GeV the orbit radius reaches several meters, and in practice it is difficult to manufacture a magnet of this size. To cope with the necessity of increasing beam energy, the concept of synchronous acceleration with phase stability was simultaneously developed in 1944 by E.M. McMillan (University of California) and V. Veksler (Soviet Union). The working principle consists in keeping the particles on a well-defined orbit with fixed radius by increasing the magnetic field synchronously to the increase in beam energy, i.e. maintaining the ratio $\frac{E}{B}$ constant. This allows to use narrow bending magnets placed along the design orbit. This type of circular accelerator is called **synchrotron**. Its essential elements, shown in Fig. 1.1, are the following:

- bending magnets to steer the beam along a circular orbit;
- focusing magnets to compensate the unavoidable divergence the beam gains turn after turn;
- RF cavities to accelerate the beam once a revolution: their frequency f_{RF} has to increase synchronously to the increase in revolution frequency f_{rev} so that the reference particle encounters the same phase of the accelerating field at each turn, and particles cluster around it. A beam accelerated by an RF voltage is always a bunched beam;
- injection and extraction magnets to deflect on the orbit the incoming beam from a pre-accelerator (synchrotrons cannot accelerate a beam from scratch) and to extract it at the end of a cycle, respectively.

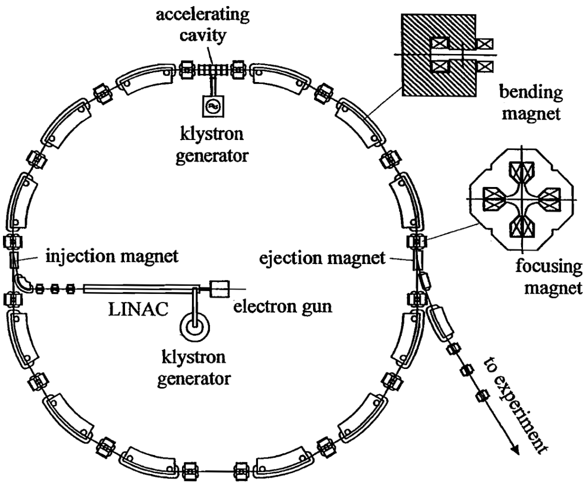

Figure 1.1: Scheme of a synchrotron [73].

1.1.3. The circular collider

The idea of colliders was born to push to the limit the center-of-mass energy when realizing experiments with accelerated beams. The center-of-mass energy reads

$$E_{CM} = \sqrt{(E_1 + E_2)^2 - (\vec{p}_1 + \vec{p}_2)^2} \, , \tag{1.7}$$

where the sub-scripts 1 and 2 refer to the projectile and to the target respectively. Then, if the target is a counter propagating beam with momentum $\vec{p}_2 = -\vec{p}_1$ and energy $E_2 = E_1 = E$, the center-of-mass energy reaches its maximum value

$$E_{CM} = E_1 + E_2 = 2E \; . \tag{1.8}$$

In a circular collider, typically a synchrotron, two counter rotating beams are accelerated up to the target energy, and then made to collide at interaction points (IPs). Each IP is surrounded by particle detectors, which almost cover all the solid angle, to collect as many interaction products as possible for further analysis. Equation (1) states that the event rate of a specific process is given by $\frac{dN_{event}}{dt} = \sigma_{event}\mathcal{L}$. The value of σ_{event} is fixed by the laws of nature, so the only way to increase the event rate is increasing the luminosity $\mathcal{L}$. This is a machine parameter independent of the physical interaction. It is proportional to the overlap integral of the two bunches crossing each other, to the number of bunches n_b and to the revolution frequency f_{rev}. In the simplest case of Gaussian distributions and head-on collisions without a crossing angle, the luminosity is given by

$$\mathcal{L} = \frac{N_1 N_2 f_{rev} n_b}{4\pi\sigma_x\sigma_y} , \tag{1.9}$$

where N_1 and N_2 are the numbers of particles per bunch and σ_x and σ_y are the horizontal and vertical transverse dimensions of the beam.
A reduction of the σ_x and σ_y is typically performed around the interaction points to increase luminosity as much as possible. Actually, at each beam crossing, generally only few particles undergo head-on collisions and thus the beam intensities are only slowly reduced by the collisions. The same beams can continue circulating while crossing at the interaction regions for a long time, allowing data taking for several hours.

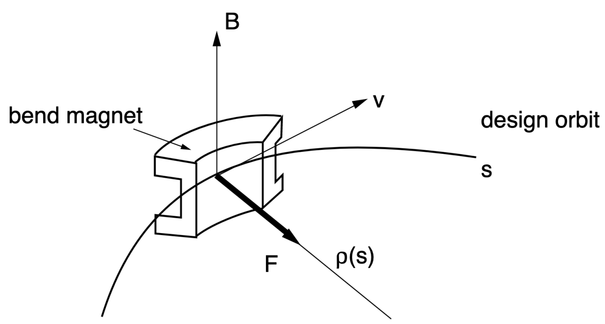

(a) Vertical dipole magnet.

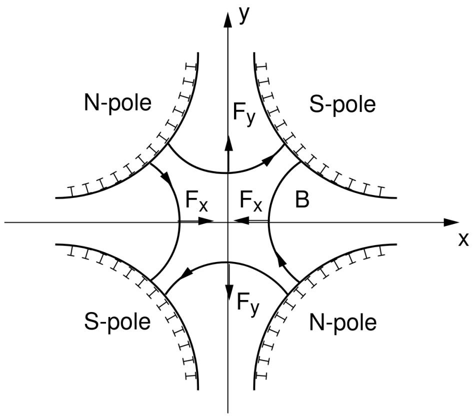

(b) Horizontally focusing quadrupole magnet.

Figure 1.2: Forces exerted on a positive charge by a dipole and a quadrupole magnet [55].

1.2. Transverse dynamics

In circular accelerators such as synchrotrons, vertical dipole magnets bend the beam trajectory along the circumference, defining the closed orbit. Beam particles circulate close to this path revolution after revolution, but they unavoidably deviate from the nominal trajectory. The restoring force needed to steer diverging particles back onto the closed orbit is given by quadrupole magnets. A quadrupole magnet produces, in both horizontal and vertical plane, a magnetic field which is zero at the centre and increases linearly as function of the distance from its centre, causing a focusing effect in one plane and a defocusing effect in the other. It can be demonstrated that the sequence of two quadrupole magnets with opposite polarities has a focusing effect on both planes [72].

For this reason, horizontally focusing and defocusing magnets are alternated along the accelerator magnet sequence, which is called lattice, in order to perform the so-called strong focusing.

Transverse dynamics is characterized by the horizontal and vertical oscillation of particles around the design orbit due to the restoring forces exerted by magnets along the lattice. The physical principles of beam steering and focusing by means of magnetic fields are called **beam optics**, by analogy with light.

1.2.1. Equations of motion

The description of beam particle transverse dynamics will be presented for an accelerator in steady state condition, in which neither beam injection nor extraction nor acceleration is occurring. We consider a right-handed orthogonal system $K(x, y, z)$ whose origin moves with the reference particle along the design orbit, described by the variable s (Fig. 1.3). The axis $\vec{z}$ gives the beam direction, whereas x and y are the horizontal and vertical coordinates respectively. The equations for the transverse dynamics can be derived from the equation of motion

$$\vec{F} = \frac{d\vec{p}}{dt} = q(\vec{E} + \vec{v} \times \vec{B}) \ , \tag{1.10}$$

with

$$\vec{p} = m\gamma\vec{v} \ , \tag{1.11}$$

where m is the particle rest mass and γ is the relativistic Lorentz factor.
The condition of no acceleration implies a zero electric field $\vec{E} = 0$ and constant v and γ.

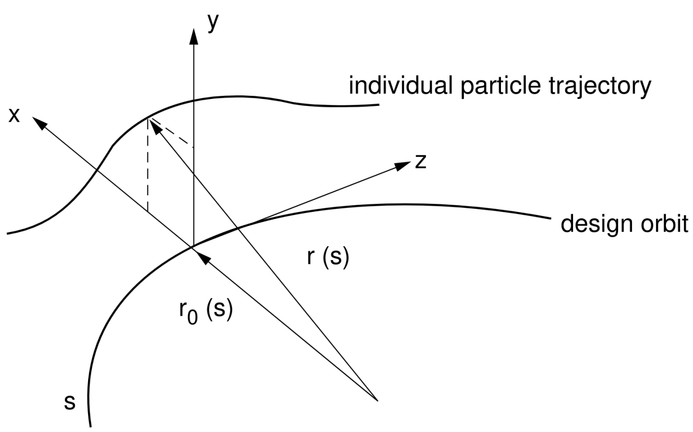

Figure 1.3: Coordinate system comoving with reference particle [55].

Thus, Eq. (1.10) becomes

$$\frac{d\vec{p}}{dt} = m\gamma\frac{d\vec{v}}{dt} = m\gamma\frac{d^2\vec{r}}{dt^2} = q(\frac{d\vec{r}}{dt} \times \vec{B}) \ . \tag{1.12}$$

The magnetic field $\vec{B}$ is assumed to have only transverse components, i.e. $\vec{B} = (B_x, B_y, 0)$, as it is usually found in a particle accelerator. For small deviations from the design orbit, the field components can be expanded in series up to the first order, which means taking into account only dipole and quadrupole terms:

$$\begin{aligned} B_x(x,y,s) &= B_{x0} + \frac{\partial B_x}{\partial x}x + \frac{\partial B_x}{\partial y}y \ , \\ B_y(x,y,s) &= B_{y0} + \frac{\partial B_y}{\partial x}x + \frac{\partial B_y}{\partial y}y \ . \end{aligned} \tag{1.13}$$

The magnetic field satisfies the Maxwell equations

$$\nabla \cdot \vec{B} = 0 \qquad\qquad \nabla \times \vec{B} = 0 \ , \tag{1.14}$$

from which it follows:

$$\frac{\partial B_x}{\partial x} = -\frac{\partial B_y}{\partial y} \qquad\qquad \frac{\partial B_x}{\partial y} = \frac{\partial B_y}{\partial x} \ . \tag{1.15}$$

As further hypothesis it is assumed that there are no skew linear magnets in the machine, i.e. there is no linear coupling between the motion in the two transverse planes, and thus $\frac{\partial B_x}{\partial x} = -\frac{\partial B_y}{\partial y} = 0$. Moreover, in an accelerator deflecting the beam only in the horizontal plane, the dipole term of horizontal field component B_{x0} is null. The magnetic field components in (1.13) then become

$$\begin{aligned} B_x(x,y,s) &= \frac{\partial B_y}{\partial x}y \ , \\ B_y(x,y,s) &= B_{y0} + \frac{\partial B_y}{\partial x}x \ . \end{aligned} \tag{1.16}$$

Equation (1.12) can be transformed, using the distance s along the reference orbit as independent variable instead of the time. The relation is uniquely defined for each instant t. Retaining only the linear terms in x, $x' = \frac{dx}{ds}$, y, $y' = \frac{dy}{ds}$ and $\delta = \frac{p-p_0}{p_0}$, the linearized equations of motion are retrieved:

$$x'' + \left(\frac{1}{\rho(s)^2} + k(s)\right)x = \frac{\delta}{\rho(s)} \ , \tag{1.17}$$

$$y'' - k(s)y = 0 \ , \tag{1.18}$$

with
$$\rho = \frac{p_0}{qB_{y0}} \; , \quad k = \frac{q}{p_0}\left(\frac{dB_y}{dx}\right)_{x=0,\; y=0} \; ,$$
where p_0 is the design momentum.
Equations (1.17) and (1.18) are the basis of calculations in linear beam optics. They describe two uncoupled quasi-harmonic oscillations around the orbit, where the forces exerted by the magnet structure of the machine act like restoring forces for the diverging particles. The vertical dipole magnets contribute with a focusing function $\frac{1}{\rho^2}$ only in the horizontal motion, whereas the quadrupole magnets provide a focusing gradient k in both planes but with an opposite effect. It can be noticed that the equation for the horizontal motion is inhomogeneous, showing a term proportional to the fractional momentum offset δ. This comes from the different bending that off-momentum particles experience with respect to the reference particle inside a dipole, because of their different magnetic rigidity—see Eq. (1.5). In other words, the term $\frac{\delta}{\rho(s)}$ accounts for the different closed orbit followed by an off-momentum particle.

1.2.2. Betatron oscillations

We first consider the solutions of the equations of motion for a particle with design momentum ($\delta = 0$). Equations (1.17) and (1.18) can be rewritten in the more general form
$$u'' + K(s)u = 0 \; , \tag{1.19}$$
where u can be x or y and $K(s) = \rho^{-2}(s) + k(s)$ or $K(s) = -k(s)$.
Around an accelerator the focusing functions vary with the elements of the lattice, but are generally periodic with L, where L is the lattice period. In a circular accelerator the lattice period can be identified with its circumference C. Equation (1.19) with periodic $K(s) = K(s+L)$ is called **Hill's equation**. Its general solution is a pseudo-harmonic oscillation [55]
$$u(s) = a\sqrt{\beta(s)}\; \cos\left[\mu(s) + \phi\right] \; , \tag{1.20}$$
with varying amplitude and frequency.
In the context of beam optics this oscillation is called **betatron oscillation** from the name betatron function associated to $\beta(s)$. It is a periodic function, satisfying $\beta(s+L)$=$\beta(s)$, as defined by the focusing properties of the lattice. The phase advance $\mu(s)$ is given by
$$\mu(s) = \int_{s_0}^{s} \frac{dt}{\beta(t)} \; , \tag{1.21}$$

whereas a and ϕ are integration constants that depend on the initial conditions at s_0.
In a circular machine it is possible to define the betatron tune Q, which is the number of betatron oscillations performed by a particle in a turn. It is given by

$$Q = \frac{1}{2\pi}\int_{s}^{s+C}\frac{dt}{\beta(t)} \ . \tag{1.22}$$

As will be discussed more in detail in Sec. 1.4, the knowledge of betatron tune values of both transverse planes and their control are of fundamental importance for beam stability. Starting from the betatron function $\beta(s)$, two other functions can be defined:

$$\alpha(s) = -\frac{\beta'(s)}{2} \ , \tag{1.23}$$

$$\gamma(s) = \frac{1+\alpha(s)^2}{\beta(s)} \ . \tag{1.24}$$

The variables $\alpha(s)$, $\beta(s)$ and $\gamma(s)$ are called **Twiss parameters** and they completely define the linear optics of an accelerator. Beside the solution (1.20), its first derivative $u' = \frac{du}{ds}$ is needed for a full description of the transverse motion:

$$u'(s) = -\frac{a}{\sqrt{\beta(s)}}\big(\alpha(s)\cos\left[\mu(s)+\phi\right] + \sin\left[\mu(s)+\phi\right]\big) \ . \tag{1.25}$$

Since the small-angle approximation can be considered valid, $u'(s)$ represents the angle between the direction of particle motion and the design trajectory. The evolution of u and u' along the accelerator lattice can be formulated through the transfer-matrix formalism. If the position u_0 and the angle u'_0 are known at an initial location s_0, the transfer-matrix $\mathbf{M}(s_0|s)$ allows to compute u, u' at any other location s. The transfer-matrix can be derived expressing the constants a and ϕ in (1.20) and (1.25) as functions of u_0 and u'_0. As a result, the solutions of transverse motion can be rewritten in matrix form

$$\begin{pmatrix} u(s) \\ u'(s) \end{pmatrix} = \mathbf{M}(s_0|s)\begin{pmatrix} u_0 \\ u'_0 \end{pmatrix} \ , \tag{1.26}$$

with [55]

$$\mathbf{M}(s_0|s) =$$
$$= \begin{pmatrix} \sqrt{\frac{\beta(s)}{\beta_0}}\left(\cos\Delta\mu(s) + \alpha_0 \sin\Delta\mu(s)\right) & \sqrt{\beta(s)\beta_0}\sin\Delta\mu(s) \\ \frac{\alpha_0-\alpha(s)}{\sqrt{\beta(s)\beta_0}}\cos\Delta\mu(s) - \frac{1+\alpha(s)\alpha_0}{\sqrt{\beta(s)\beta_0}}\sin\Delta\mu(s) & \sqrt{\frac{\beta_0}{\beta(s)}}\left(\cos\Delta\mu(s) - \alpha(s)\sin\Delta\mu(s)\right) \end{pmatrix} , \tag{1.27}$$

where α_0, β_0 are the Twiss parameters at s_0 and $\Delta\mu(s)$ is the phase advance between s_0 and s.
The transverse motion of a particle can be studied in the phase space (u, u'). Manipulating the expressions for u (1.20) and u' (1.25) the following equation can be obtained

$$\gamma(s)u(s)^2 + 2\alpha(s)u(s)u'(s) + \beta(s)u'(s)^2 = a^2 \ . \tag{1.28}$$

Equation (1.28) is the parametric representation of an ellipse in the plane (u, u'). As shown in Fig. 1.4, the shape and the orientation of the ellipse are determined by the Twiss parameters at the location s and change together with them as a particle moves along the orbit. The area enclosed by the ellipse, given by πa^2, is instead a constant of motion identified as the single-particle **emittance** ϵ

$$\iint_{ellipse} du du' \equiv \pi\epsilon \ , \tag{1.29}$$

from which $a = \sqrt{\epsilon}$.
Thus the maximum betatron amplitude is $\sqrt{\beta\epsilon}$ and the maximum angle is $\sqrt{\gamma\epsilon}$. The results shown so far hold for a single particle, whereas a beam is composed of many particles distributed in phase space, each with its own phase plane ellipse. In an accelerator they usually have a Gaussian distribution in both position and angle, whose standard deviation defines the emittance of the entire beam. For instance, the distribution in position of N particles in the horizontal transverse plane has the well-known expression

$$\rho_{Gaussian}(x) = \frac{N}{\sqrt{2\pi}\sigma_x} e^{-\frac{x^2}{2\sigma_x^2}} \ , \tag{1.30}$$

where $\sigma_x = \sqrt{\epsilon_x \beta_x}$ represents the horizontal envelope of the beam and $\epsilon_x = \frac{\sigma_x^2}{\beta_x}$ is the beam emittance in (x, x') plane, which identifies an ellipse containing 68.3% of the particles.

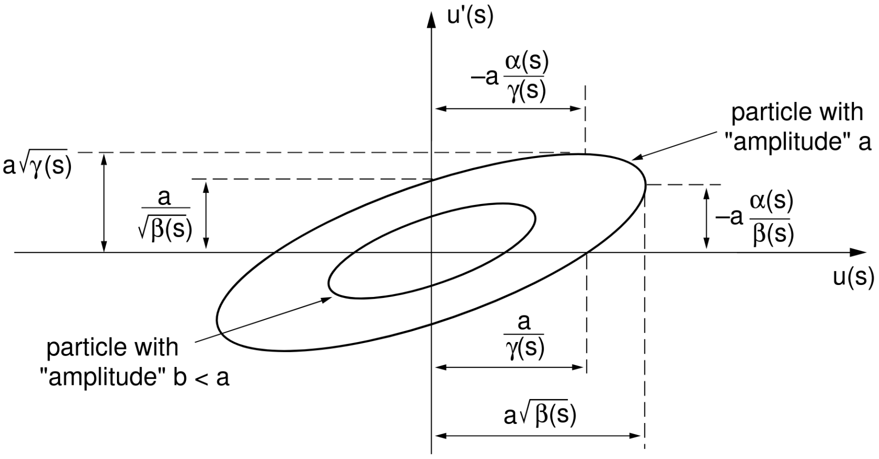

Figure 1.4: Phase space ellipses for particles with different amplitudes [55].

It can be shown that removing the hypothesis of no acceleration the emittance ϵ is no more a constant of motion. Liouville's theorem from Hamiltonian mechanics states that every volume in phase space is constant in time if particles obey the canonical equations of motion. Even though this condition is generally satisfied in accelerators, the theorem does not hold for the ellipse in (u, u') plane since u and u' are not canonically conjugated variables. It can instead be applied to x and p_x or y and p_y, for example:

$$\iint dx dp_x = const \ . \tag{1.31}$$

The angle x' can be expressed as

$$x' = \frac{dx}{ds} = \frac{dx}{dt}\frac{dt}{ds} = \frac{p_x}{p_s} \simeq \frac{p_x}{p_0} \ , \tag{1.32}$$

where $p_0 \simeq p_s$ holds because of the small-angle approximation.
Using (1.32), the integral (1.31) can be transformed into

$$p_0 \iint dx dx' = const \ , \tag{1.33}$$

from which

$$\epsilon_x = \frac{const}{p_0} = \frac{const}{mc\gamma_0\beta_0} = \frac{const}{\gamma_0\beta_0} \ , \tag{1.34}$$

where γ and β are the relativistic factors, not to be confused with twiss parameters. Equation (1.34) shows that if acceleration is occurring, then β and γ increase and ϵ_x is not constant anymore: as the energy of the beam increases ϵ_x decreases and its transverse size shrinks. Thus it is useful to define the so-called **normalized emittance**, which is conserved even during acceleration:

$$\epsilon_n = \epsilon\gamma\beta \ . \tag{1.35}$$

1.2.3. Dispersion

We now consider a particle with a momentum $p = p_0 + \Delta p$ different from the design momentum p_0 ($\delta \neq 0$). The equation for the vertical plane (1.18) is unchanged, whereas the equation for the horizontal plane (1.17) reads

$$x'' + K(s)x = \frac{\delta}{\rho(s)} \ , \tag{1.36}$$

where $K(s) = \rho^{-2}(s) + k(s)$.
The solution to Eq. (1.17) is given by the sum of two functions

$$x(s) = x_\beta(s) + x_\delta(s) \ , \tag{1.37}$$

where $x_\beta(s)$ is the solution to the homogeneous equation, already discussed in Subsec. 1.2.2, and $x_\delta(s)$ is a particular solution to the inhomogeneous one (1.36). The solution $x_\delta(s)$ is usually rewritten as

$$x_\delta(s) = D(s)\delta \ , \tag{1.38}$$

where $D(s)$ is a function called **dispersion** which satisfies the equation

$$D'' + K(s)D = \frac{1}{\rho(s)} \ . \tag{1.39}$$

The dispersion function $D(s)$ quantifies the horizontal shift from the design orbit for a unitary fractional off-momentum deviation $\delta = \frac{\Delta p}{p_0} = 1$. Therefore, the solution $x_\beta(s)$ describes betatron oscillations around the shifted off-momentum orbit. In matrix form the solutions for the horizontal transverse plane become

$$\begin{pmatrix} x(s) \\ x'(s) \end{pmatrix} = \mathbf{M}(s_0|s) \begin{pmatrix} x_0 \\ x'_0 \end{pmatrix} + \delta \begin{pmatrix} D(s) \\ D'(s) \end{pmatrix} \ . \tag{1.40}$$

The additional transverse shift in position given by dispersion evidently changes the size of the beam, which now depends on both $\beta(s)$ and $D(s)$:

$$\sigma_x = \sqrt{\beta_x(s)\epsilon_x + D(s)^2\left(\frac{\Delta p}{p_0}\right)^2_{beam}} \ , \tag{1.41}$$

where $\left(\frac{\Delta p}{p_0}\right)_{beam}$ is the standard deviation δ, called the momentum spread of the beam.

1.3. Longitudinal dynamics

As introduced in the previous section and shown in Eq. (1.3), only the electric field is responsible for particle acceleration. Therefore every accelerator has its system that provides a longitudinal electric field to increase particle momentum. Since the use of static electric fields presents great limits to the maximum beam energy that can be achieved, high-frequency voltages are preferred. In all modern accelerators radio-frequency structures (RF) are used to generate strong electric fields of the order of MV/m with a frequency ranging from hundreds of MHz to several GHz. In a circular accelerator, particles pass through the same RF cavities every turn, receiving a boost in energy equal to

$$\Delta E = qV \sin\varphi = qV \sin\left(\omega_{RF} t\right) \ , \tag{1.42}$$

where V is the maximum amplitude of RF accelerating voltage, ω_{RF} is the RF voltage angular frequency, and φ is the phase seen by the particle.
In order to ensure that particles always see an accelerating voltage at the gap, the RF frequency f_{RF} must be an integer multiple of the revolution frequency:

$$f_{RF} = h f_{rev} \ , \tag{1.43}$$

where h is an integer called **harmonic number**.
The synchronism between the passage of beam particles and the RF oscillation is crucial to obtain the desired increase in energy. This is of fundamental importance in synchrotrons, where the energy gain per turn must fit the increase of magnetic field to keep the bending radius ρ constant and maintain the accelerating particles on the same fixed orbit. The phase φ_s fulfilling this condition is called **stable phase** and it is given by

$$\sin\varphi_s = 2\pi\rho R \frac{\dot{B}}{V} \ , \tag{1.44}$$

where $\dot{B}$ is the time derivative of magnetic field and R is the average radius of accelerator circumference.

In principle both φ_s and $\pi - \varphi_s$ satisfy Eq. (1.44) but, as it will be explained in the following sub-section, only one of them represents a stable value of phase. The ideal particle arriving each turn at the same stable phase is called a **synchronous particle**. Longitudinal dynamics is characterized by the longitudinal oscillation of particles due to the fluctuation of their phase around the stable one turn after turn, which is also linked to an oscillation in energy around the ideal one.

1.3.1. Phase stability

The principle of phase stability ensures that the circulating particles are always accelerated with a fixed average phase of the RF voltage, i.e. the stable phase, so that they do not spread around the accelerator but instead form a bunch around the synchronous particle. As the beam particles do not all reach the accelerating cavity at the same instant, they each encounter a slightly different RF voltage phase and hence experience a different momentum change. This shift in momentum has two main effects on a particle: not only it will have a different velocity but it will also circulate on an off-momentum orbit with a different length. The relative orbit length change for a given relative momentum change is given by the **momentum compaction factor**

$$\alpha_c \equiv \frac{\Delta C/C}{\Delta p/p} = \frac{1}{C} \oint \frac{D(s)}{\rho(s)} ds \ . \tag{1.45}$$

Since a positive shift in momentum implies a longer orbit travelled at higher velocity, it is not straightforward to state whether this increases or decreases the revolution frequency f_{rev}. For instance, let us assume a group of non-relativistic particles, where the increase in velocity dominates over the increase in path length. In such conditions, a positive shift in momentum leads to a higher revolution frequency, and vice-versa. The situation is illustrated in Fig. 1.5, where two synchronous particles P_1 and P_2 are located at the phases φ_s and $\pi - \varphi_s$ of the sinusoidal RF voltage, respectively. They are ideal on-momentum particles ($\frac{\Delta p}{p_0} = 0$), experiencing the same energy gain every turn. M_1, N_1, M_2 and N_2 represent instead the particles distributed around them. The particle M_1 had a higher momentum ($\frac{\Delta p}{p_0} > 0$) and arrived at the cavity somewhat earlier, with a smaller phase $\varphi < \varphi_s$. This turn it sees a smaller voltage and gains less energy: its revolution frequency will decrease and it will again move closer to the synchronous particle P_1. The opposite happens to the particle N_1, arriving later because of its smaller momentum ($\frac{\Delta p}{p_0} < 0$). It sees a higher voltage and gains more energy, getting closer to the synchronous particle as

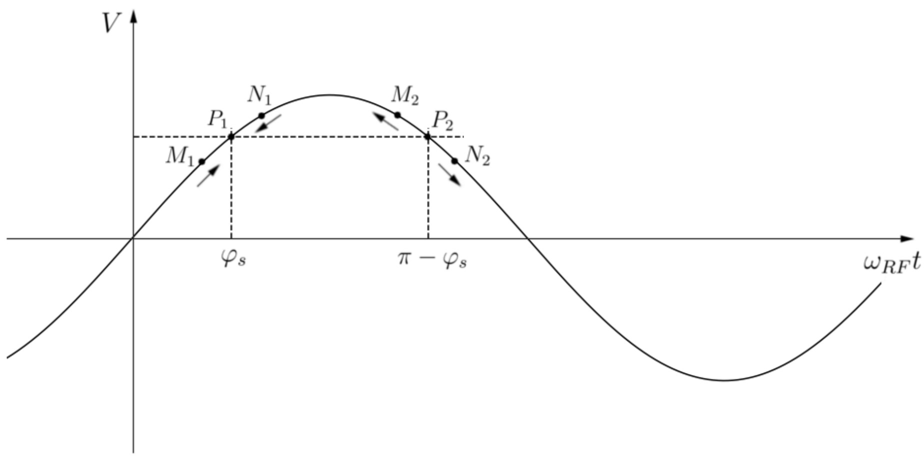

Figure 1.5: Schematics of the principle of phase stability for an accelerator below transition.

well. This is not the case for the particles distributed around the phase $\pi - \varphi_s$. The faster particle M_2 arrived with a smaller phase $\varphi < \pi - \varphi_s$ and will gain even more energy this turn, getting further and further from P_2. Similarly, the slower particle N_2 will depart from the synchronous particle because of its lower and lower revolution frequency.

It is clear that the two phases φ_s and $\pi - \varphi_s$ are not equivalent and that the stable phase must be chosen adequately depending on how the revolution frequency changes for a given momentum change. This is expressed by the **slip factor**

$$\eta \equiv \frac{df_{rev}/f_{rev}}{dp/p_0} = \frac{1}{\gamma_0^2} - \alpha_c \ , \tag{1.46}$$

where γ_0 is the relativitic Lorentz factor of the synchronous particle.
The energy giving a value of $\gamma = \frac{1}{\sqrt{\alpha_c}} \equiv \gamma_t$ is called **transition energy** and divides the longitudinal motion into two regimes. Below the transition energy ($\gamma < \gamma_t, \eta > 0$) the increase in velocity dominates over the increase in path length, hence a higher momentum implies a higher revolution frequency. The above example corresponds to this case, where φ_s is the stable phase around which phase focusing can be performed. Above the transition energy ($\gamma > \gamma_t, \eta < 0$) particle velocity approaches speed of light and thus the increase in velocity is less and less significant. In this regime a higher momentum corresponds to a lower revolution frequency and the stable phase is instead $\pi - \varphi_s$. Some machines work only below or above transition, whereas others cross the transition during acceleration. The moment of transition is delicate since the RF must perform a rapid change of phase, called phase jump, so that the beam can come across the new stable phase $\pi - \varphi_s$.

1.3.2. Synchrotron oscillations

The periodic longitudinal particle motion around the stable phase is called **synchrotron oscillation**. The particles keep oscillating and changing their phase φ and their relative momentum offset δ. In order to give a quantitative description of this oscillation, we relate phase difference of a particle with respect the synchronus one $\Delta\varphi = \varphi - \varphi_s$ to the difference in their momentum gain at the RF. The phase difference can be expressed in terms of difference in revolution frequency:

$$\begin{aligned} \frac{d\Delta\varphi}{dt} &= -2\pi h \Delta f_{rev} \ , \\ \frac{d^2\Delta\varphi}{dt^2} &= -2\pi h \frac{d\Delta f_{rev}}{dt} \ . \end{aligned} \tag{1.47}$$

The increase in momentum can be derived from the energy gain per turn (1.42), using the relation $dE = vdp$ with $v = 2\pi R/T_{turn}$:

$$\Delta E = 2\pi R \frac{dp}{dt} = qV \sin\varphi \ . \tag{1.48}$$

The difference in momentum gain between a particle and the synchronous one can be written as

$$2\pi R \frac{d\Delta p}{dt} = qV(\sin\varphi - \sin\varphi_s) \ . \tag{1.49}$$

Using the definition of slip factor η,

$$\frac{d\Delta f_{rev}}{dt} = \eta \frac{f_{rev}}{p_0} \frac{d\Delta p}{dt} = \frac{\eta f_{rev}}{2\pi R p_0} qV(\sin\varphi - \sin\varphi_s) \ , \tag{1.50}$$

Eq. (1.47) can be transformed into

$$\frac{d^2\Delta\varphi}{dt^2} = -\frac{\eta h f_{rev}}{R p_0} qV(\sin\varphi - \sin\varphi_s) \ . \tag{1.51}$$

This second-order non-linear differential equation describes the synchrotron motion. For very small deviations from the stable phase, i.e. $\Delta\varphi \to 0$, the term $(\sin\varphi - \sin\varphi_s)$ can be simplified as follows

$$\begin{aligned} \sin(\Delta\varphi + \varphi_s) - \sin\varphi_s &= \sin\Delta\varphi\cos\varphi_s + \cos\Delta\varphi\sin\varphi_s - \sin\varphi_s = \\ &\simeq \Delta\varphi\cos\varphi_s + \sin\varphi_s - \sin\varphi_s = \Delta\varphi\cos\varphi_s \ , \end{aligned} \tag{1.52}$$

and Eq. (1.51) can be linearized to an equation of a harmonic oscillator

$$\frac{d^2\Delta\varphi}{dt^2} + \Omega_s^2\Delta\varphi = 0 \ , \tag{1.53}$$

with angular frequency

$$\Omega_s = \sqrt{\frac{\eta f_{RF}\cos\varphi_s}{Rp_0}qV} \ . \tag{1.54}$$

The conditions for phase stability, already expressed qualitatively in the previous subsection, are implicitly included in the expression of the synchrotron frequency Ω_s. A stable oscillation requires the quantity under the square root to be larger than zero and thus $\eta \cdot \cos\varphi_s > 0$. The two regimes are then retrieved:

below transition $\eta > 0 \Rightarrow \gamma < \gamma_t, \ \cos\varphi_s > 0 \Rightarrow \varphi_s \in (0, \pi/2)$,

above transition $\eta < 0 \Rightarrow \gamma > \gamma_t, \ \cos\varphi_s < 0 \Rightarrow \varphi_s \in (\pi/2, \pi)$.

1.3.3. The RF bucket

The longitudinal motion of a particle can be visualized in the phase space (φ, δ), where closed orbits and open trajectories can be distinguished (Fig. 1.6). The former represent the stable oscillation around the stable phase, well described by Eq. (1.53) for small amplitudes. The latter instead represent the unstable motion characterized by the departure of the particle from the stable phase and the nominal momentum. The separatrix is the boundary between the region of stable motion, called **RF bucket**, and that of unstable one. The bucket area defines the phase and energy acceptance of the accelerator, outside of which RF capture do not occur and the particles will eventually be lost. For this reason the particle distribution of a bunch must entirely fit into the bucket to be properly accelerated with the rest of the beam. The number of buckets around the ring is exactly given by the harmonic number h and represents the maximum amount of particle bunches that a machine can be filled with.

1.4. Beam losses in circular machines

The transverse and longitudinal dynamics discussed so far indicate that, under the action of electromagnetic fields, particles in a beam perform a stable motion around the design orbit. However, in a real accelerator, there is a vast variety of physical processes and imperfections that risk increasing the transverse oscillation amplitude, possibly so that it becomes larger than the dimension of the vacuum chamber, provoking the loss of particles.

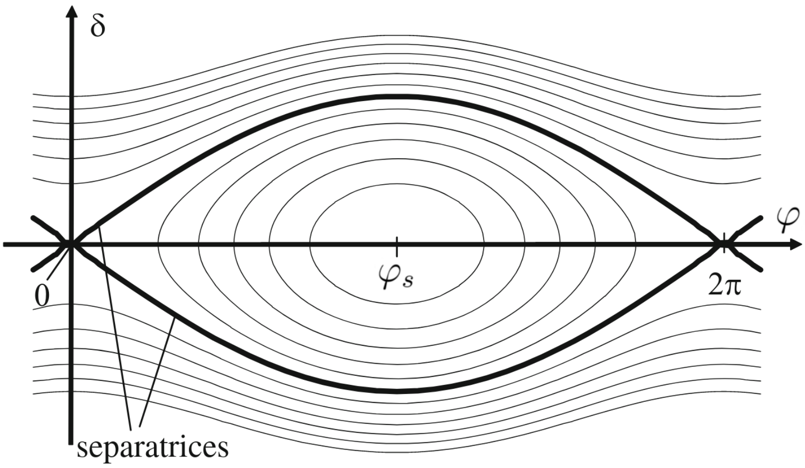

Figure 1.6: Longitudinal motion in phase space (φ, δ) [72].

Particle losses are undesired because of their degrading effect on beam quality and machine performance, as well as their destructive and radio-activating potential on machine components. The mechanisms leading to transverse amplitude growth must be studied and understood in order to control and mitigate them. Since these phenomena cannot be completely avoided, collimation systems capable of disposing of the arising losses in a safe way are typically included in the design of modern high-power accelerators. A collimation system is designed to withstand the maximum expected rates of beam loss. Neglecting very fast loss scenarios due to accidents and faults, several kinds diffusive losses discussed in the next sub-sections can in combination modelled by considering the beam lifetime. This approach consists in modeling the beam intensity as an exponential decay function, whose time constant τ_b defines the beam lifetime:

$$I(t) = I_0 e^{-\frac{t}{\tau_b}} \ , \tag{1.55}$$

where I_0 is the initial intensity.
Then the problem is reduced to assess which is the minimum beam lifetime that can be handled by the collimation system during the phases at maximum energy, as well as assessing the possible impact distribution on the collimation system.

1.4.1. Tune and optical resonances

In circular accelerators such as synchrotrons or storage rings the beam passes the same lattice every turn. For this reason it experiences the same forces that keep it on the orbit once every revolution. Under particular conditions the magnetic structure can cause the circulating beam to resonate, thereby enhancing the transverse oscillations of its particles. As a result the beam size rapidly blows up and gives rise to losses. This phenomenon is called **optical resonance** and it is strictly related to the betatron tune $Q_{x,y}$. The betatron tune has been defined as the number of betatron oscillations performed by a particle in the horizontal or vertical transverse plane during one revolution (1.22). Since there are always discrepancies between theoretical and realistic magnetic fields, for certain values of $Q_{x,y}$ the perturbative effect of the unavoidable field errors on particle motion resonantly sum up turn after turn. In the discussion of betatron oscillation, the magnetic field components in x and y have been expanded up to the first order (Subsec. 1.2.1). However, higher-order components (sextupole octupole, etc.) may be present as unwanted field errors, or may be introduced on purpose for compensation or field correction. It can be demonstrated that for the following values of $Q_{x,y}$ the oscillation amplitudes diverge:

dipole field errors $Q_{x,y} = N$,

quadrupole field errors $Q_{x,y} = N, N/2$,

sextupole field errors $Q_{x,y} = N, N/3$,

octupole field errors $Q_{x,y} = N, N/4$,

where N is an integer.
In general, the optics of a machine must be chosen such that it does not satisfy the condition

$$nQ_x + mQ_y = N \ , \tag{1.56}$$

where n, m and N are integers and the smallest values typically give a stronger effect.
The forbidden tunes can be summarized in a tune diagram where the resonance lines are plotted. An example of a tune diagram for up to 4-th order resonances is shown in Fig. 1.7.
As discussed in previous sections, the particles in a beam have a distribution of momenta around the design momentum p_0. As the effects of magnets on charged particles depend on their energy, each particle experiences field errors related to its own momentum offset $\frac{\Delta p}{p_0}$. As a result, particles with different momenta will all have different tunes. The spread in tune of a beam is expressed through the parameter **chromaticity** Q':

$$\Delta Q = Q' \frac{\Delta p}{p_0} \ , \tag{1.57}$$

with

$$Q' = -\frac{1}{4\pi} \oint k(s)\beta(s)ds \ , \tag{1.58}$$

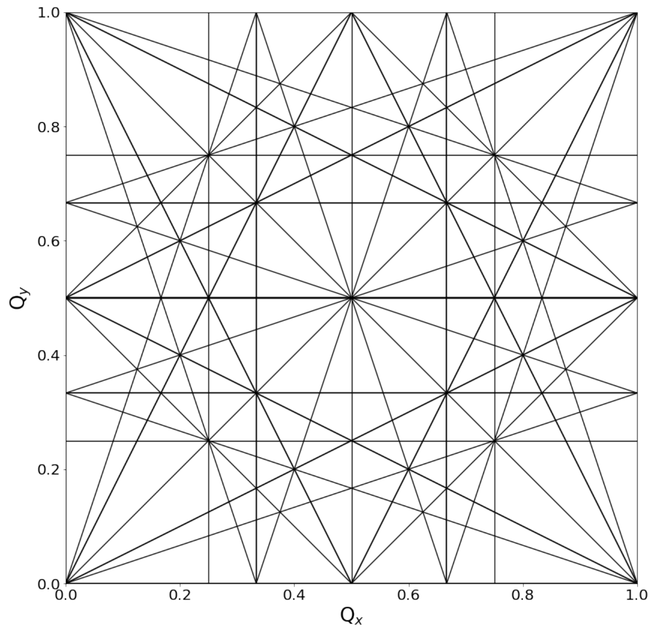

Figure 1.7: Tune diagram example. The machine horizontal and vertical tunes must be far from the lines.

where $k(s) = \frac{q}{p_0+\Delta p}\left(\frac{dB_y}{dx}\right)_{x=0,\ y=0}$ is the focusing function for an off-momentum particle. Thus the working point of an accelerator on the tune diagram is never a single point but a spot with a size determined by ΔQ.

1.4.2. Collective effects

So far it has been neglected that charged particles in a beam are sources of electromagnetic fields themselves. They influence each other and interact with the environment developing the so-called **collective effects**. Among the several consequences of collective effects there are beam instabilities, emittance blow-up and beam loss. The main collective effects are listed below grouped into three categories.

Beam-self This category includes all the interactions among the particles belonging to the same bunch. They can interact through long range coulomb collisions at small angles (intra-beam scattering), or through beam space-charge. Space-charge effect exerts on a particle a net repulsive force which translates into a defocusing effect for the beam. The overall effect is a tune spread proportional to $1/\beta^2\gamma^3$.

Beam-beam In circular colliders, a major part of the losses comes from the interactions between the two colliding beams. Head-on collisions can cause high scattering angles and large deviations from the nominal momentum. In addition, the two counter propagating beams interact with long-range interactions close to the collision point. This eventually causes a tune spread.

Beam-environment Even though the beam circulates in a vacuum chamber there is still possibility for it to interact with residual gas atoms or molecules through elastic or inelastic scattering. Another remarkable collective effect is due to the electromagnetic wake field generated by the accelerated beam. Any discontinuity in the structure crossed by the beam is a source of wake fields. This field, whose frequency spectrum is called impedance, decays over time and can affect the trailing particles or the source itself in a subsequent turn. A witness particle feels a kick proportional to the amplitude of the field left by the source ahead. Impedance leads to a coherent tune shift which scales with the intensity of the beam and can also cause unstable motion.

The change in tune induced by these effects is dangerous, since it may move the tune from a safe value towards a resonance and provoke emittance blow-up and losses.

1.4.3. Collimation systems

All the effects mentioned above are responsible for populating the beam halo. Particles are referred to as halo particles if their transverse amplitudes or momentum deviations are significantly larger than those of the reference particle. Hence it is possible to distinguish between betatron and off-momentum halos. There is no absolute distinction between halo and core particles. For Gaussian distributed beams, it is common to define as betatron halo particles those lying outside $3\sigma_{u,u'}$. Instead, off-momentum halo is composed of the particles lying outside the RF bucket. It is role of the collimation system to perform the cleaning of betatron and off-momentum beam halos. Collimation is performed by placing blocks of engineered material, the collimator jaws, close to the circulating beam. The jaws can safely intercept the halo particles before they get lost in sensitive equipment, providing passive machine protection. Other roles of collimation systems are to protect the experiments against unwanted backgrounds caused by the halo particles, and to protect the machine elements against excessive radiation dose.

The collimator jaw opening sets a constraint for the betatron amplitude of halo particles, as represented in Fig. 1.8. Off-momentum tails of the beam can be cleaned with the same principle but in locations of high dispersion. The bottleneck of machine geometrical

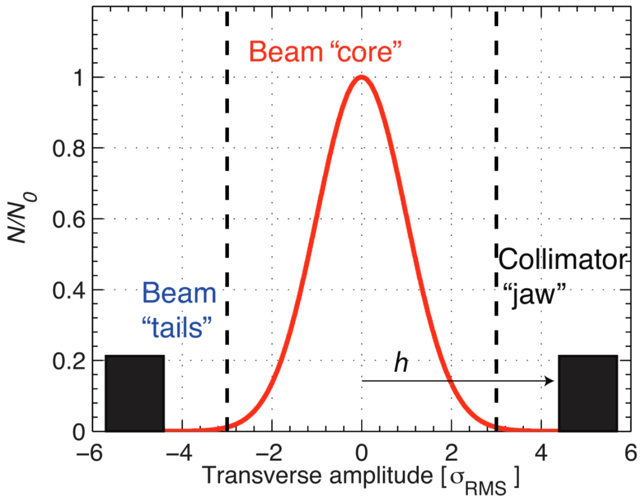

Figure 1.8: Scheme of a two-sided collimator centred around the beam. The half gap h indicates the opening of the jaws in unit of σ_{RMS} [58].

aperture poses an upper limit to collimator settings, which nonetheless must not be too tight to not perturb beam stability. The performance of a collimation system is measured by the **cleaning inefficiency** η_c. This figure of merit expresses the ratio between the number of halo particles lost in other accelerator components, A_{lost}, and those caught by the collimators A_{coll}:

$$\eta_c = \frac{A_{lost}}{A_{coll}} . \tag{1.59}$$

Since some instrumentation has specific requirements on the maximum losses it can tolerate, such as superconductive magnets, it is useful to define the **local cleaning inefficiency** $\tilde{\eta}_c$. This quantity represents the fractional loss per unit length in a range of interest $(s, s + \Delta s)$. It is defined as

$$\tilde{\eta}_c(s) = \frac{A_{lost}(s|s + \Delta s)}{A_{coll}} \frac{1}{\Delta s} . \tag{1.60}$$

In order to ensure the lowest possible cleaning inefficiency, a sequence of collimators can be used to perform multistage collimation. Particles entering the collimator jaws undergo multiple scattering inside the material and may escape without being absorbed. These particles have even larger betatron amplitudes and energy deviation and thus populate the so-called secondary beam halo. The secondary beam halo, together with hadronic and electromagnetic showers generated in the interactions inside the jaws, proceed downstream of the collimator and would in many cases, in particular for the LHC, provoke significant losses if there were no further collimators. For this reason, multistage collimation relies on a hierarchy of primary, secondary, tertiary collimators and active absorbers to guarantee efficient cleaning without any unwanted leak. An efficient cleaning brings several other benefits to the operation of an accelerator, such as concentration of radiation doses or reduction of experimental background.

As the collimation system has many roles, it is important to study which is the primary driving requirement for a specific accelerator when designing its collimation system. An example of a collimation system is presented in the next chapter while discussing the design of the LHC.

2 | CERN LHC ion operation

The European Organization for Nuclear Research (CERN) is an international laboratory of particle physics located at the border between France and Switzerland, near Geneva. Founded in 1954 by 12 countries, it today counts 23 member states. CERN's mission is to provide an unparalleled accelerator facility where people from all over the world can collaborate to extend human knowledge in fundamental physics. Since 2008 CERN operates the Large Hadron Collider (LHC) [26], the largest and highest-energy particle accelerator ever built. A short overview of LHC technology, layout and performance is presented in this chapter. Afterwards, a presentation of LHC ion program motivations, past run achievements and challenges follows.

2.1. The Large Hadron Collider

The CERN LHC is a circular collider designed to produce collisions between proton or nuclear beams at energy regimes never explored before [26]. It can accelerate two beams up to 7 Z TeV per particle, so as to obtain a center-of-mass energy of 14 TeV for proton head-on collisions. The study of the rare processes induced at LHC experiments allows to shed light on the fundamental questions raised by the incompleteness of the Standard Model. The discovery of Higgs boson in 2012 [31] is an example of what this machine is capable of.

The LHC was built inside the already existing 27 km long tunnel of Large Electron-Positron collider[1] (LEP). With the radius of the design orbit fixed by the tunnel circumference, the only way to reach the target momentum of 7 TeV/c was by producing a dipolar magnetic field of 8.3 T. Such a strong magnetic field requires very large current densities, and the LHC hence relies on superconducting magnets. The LHC superconducting coils are made of Niobium-Titanium (NbTi) alloy and are kept at a temperature of 1.9 K by a complex superfluid Helium cooling system. The small transverse size of the tunnel imposes another constraint: its tight diameter of 3.8 m must accommodate not

[1] The LEP, commissioned in 1989 and decommissioned in 2000 to make room to LHC, enabled to measure the mass of W and Z bosons.

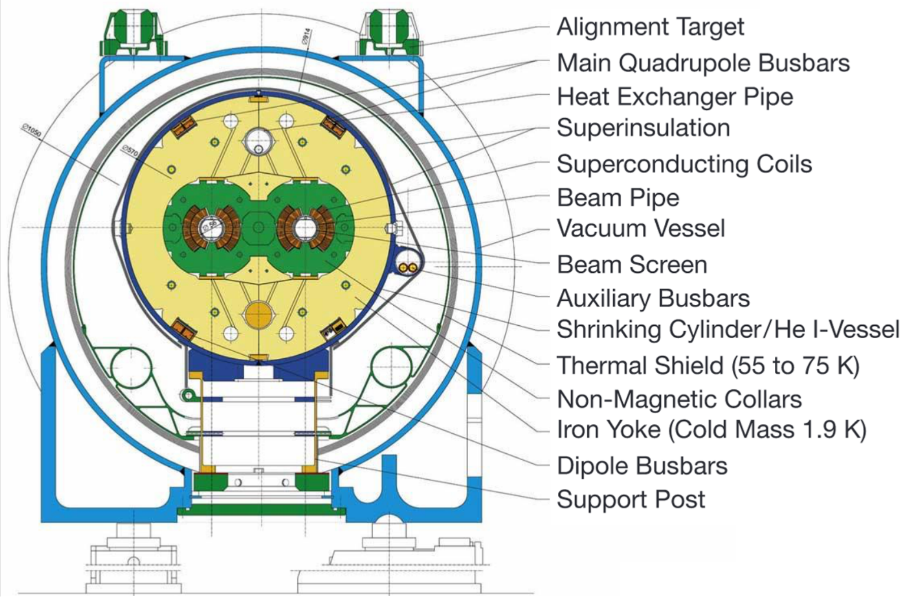

Figure 2.1: A cross section of the two-in-one LHC bending magnet [34].

one but two rings. An elegant two-in-one magnet design, consisting of two separated vacuum chambers inside a common yoke and cryostat, solved this problem. A cross-section showing the superconducting coils of bending magnets is shown as example in Fig. 2.1.

The LHC circumference is divided into eight identical arcs connected by eight long straight sections (LSS). The insertion regions (IRs), where the experiments and the machine utilities are installed, are placed in different LSS, labeled from 1 to 8. The two accelerated beams are made to collide at IPs at four of the IRs. The largest experiments ATLAS (an acronym for A Toroidal LHC ApparatuS) [11] and CMS (the Compact Muon Solenoid detector) [30], respectively IP1 and IP5, have been designed as general-purpose detectors. ALICE (A Large Ion Collider Experiment) [8], located in IR2, is aimed to study collisions between heavy nuclei but also collects data from proton-proton runs. The fourth experiment (IP8) is LHCb [3], where "b" refers to beauty quarks, designed to investigate matter-antimatter asymmetry. Around each of these experiments, special magnets bring the beams into a single vacuum chamber so that they can cross each other. Moreover, special triplets of quadrupole magnets focus the beams to a small spot (down to about $\sim$10 μm radius, depending on configuration) at the collision points to achieve the highest luminosity. The other four IRs are dedicated to other essential equipment, specifically: IR3 and IR7 host the two collimation systems to perform momentum and betatron cleaning respectively, IR4 is assigned to the RF acceleration system and IR6 to the beam-dump system [34]. Fig. 2.2 shows a schematic layout of the LHC.

Beam 1 (B1) and Beam 2 (B2) are injected from the Super Proton Synchrotron (SPS) in

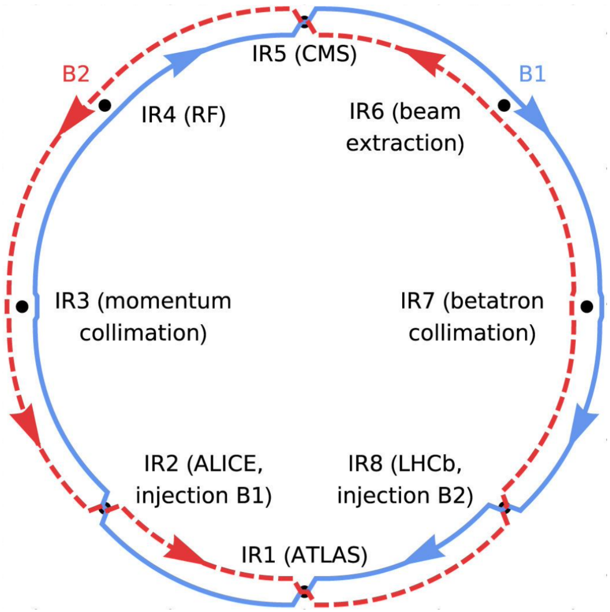

Figure 2.2: Schematic layout of the LHC. The eight IRs are marked along the ring.

IR2 and IR8 respectively, with an initial momentum of 450 Z GeV/c. A complex of smaller accelerators, called the injector chain, is responsible for accelerating and shaping the beam from the source to the LHC. The linear accelerator Linac4 is the first injector for proton beams. It accelerates H^- ions to 160 MeV/c and injects them into the Proton Synchrotron Booster (PSB). A charge exchange injection turns the H^- ions into protons as they enter the PSB. The PSB accelerates the proton beam up to 2 GeV/c momentum before it is extracted and injected into the Proton Synchrotron (PS). Here the beam gets its nominal bunch parameters for the LHC through RF manipulations and is accelerated to 26 GeV/c. Finally, the protons are transferred to the SPS where they get accelerated to 450 GeV/c, ready to be injected into the LHC through the two different B1 and B2 transfer lines.

The injector chain is slightly different for heavy ions. Lead ions are produced by an electron-cyclotron resonance (ECR) ion source. A spectrometer selects the $^{208}Pb^{+29}$ ions, which are accelerated by Linac3 before a stripping foil increases their charge state to +54. $^{208}Pb^{+54}$ ions are then injected into the Low Energy Ion Ring (LEIR) with an energy of 4.2 MeV/nucleon. The ions are accelerated by LEIR up to 72 MeV/nucleon energy, extracted and injected into the PS, where they reach 5.9 GeV/nucleon. A last stripping foil in the beamline between the PS and the SPS removes the remaining electrons from the ions. As last step, the SPS accelerates the fully stripped ions $^{208}Pb^{+82}$ up to 450 Z GeV momentum, ready to enter the LHC.

2.1.1. Measurement of LHC beam loss distributions

By design the LHC nominal proton beam stores an energy of 362 MJ. Even a loss of a small fraction of the beam can provoke physical damage to machine components or quench a superconducting magnet. For this reason, control of the unavoidable beam losses is crucial. In order to detect the beam particles lost, a system of about 4000 beam-loss monitors (BLMs) is installed around the ring. The BLMs are nitrogen-filled ionization chambers, 50 cm long. They are mounted outside of the magnet cryostat at most machine equipment, such as quadrupoles, dipoles or collimators. The BLMs working principle is based on the detection of secondary shower particles on the outside of the machine elements. When the measured losses exceed a certain threshold a beam dump is triggered to prevent quenches and protect the machine. The signals from all the BLMs are continuously logged during LHC operation. This allows to have a global view of the distribution of instantaneous losses occurring all around the ring at any time, so-called lossmaps. We distinguish between lossmaps measured during physics operation and qualification lossmaps for the collimation system. The latter are measured blowing-up a safe low-intensity beam on purpose to study the performance of the collimation system. The provoked betatron or off-momentum losses completely dominate over the collisional losses at the experiments [20]. A technical report on BLM system and its performance can be found in [26, 33, 38].

2.1.2. The LHC collimation system

The LHC collimation system has the fundamental role of intercepting halo particles that would otherwise be lost elsewhere causing possible damage, quenches or beam dumps. The guiding design criterion is sufficient halo cleaning to not overcome quench limit and to provide sufficient passive protection so that key equipment is not damaged during failures. In the worst case scenario of minimum beam lifetime of 0.2 h [10], considered for the LHC design, and design beam stored energy of 362 MJ, the local cleaning inefficiency required in a cold magnet is [58]

$$\tilde{\eta}_c \leq 10^{-5}\ m^{-1}\ . \tag{2.1}$$

A three-stage collimation system is installed in both IR3 and IR7 to perform an efficient cleaning of off-momentum and betatron halos respectively. Here the primary collimators (TCPs) are followed by secondary collimators (TCSs) and by active absorbers (TCLAs). The TCPs and the TCSs can intercept large beam losses and hence are made of a carbon fibre composite (CFC) to be as robust as possible. The TCLAs are instead made of a

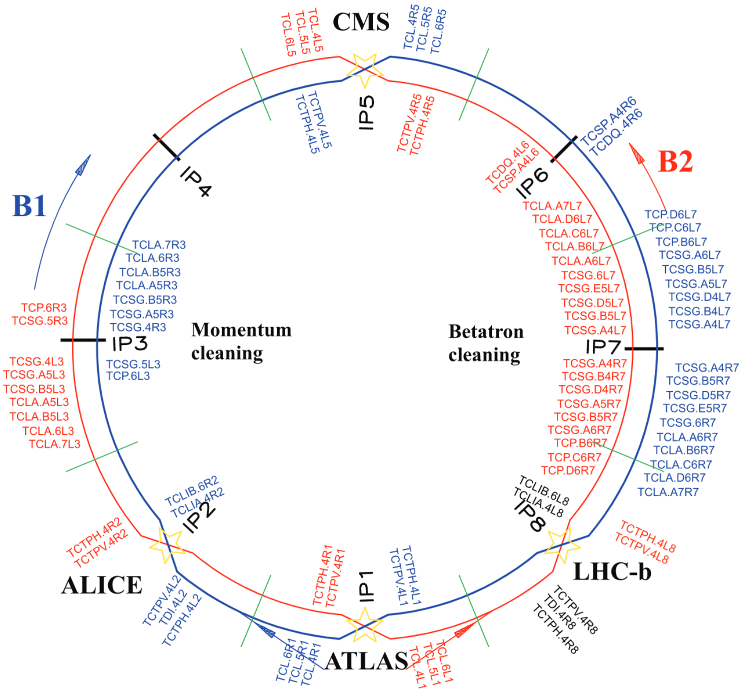

Figure 2.3: Schematic layout of the LHC showing the collimator locations around the ring [58].

tungsten alloy since they must stop all the energy incoming by the upstream collimators. Other collimators are installed in most other IRs. Around each experiments a pair of tertiary collimators (TCTPs) in tungsten alloy can be found about 150 m upstream of the collision points. They are meant to protect the quadrupole triplets in the final focusing system, which typically is the limiting machine aperture during physics operation and hence are very important for the LHC performance reach [22]. These collimators are also important for controlling the machine-induced backgrounds at the experiments [19, 23]. Three TCLs (target collimator, long) are placed downstream of ATLAS and CMS to catch the collision debris. Finally, there are collimators (TDIs) for injection protection in IR2 and IR8, as well as in IR6 (TCDQs) for extraction protection, as precaution in case of miskicked beams [58]. The total system, consisting of 110 movable collimators, is shown in Fig. 2.3.

2.2. The LHC ion program

The LHC timeline is divided into periods of physics operation, called "Runs", alternated by periods of major maintenance referred to as "Long Shutdowns" (LS). Run 1 [7] took place from 2010 to 2013. Run 2 [21] started in 2015 after LS1 (2014–2015) [35] and ended in 2018. At the time of writing, LS2 is over and Run 3 has started in 2022.

At the end of each operational year, for a month, LHC is typically operated with heavy-ion beams. Heavy-ion operation was planned in the LHC Design report [4], in addition to the main program of proton-proton collisions. At an early stage, the main goal of the program was to provide the ALICE detector with Pb-Pb collisions and collect 1 nb^{-1} of integrated luminosity in the first 10 years of heavy-ion operation [8]. However, all the experiments but LHCb joined the program and took data from the very beginning, already during Run 1 [41]. Finally, LHCb also joined the program in Run 2 [40, 43, 47]. Four Pb-Pb physics runs have been executed in 2010, 2011, 2015 and 2018. An integrated luminosity of 1.5 nb^{-1} was collected at ALICE, overcoming the initial target of 1 nb^{-1}, and a total of 2.5 nb^{-1} at ATLAS and CMS. LHCb integrated instead 0.25 nb^{-1} during Run 2.

Besides Pb-Pb collisions, a further mode of operation with proton-nucleus collisions was studied and put in place [42, 45, 48, 70]. After a one-day pilot run in 2012, two full one-month p-Pb runs took place in 2013 and 2016. A total integrated luminosity of 250 nb^{-1} was collected at ATLAS and CMS, and 75 nb^{-1} were collected at ALICE. The heavy-ion program is foreseen to continue with Pb-Pb and p-Pb operation in Run 3 and 4, and the next Pb-Pb run is scheduled for October 2023.

A brief overview of the 2018 Pb-Pb run and 2016 p-Pb run, taken as references to benchmark the simulation tools, is given below. For reference, the parameters achieved in all previous Pb-Pb runs are summarized in Table 2.1, while Table 2.2 shows the parameters during p-Pb operation.

2.2.1. The 2018 Pb-Pb run

During Run 2, the performance limits expected at the time of the Design report were overcome. The beam energy was increased from the value of 3.5 Z TeV of Run 1 to 6.37 Z TeV. The betatron function β at the IPs, called β^*, the number and the intensity of the bunches improved over time. In particular, the bunch structure was changed some time into the run, decreasing the spacing between bunches from 100 ns to 75 ns, which allowed fitting more bunches in the ring.

In 2018 Pb-Pb run, these improvements allowed to reach the highest peak luminosity at ATLAS and CMS for Pb-Pb operation, 6.1 times larger then the design value [39]. Despite that the smallest ever β^* was achieved in both ALICE and LHCb, 0.5 and 1.5 m respectively, their luminosity was levelled at 1×10^{27} $cm^{-2}s^{-1}$ to prevent beam dumps or quenches due to losses from bound-free pair production (BFPP). The main beam parameters for 2018 Pb-Pb run are reported in Table 2.1.

2.2.2. The 2016 p-Pb run

Following the different requirements from LHC experiments, the 2016 p-Pb run was carried out at the beam energies of 4 Z TeV (1 week) and 6.5 Z TeV (2 weeks) [45]. The lessons learnt in the 2013 run and the increased heavy-ion injector performance contributed to the success of the 2016 p-Pb run. During the high-energy phase, a peak luminosity of 8.9×10^{29} cm^{-2}s^{-1}, almost 6 times larger then the design value, was reached at ATLAS and CMS. An integrated luminosity of 190 nb^{-1} was collected in total in ATLAS and CMS and 43 nb^{-1} in ALICE. The main beam parameters for 2016 p-Pb run are reported in Table 2.2.

2.2.3. Towards the heavy-ion runs of HL-LHC

The future heavy-ion runs will profit of the upgrades of the LHC injectors [32] and those foreseen by the high-luminosity LHC (HL-LHC) project [9]. The HL-LHC project aims to achieve much larger integrated luminosities in the future through a series of upgrades to LHC equipment. The upgrades brought in during LS2 make the full heavy-ion "HL-LHC" performance available already in Run 3. The major upgrade in the LHC for future heavy-ion operation was the installation of dispersion suppressor collimators (TCLDs) in IR2. The TCLDs in IR2 are designed to safely intercept the BFPP particles produced in IP2. These collimators, together with an upgrade of the ALICE detector, will allow its luminosity to be levelled at 6.4×10^{27} cm^{-2}s^{-1} during Pb-Pb operation, similarly to ATLAS and CMS. For ALICE, this will increase the 2018 luminosity by more than a factor 6, since it had to be levelled at the LHC design luminosity in order to avoid quenches from BFPP losses.

Table 2.1 shows that for IP1 and IP5, the target peak luminosities for heavy-ion operation of the LHC were largely exceeded, almost reaching the target values of the HL-LHC. Moreover, the goals of integrated luminosities at these IPs for the first phase of operation were achieved in less time than expected. It remains to carry out the operations for longer times, with the improved performance, in order to collect the desired integrated luminosity for the HL-LHC era. The beam parameters envisaged for Pb-Pb and p-Pb operation in HL-LHC are reported in Table 2.1 and Table 2.2, respectively.

	Design	**2010**	**2011**	**2015**	**2018**	**HL-LHC**
Beam energy (Z TeV)	7	3.5	3.5	6.37	6.37	7
Total no. of bunches	592	137	338	518	733	1240
Bunch spacing (ns)	100	500	200	100	75	50
Bunch intensity (10^7 Pb ions)	7	12	11.4	20	21	18
Normalized emittance (μm)	1.5	2	2	2.1	2.3	1.65
β^* at IP1/5 (m)	0.55	3.5	1.0	0.8	0.5	0.5
β^* at IP2 (m)	0.5	3.5	1.0	0.8	0.5	0.5
β^* at IP8 (m)	10.0	3.5	3.0	3.0	1.5	1.5
half crossing, IP1 (μrad)	160	0	-120	-145	160	170
half crossing, IP2 (μrad)	110	40	±80	±137	±137	170
half crossing, IP5 (μrad)	160	0	120	145	160	170
half crossing, IP8 (μrad)	–	-100	-250	-250	160	-170
Peak luminosity, IP1/2/5 (10^{27} cm^{-2}s^{-1})	1.0	0.03	0.5	3.6	6.1	–
Levelled luminosity, IP1/5 (10^{27} cm^{-2}s^{-1})	–	–	–	–	–	6.4
Levelled luminosity, IP2 (10^{27} cm^{-2}s^{-1})	–	–	–	1.0	1.0	6.4
Levelled luminosity, IP8 (10^{27} cm^{-2}s^{-1})	–	–	–	–	1.0	1.0

Table 2.1: Pb beam parameters at the start of Pb-Pb collisions in the LHC, as foreseen in the LHC design report [26], as achieved in 2010 [7, 41], 2011 [7, 54], 2015 [43, 71], 2018 [46, 71] and as envisaged for HL-LHC [24].

	2013	**2016**	**2016**	**HL-LHC**
Beam energy (Z TeV)	4.0	4.0	6.5	7
Total no. of bunches	358	540	540	1240
Bunch spacing (ns)	200	100	100	50
Bunch intensity (10^7 Pb ions)	12	21	21	18
Normalized emittance (μm)	2	1.5	1.5	2.5
β^* at IP1/5 (m)	0.8	11.0	0.6	0.5
β^* at IP2 (m)	0.8	2.0	2.0	0.5
β^* at IP8 (m)	2.0	10.0	1.5	1.5
half crossing, IP1 (μrad)	-145	-140	-140	170
half crossing, IP2 (μrad)	$\pm$62	185	$\pm$138	170
half crossing, IP5 (μrad)	145	140	140	170
half crossing, IP8 (μrad)	-220	-180	-180	-170
Peak luminosity, IP1/2/5 (10^{29} cm^{-2}s^{-1})	1.16	0.1	8.9	22.3
Levelled luminosity, IP1/5 (10^{29} cm^{-2}s^{-1})	–	–	–	–
Levelled luminosity, IP2 (10^{29} cm^{-2}s^{-1})	–	0.1	–	5.0
Levelled luminosity, IP8 (10^{29} cm^{-2}s^{-1})	–	–	–	–

Table 2.2: Pb beam parameters at the start of p-Pb collisions in the LHC, as achieved in 2013 [7, 42], 2016 [45, 71] and as envisaged for HL-LHC [24]. No design parameters are reported since p-Pb runs were not foreseen in the LHC design report. The parameters for 2016 run are reported for both the energies of 4 Z TeV and 6.5 Z TeV.

2.3. Heavy ion physics

The collisions between $^{208}\mathrm{Pb}^{+82}$ beams can reach centre-of-mass energies up to 1.15 PeV. This opens up a new energy regime in experimental nuclear physics, allowing to extend the hadronic matter study. One of the main purpose of LHC ion program is to recreate and study the so-called quark-gluon plasma, a state of matter existed few millionths of a second after the Big Bang [8].

During Pb-Pb operation, the ultraperipheral electromagnetic interactions for colliding nuclei with an impact parameter[2] $b > 2R$, where R is the nuclear radius, dominate over the nuclear inelastic interactions ($b < 2R$) and represent one of the most challenging phenomena. These interactions are responsible of two main effects that introduce luminosity limitations: i) lepton pair production in collisions between quasireal photons and ii) emissions of nucleons in electromagnetic dissociation (EMD) [64].

2.3.1. Bound-free pair production and EMD

In contrast to the more frequent free pair production, in BFPP at least one electron is created in a bound state of one of the ions. Among the possible pair production events, the most dangerous is the single bound-free pair production (BFPP1), involving a single electron:

$$^{208}\mathrm{Pb}^{+82} +^{208}\mathrm{Pb}^{+82} \rightarrow^{208}\mathrm{Pb}^{+82} +^{208}\mathrm{Pb}^{+81} + \mathrm{e}^{+}\ . \tag{2.2}$$

In EMD, a nucleus transits to an excited state after absorbing a virtual photon and then it decays emitting one or more nucleons. Because of the nuclear Coulomb barrier, the most occurring EMD events are those in which a nucleus lose one or two neutrons, namely EMD1 and EMD2:

$$^{208}\mathrm{Pb}^{+82} +^{208}\mathrm{Pb}^{+82} \rightarrow^{208}\mathrm{Pb}^{+82} +^{207}\mathrm{Pb}^{+82} + \mathrm{n}\ , \tag{2.3}$$

$$^{208}\mathrm{Pb}^{+82} +^{208}\mathrm{Pb}^{+82} \rightarrow^{208}\mathrm{Pb}^{+82} +^{206}\mathrm{Pb}^{+82} + 2\mathrm{n}\ . \tag{2.4}$$

The above mentioned processes cause a very small transverse momentum recoil and a well-defined magnetic rigidity change in at least one of the colliding nuclei. The new magnetic rigidity can be written as [18]

$$B\rho(1+\delta)\ , \tag{2.5}$$

[2]The impact parameter b is defined as the perpendicular distance between the path of a projectile and the center of a potential field created by an object that the projectile is approaching.

with δ given by

$$\delta \approx \frac{Z_0(A_0 + \Delta A)}{A_0(Z_0 + \Delta Z)}(1 + \delta_p) - 1 \; , \tag{2.6}$$

where ΔA and ΔZ are the change in mass and atomic number of the original ion with A_0 and Z_0, and δ_p is the fractional momentum deviation per nucleon with respect to an ion circulating on the central orbit of a circular collider.

As a result of these ultraperipheral interactions, a secondary beam with a slightly modified magnetic rigidity (due to the change in charge for BFPP and in mass for EMD1 and EMD2) emerges from both directions of the IP at small angle to the main beam. It follows a dispersive trajectory, eventually hitting the aperture of the machine where the local dispersion D and the horizontal aperture A_x satisfy the condition [18]

$$D\delta \geq A_x \; . \tag{2.7}$$

From the results of a previous study [18], for $^{208}Pb^{+82}$ only BFPP and EMD2 cause a fractional rigidity deviation δ greater than the momentum acceptance of LHC arcs, thus meeting the condition given by Eq. 2.7. Whereas BFPP and EMD2 will cause localized losses, EMD1 will not and $^{207}Pb^{+82}$ ions will be removed by the momentum collimation system IR3.

Apart from contributing significantly to the decay of intensity and luminosity [13], these beam losses cause a localised power deposition given by:

$$P_p = \mathcal{L}\sigma_p E_b \; , \tag{2.8}$$

where $\mathcal{L}$ is the luminosity at the IP, σ_p is the cross section of the process and E_b is the energy carried by the primary beam. The single BFPP is the most significant process in terms of cross section (Table 2.3) and thus the main concern for maximizing the luminosity: early estimations in 2004 found that localised heating due to BFPP losses was high enough to induce a quench of the impacted magnet already below nominal luminosity [49]. This was demonstrated at the 2015 quench test [44, 63], where the impacted dipole downstream of IR5 quenched at a luminosity of 2.3×10^{27} cm^{-2}s^{-1}. In HL-LHC, the BFPP beam carries about 165 W of power for a luminosity of 6.4×10^{27} cm^{-2}s^{-1}. Therefore, if nothing is done, the BFPP losses put an upper limit on the operational luminosity.

For this reason, mitigation strategies have been adopted at every IP but IP8, where luminosity levelling to a safe value of 10^{27} cm^{-2}s^{-1} remained the only option. These measures mainly consist of orbit bumps[3] to deflect the BFPP beams to a safer impact location and carefully dispose of resulting losses [64]. Recently, a higher integrated luminosity of 2.5 nb^{-1} has been requested at LHCb for the future runs [29] and hence a study of a dedicated solution to safely maximize the BFPP losses in IR8 has become a concern.

2.3.2. Mitigation strategies for BFPP

ATLAS and CMS The optics around IP1 and IP5 are similar, thus allowing a common analysis for the two experiments. BFPP beams emerging from either ATLAS or CMS naturally hit the second superconducting dipole of the cell 11 of the dispersion suppressor (DS) [64]. The DS is the transition region connecting the FODO cells in the arcs to both sides of the straight sections hosting the experiments. Each DS is made up of four cells, numbered from 8 to 11, with each one containing one superconducting quadrupole and two superconducting dipoles. Since an empty connection cryostat replaces a dipole at one position in the DS lattice, it is possible to move the losses out of the dipole MB.B11 into the connection cryostat by means of an horizontal orbit bump around the impact location [18].

In Fig. 2.4 a plot from a previous study [64] shows the trajectories of primary and BFPP beams emerging from both sides of IP5, with and without orbit bump applied. The connection cryostat does not contain any magnet that can quench, but it does contain superconducting bus bars, although at a larger distance from the beam and away from the mid-plane. The higher steady-state quench limit of bus bars in connection cryostat (200-300 mW/cm^3) than in dipole magnets (10–20 mW/cm^3), as well as the geometric placement of the superconductors, ensures a greatly reduced risk of quench and therefore a complete alleviation of the luminosity limits for presently achievable luminosities [64]. This alleviation measure has been adopted at both IP1 and IP5 since Run 2 (2015), enabling the achievement of a peak luminosity over 6×10^{27} cm^{-2}s^{-1} [39].

σ_{BFPP1}	278 b
σ_{EMD1}	96 b
σ_{EMD2}	29 b
σ_{nucl}	7.8 b

Table 2.3: Burn-off cross sections for main interactions between colliding Pb-Pb beams at 7 Z TeV [18].

[3] An orbit bump is a deliberate shift of the transverse position of the beam within a limited region, which does not affect the rest of the ring [73].

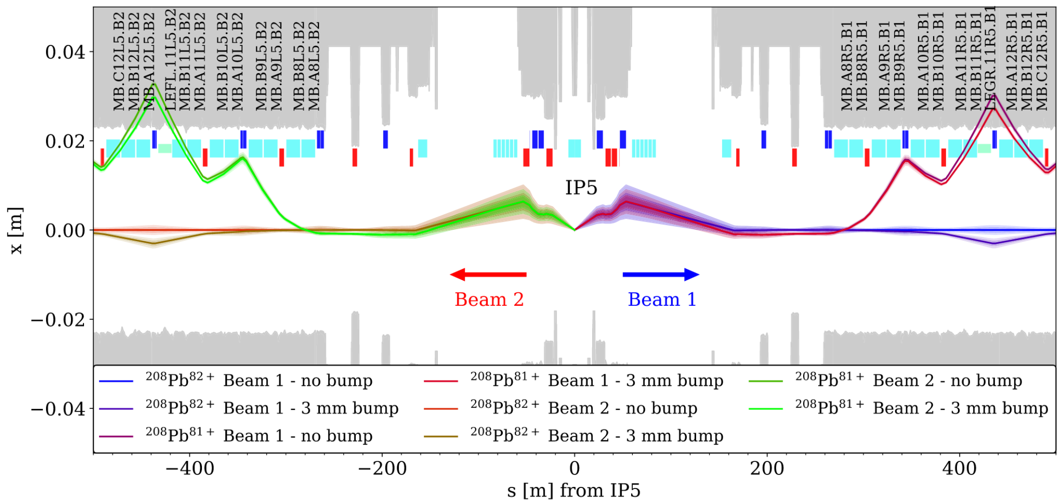

Figure 2.4: Effect of a -3 mm orbit bump around Q11 on primary ($^{208}Pb^{+82}$) and BFPP ($^{208}Pb^{+81}$) beams (1σ envelopes). The incoming beam envelopes, before the collision at IP5, are not shown. The aperture of the machine is represented by the grey shaded area [64].

ALICE Around IP2 the quadrupoles have opposite polarity with respect to those around IP1/5 and this does not permit implementing the same strategy. BFPP beams emerging from ALICE naturally hit the second superconducting dipole of the cell 10, already at the first peak of their trajectory. Since the dispersion function has a minimum at the location of the connection cryostat, there is no possibility to move the losses there. An orbit bump around the quadrupole Q10 could just move some, or all, losses from MB.B10 into the dipole MB.C12 in the cell 12.

During 2015 and 2018 runs the luminosity of ALICE was levelled to 10^{27} cm^{-2}s^{-1} to keep BFPP power deposition below the quench limit. In order to achieve a peak luminosity in Run 3 similar to that of ATLAS and CMS, new TCLD collimators have been installed in the IR2 connection crysotats during LS2. The TCLD can be moved in to an opening small enough to intercept the BFPP losses from IP2 in the connection cryostat. This is made possible when the beam is deflected by a horizontal orbit bump around Q10, as shown in Fig. 2.5.

LHCb No mitigation strategy has been planned and put in place in IR8. The recent request for higher luminosity in LHCb, which in past runs was levelled to a safe value of 10^{27} cm^{-2}s^{-1}, determined the need for a dedicated alleviation to deal with the more intense BFPP losses that follow. The optics around IP8 is similar to that in IR2, hence not allowing to move BFPP losses into the connection cryostat through a horizontal orbit bump, and TCLD collimators would be needed as in IR2. However, such an upgrade is

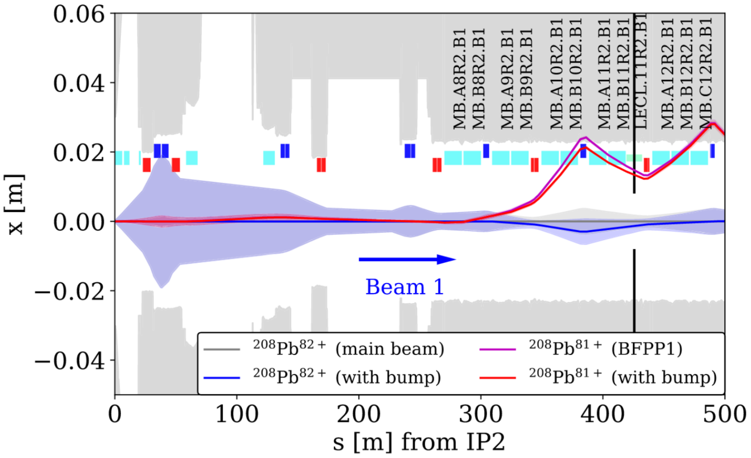

Figure 2.5: Effect of a -3 mm orbit bump around Q10 on primary (12σ) and BFPP (1σ) beams emerging from IP2. The collimator installed at s=430 m completely intercepts the deflected BFPP beam. The aperture of the machine is represented by the grey shaded area [64].

presently not foreseen.

In this regard, a study on BFPP losses in IR8 has been carried out within this thesis work, with the aim of analysing their position and distribution and investigating any possibility of partial alleviation through orbit bumps.

3 | Simulation tools

The study carried out within this thesis relies on the use of MAD-X [1] and the coupling [5, 56, 66] between the two simulation codes SixTrack [2, 20, 59, 65] and FLUKA [15, 36]. This chapter presents the main features of these codes that have been used to obtain the results shown in the next chapters.

3.1. MAD-X

MAD-X (methodical accelerator design) is a tool developed at CERN for the design and study of particle accelerators. It consists of a core program, and modules for specific tasks such as twiss parameter calculation, matching, thin lens tracking and many other [1].

In this code, an accelerator is described as a sequence of beam elements placed sequentially along the beam orbit. A sequence file, given as input, contains the description of the beam line components, such as magnets, collimators, or RF cavities (element type, length, etc). Typically, the magnetic strengths are given in a separate input file (strength files). Once these files are provided as input to MAD-X, it is possible to perform different operations and solve various problems. Firstly, the beam optics can be computed around the ring. MAD-X can use variables, that in turn control the strengths of several different elements with a parametric dependence. Such variables are called knobs, and they can be setup to automatically compute the magnet strengths required to obtain the specified value for a variable. This is typically done for the crossing bumps at the IPs, so that it is enough to specify the value of a crossing angle in order to obtain the required strengths and the resulting orbit for a crossing scheme.

The functionalities of MAD-X mainly used in this work are the TWISS and the MATCH commands. The TWISS command calculates the linear optical functions, and optionally the chromatic functions, around the lattice of a given sequence. This command can be executed either without providing any boundary conditions or giving some starting conditions. In the first case the TWISS command computes the periodic solution and returns as output the periodical optical functions and the closed orbit. In the second case

MAD-X computes the evolution of the given initial values through the lattice. This can be used to, e.g., study the behaviour of a secondary off-momentum beam created at an IP in the collisions, entering a value for the initial fractional momentum offset acquired in the collision.

Matching of beam optics, i.e. computing the magnetic strengths required to achieve specified optics conditions, can be instead performed through the MATCH command. It allows to declare a set of variables which are varied, typically strengths of magnets, in order to match the specified constraints. An example of MATCH command application is the implementation of an orbit bump: MAD-X computes the strengths of the involved kicker magnets to satisfy the conditions locally imposed on the orbit.

3.2. SixTrack

SixTrack is a single particle tracking code optimized for tracking in high energy rings over a large number of turns. It uses a symplectic approach to track the evolution of particle coordinates in the six-dimensional phase space. The tracking is performed element-by-element through a thin-lens model of the magnetic lattice, which can include multipoles up to the 20th order.

SixTrack takes as input a thin-optics sequence, which can be created by MAD-X. Other inputs are the machine aperture model, accounting for the geometrical aperture with a 10 cm longitudinal precision, and the collimator database, where the collimator parameters and settings are given. When a particle hits a collimator, its interaction with the jaw material can be simulated through a built-in Monte Carlo code [27, 67, 68]. This scattering routine includes multiple Coulomb scattering, Rutherford scattering, nuclear elastic and inelastic scattering and single diffractive events. Each particle from an initial distribution is tracked over the specified number of turns, unless it is lost before. A particle is considered lost by SixTrack either when its coordinates exceed the geometrical aperture or if it undergoes inelastic interaction (excluding single diffractive scattering) inside a collimator. Particles which are not absorbed by a collimator are tracked further.

The two main outputs of SixTrack are a detailed recording of the aperture losses and a summary of the interactions with the collimators. For the aperture losses, the coordinates are specified for each lost particle. Instead, the collimator summary file includes information on the number of impacts, the number of particles and energy absorbed by each collimator. These two output files allow to reconstruct simulated lossmaps, plotting the energy lost around the ring as a function of the longitudinal coordinate. For this reason, SixTrack is one of the main tools used for collimation studies at CERN [20].

Among the many other outputs that can be requested, it is worth mentioning the beam population dump. This file consists in a printout of the position in phase-space for all the particles at a specified element of the sequence.

3.3. FLUKA

FLUKA (fluktuierende kaskade) is a multi-purpose particle-physics Monte Carlo simulation code used to simulate the interaction of particles and nuclei with matter and their transport. The FLUKA code is constantly updated with state-of-art models of physical interactions for about 60 different particles, including photons, electrons, neutrinos, hadrons and the corresponding anti-particles.

The initial particles, specified as starting conditions, are tracked together with all the secondaries produced in the induced hadronic and electromagnetic cascades. The user defines the 3D geometry where FLUKA performs the tracking. Detailed material composition and presence of electromagnetic fields can be specified for the geometry, allowing to reproduce even the most complicated scenarios. The FLUKA geometry of LHC (Fig. 3.1) has been built over the past years to serve many purposes. For instance, it has been used for studies of energy deposition in the accelerator elements [16], background to experiments [19], induced radioactivity [37], and radiation to electronics [60].

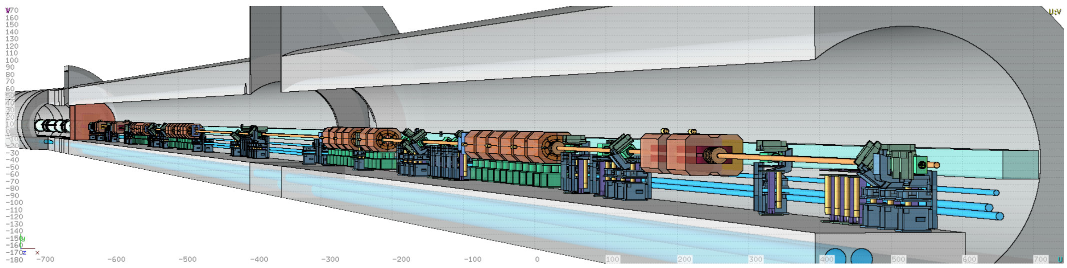

Figure 3.1: LHC IR7 LSS FLUKA geometry visualised with Flair [69].

3.4. SixTrack-FLUKA coupling

The SixTrack-FLUKA coupling combines the two codes to put together the tracking efficiency of SixTrack and the state-of-art account of physics processes of FLUKA. This approach avoids the rough simplifications of the scattering routines embedded in the tracker tools, replacing them with the more sophisticated models incorporated in FLUKA, thus resulting in more accurate predictions. This is especially relevant when dealing with heavy ions and their complex interactions with matter, which are not implemented in the

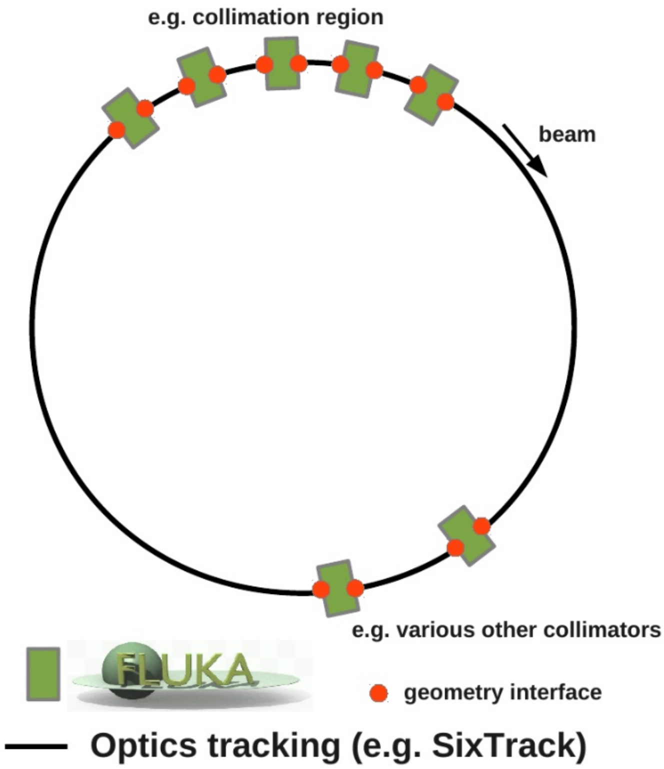

Figure 3.2: Schematics of SixTrack-FLUKA workflow [66].

built-in scattering routine.

The coupling is implemented such that there is a clear boundary between the two codes: the tracking of particles through the accelerator lattice is performed by SixTrack, whereas the beam-matter interaction is simulated by FLUKA (Fig. 3.2). The communication between the codes relies on the FlukaIO library, an independent C++ TCP/IP library which enables the two codes to exchange particle coordinates over a network port.

The lattice elements where particle interactions with the accelerator components have to be simulated are labelled for transport in FLUKA. When the beam particles tracked by SixTrack reach a labelled element, they are transferred to FLUKA which simulates their transport and interactions in the corresponding 3D geometry. Once particles reach the geometry interface, marking the boundaries of the FLUKA insert, they are sent back to SixTrack to be further tracked. This process continues until all the particle are lost either in a FLUKA region or in the rest of the machine.

The 3D geometry of the concerned insertion regions is described in the FLUKA input file, built by a separate program called the Line Builder, and using the so-called FLUKA element database (FEDB) [57]. The FEDB is a dedicated database containing all the

FLUKA models of relevant objects from CERN accelerator complex. These are taken as input by the Line Builder, together with the optics sequence and the collimator database, to assemble the FLUKA geometries. The FLUKA input contains the settings of physics and transport as well. These settings can be customized to keep the CPU time reasonably low, for instance by switching off unnecessary physics processes or adopting higher energy cuts for particle production and transport.

3.4.1. Setup of a collision source

The SixTrack-FLUKA coupling can be used to simulate beam-beam and beam-target collisions and track the products resulting from the interactions. The collisions are simulated in FLUKA and forced only at the first turn in an insertion region of interest, which has to be specified in the FLUKA input.

For beam-beam collisions, every particle reaching the concerned insertion region is made to collide with another particle of the other beam, sampled run-time. The implementation is as general as possible: while the crossing conditions of the tracked beam are defined by the usual tracking, those of the target beam are independent and can be determined via input parameters. The target-beam parameters that can be specified include the optics functions, momentum spread, horizontal and vertical normalized transverse emittance, atomic and mass number of beam particles. This allows to force asymmetric collisions between different ion species. However, target-beam energy cannot be specified since target beam is automatically assumed to have the same magnetic rigidity as the main beam. The types of interaction that can be turned on, in any combination, are nuclear inelastic, nuclear elastic and EMD but not BFPP. The collision positions are sampled around the centre of the FLUKA model of the colliding insertion region, with a longitudinal spread indicated by the user.

Instead, when simulating beam-target collisions, the particles received by FLUKA in the insertion of interest are made to interact with a nucleus of the residual gas, at rest. In this case, it is sufficient to specify the material of the gas and the extent of the region where interactions are forced.

4 | Study of collisional losses for Pb-Pb

In this chapter a study of collisional losses during LHC Pb-Pb operation is carried out. The simulation tools described in the previous chapter have been used to simulate the loss pattern around the ring caused by Pb-Pb collisions at the four experiments. BFPP, EMD and inelastic interactions have been taken into account in the simulation, neglecting the elastic interactions. These have a low cross section compared to the other processes, cause small scattering angles and do not fragment ions, hence not significantly contributing to the losses. The results have been compared to LHC data from past runs and used to estimate these losses in future runs.

Firstly, a study on the localized losses caused by BFPP around IP8 is presented, with the aim of proposing a dedicated alleviation method. An analysis of the simulated distribution of Pb-Pb collision products from EMD and inelastic interactions, as well as their simulated loss locations, follows. Then, the simulation of a Pb-Pb collisional debris lossmap for 2018 is shown and compared to a corresponding measured lossmap. This contains the weighted contributions from losses caused by both EMD, BFPP, and nuclear inelastic interactions. Lastly, a prediction of collisional lossmap for future operation in Run 3-4 is given, including also all these processes.

4.1. BFPP beam losses from LHCb

4.1.1. BFPP losses at IP8

Losses from BFPP are the most important in terms of beam loss power, due to the large cross section (see Table 2.3). Such losses have been studied in detail for IP1, IP2 and IP5 (see Subsec. 2.3.2), hence there is no need to repeat these studies. However, a detailed study of BFPP at IP8, including possible alleviation methods to reach the recent increased LHCb luminosity goal has not been done previously. The study described in this section therefore consists of the tracking of BFPP particles emerging from IP8, the analysis of the loss pattern caused by their impact and the investigation of possible orbit bumps as mitigation strategy. Moreover, the prediction of BFPP particle distribution at the beginning of hit element provides the input for energy deposition studies to possibly optimize the LHCb levelling target.

The dispersive trajectory of BFPP ^{208}Pb^{+81} ions has been mimicked by tracking fully stripped ^{208}Pb^{+82} ions with the δ corresponding to the change in magnetic rigidity due to the acquisition of an electron:

$$\frac{p_{simulation}}{q_{simulation}} = \frac{p_{BFPP}}{q_{BFPP}} \rightarrow p_{simulation} = \frac{q_{simulation}}{q_{BFPP}} p_{BFPP} = \frac{82}{81} p_{BFPP} \tag{4.1}$$

The studies have been carried out for both B1 and B2, considering the LHC optics deployed in 2018 for Run 2 (see Table 2.1) and taking into account different energies and emittances.

As a first check, the trajectory of the BFPP beam has been computed through a MAD-X twiss, using as starting conditions the solution for closed orbit at IP8 and a momentum offset $\delta = \frac{1}{p}(\frac{82}{81}p - p) = \frac{1}{81}$. The trajectories followed from IP8 by the main and BFPP beams, both for B1 and B2, are shown in Fig. 4.1. The BFPP beams hit the second superconducting dipole in cell 10, and at the s-location of the empty connection cryostat their trajectories have a minimum, similarly to what happens in IR2 (see Par. 2.3.2). Therefore, a full alleviation would require a TCLD collimator, which is an upgrade not foreseen at this stage.

Furthermore, the detailed loss patterns have been simulated with SixTrack, tracking the BFPP particles from IP8 and recording the aperture losses. Momentum and angular kicks from BFPP have been supposed small and then neglected as in Ref. [18]. BFPP ions have been represented only accounting for their change of charge (off-momentum beam of ^{208}Pb^{+82} ions) and assuming them to be initially distributed in phase space as the collision points and not simply as the incoming bunches. It can be demonstrated that if the particles of a bunch have a Gaussian distribution, then the distribution of collision points in space is still a Gaussian but narrower by a factor $\sqrt{2}$ in both the transverse and longitudinal directions, while the angular distribution is unchanged [18]. For each simulation case an initial Gaussian distribution of 10000 off-momentum ^{208}Pb^{+82} ions, with a bunch length of 1.1 ns, has been sampled. No spread in momentum has been taken into account in order to have particles all with the same magnetic rigidity and obtain conservative, narrower estimations for the loss patterns. Indeed, a spread in magnetic rigidity would mean a slightly different bending for each BFPP particle and a broader distribution of the losses, which would cause a lower peak power load.

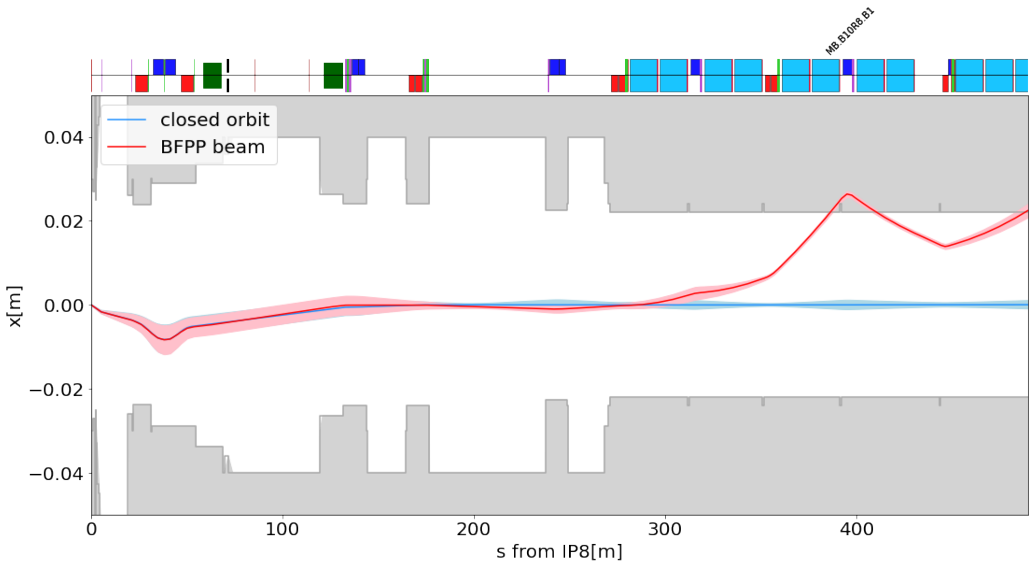

(a) Beam 1.

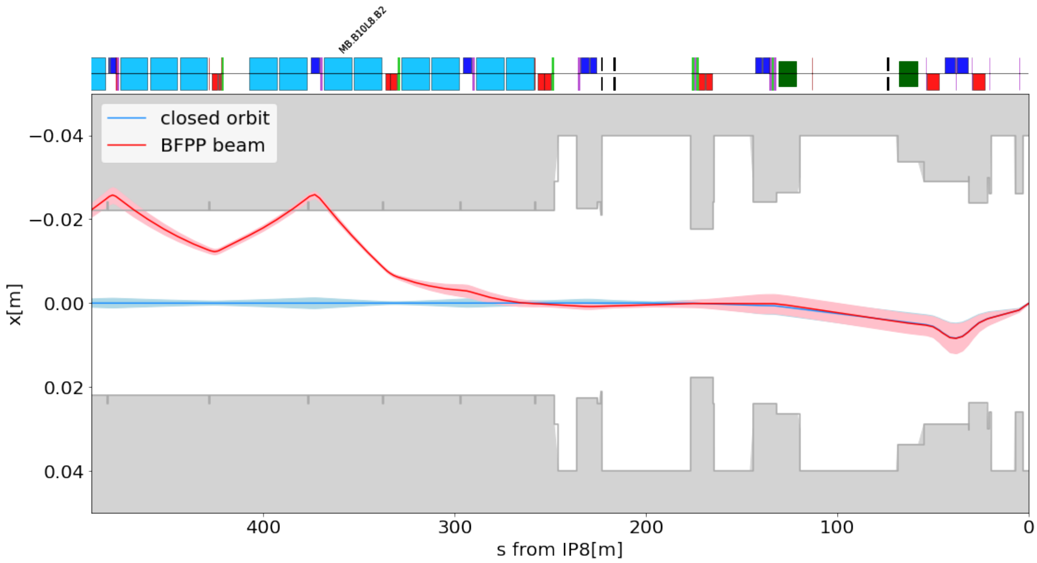

(b) Beam 2.

Figure 4.1: Closed orbit and BFPP dispersive trajectories (3σ envelopes) from IP8 computed with MAD-X in the 2018 LHC configuration for Pb-Pb at 6.37 Z TeV. The aperture of the machine is represented by the grey shaded area. The secondary beams hit the second superconducting dipole in cell 10 (MB.B10R8.B1 and MB.B10L8.B2).

The loss patterns on MB.B10R8.B1 and MB.B10L8.B2 obtained for an energy of 6.37 Z TeV and an emittance of 2.3 μm, i.e. operating conditions for 2018 run, are shown in Fig. 4.2. The distributions of the losses for B1 and B2 are centered at 386.35 m and 365.26 m downstream of IP8, respectively. In view of the possibly updated beam parameters in the next runs [24], simulations with 1.6 μm emittance and 7 Z TeV energy have been carried out as well. The same optics was used, as it is expected to be extremely similar to the optics used in the future. Changing beam emittance and energy has no significant effect on the centre of loss pattern, but rather on its spread since these two parameters affect beam transverse dimensions. The resulting standard deviations of the loss patterns simulated for the different combinations of emittance and energy are summarized in Table 4.1.

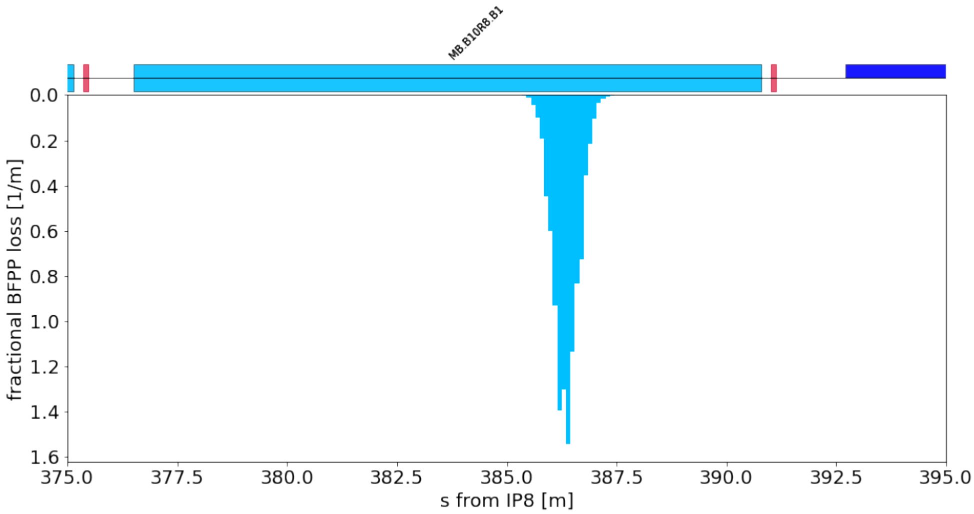

(a) Beam 1, losses at 386.347 ± 0.281 m.

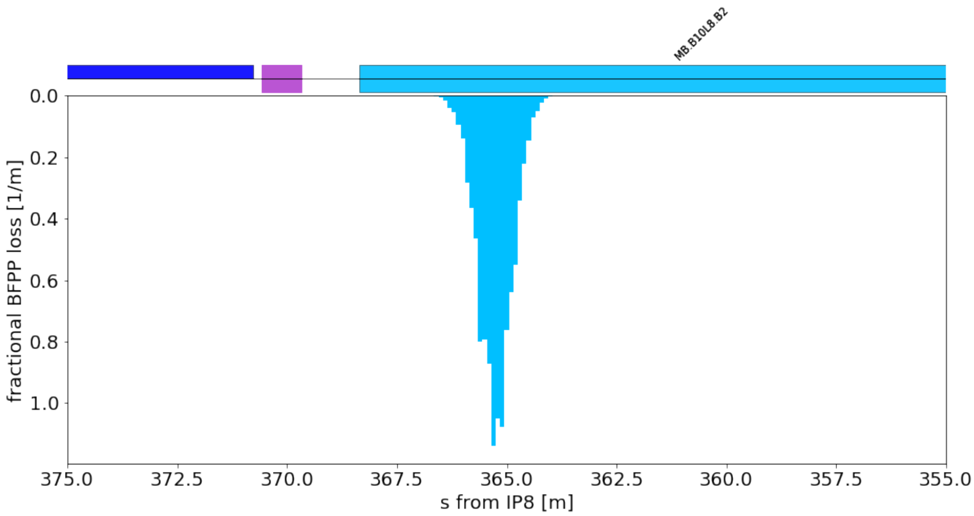

(b) Beam 2, losses at 365.261 ± 0.379 m.

Figure 4.2: BFPP loss patterns on MB.B10R8.B1 and MB.B10L8.B2, simulated for an energy of 6.37 Z TeV and an emittance of 2.3 μm with SixTrack. The coordinate axis has $s = 0$ at IP8.

		B1 ($s = 386.35$ m)	**B2** ($s = 365.26$ m)
6.37 Z TeV	1.6 μm	0.234 m	0.315 m
	2.3 μm	0.281 m	0.379 m
7 Z TeV	1.6 μm	0.223 m	0.302 m
	2.3 μm	0.268 m	0.361 m

Table 4.1: Standard deviations of the longitudinal loss locations of BFPP particles emerging from IP8 for different values of emittance and energy. The optics is assumed the same in the two cases.

From the simulations it can be seen that under the same conditions, BFPP losses for B2 always occur about 20 m more upstream and with a broader distributions than B1. This is caused by small asymmetries in the optics and in particular the dispersion. The most concentrated losses have been obtained for B1, 7 Z TeV energy and 1.6 μm emittance, which is the scenario with the smallest transverse beam dimensions.

4.1.2. Comparison with BLM data

The prediction of loss patterns due to BFPP beams in LHCb has been compared to the BLM signals during Pb-Pb collisions. The fill #7477 from the 2018 Pb-Pb run has been taken as reference, with timestamp $2018-11-26$ $22:45$. It should be noted that we only do a qualitative comparison of the loss locations, since the absolute signal of the BLMs depend on the hadronic and electromagnetic shower development in the local geometry, which is not included in the simulation setup.

A view of the signals in the regions of interest (right and left side of IP8) is shown in Fig. 4.3. In both cases the peaks that can be attributed to BFPP losses are very close to the simulated ones, but located few meters downstream with respect to the centre of predicted loss patterns. For B1 the highest loss signal is $\sim$7 m downstream, at the quadrupole MQML.10R8.B1, whereas for B2 it is $\sim$5 m downstream, at the horizontal kicker magnet MCBCH.10L8.B2.

There are several possible reasons for the small discrepancy. Firstly, it must be emphasised that BLMs' ionization chambers detect the radiation coming out on the outside of the cryostat, resulting from the interaction of BFPP particles with vacuum chamber and surrounding materials, thus they do not directly record the beam losses but a signal which is proportional to it and that is likely shifted downstream of the position where particles are lost. It could also be that a BLM is actually missing at the location where the BFPP beam hits the aperture, since the peak simulated for B1 falls into a region where

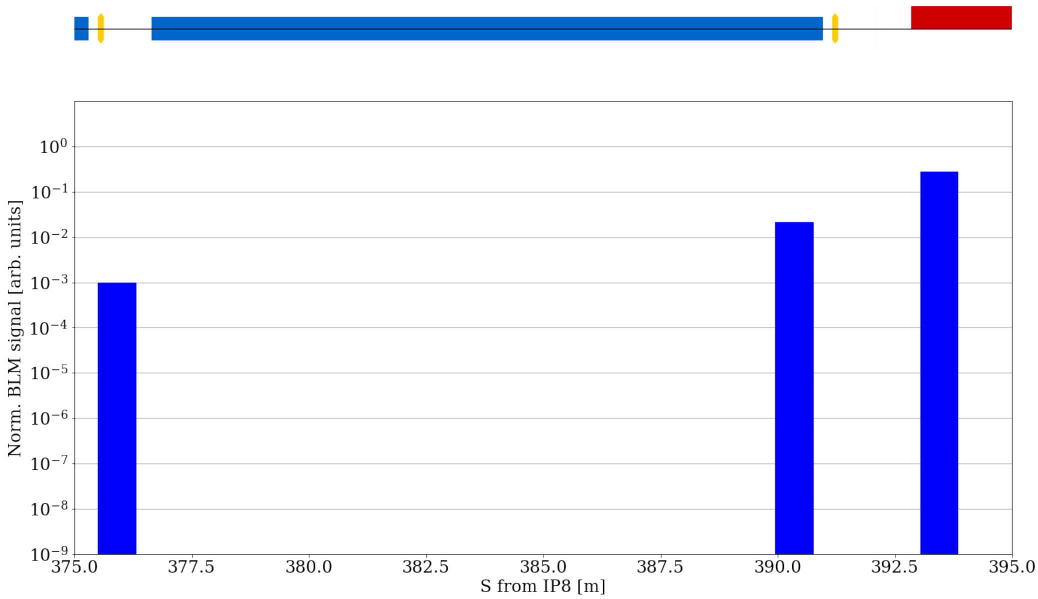

(a) Beam 1, region between 375 m and 395 m at the right side of IP8.

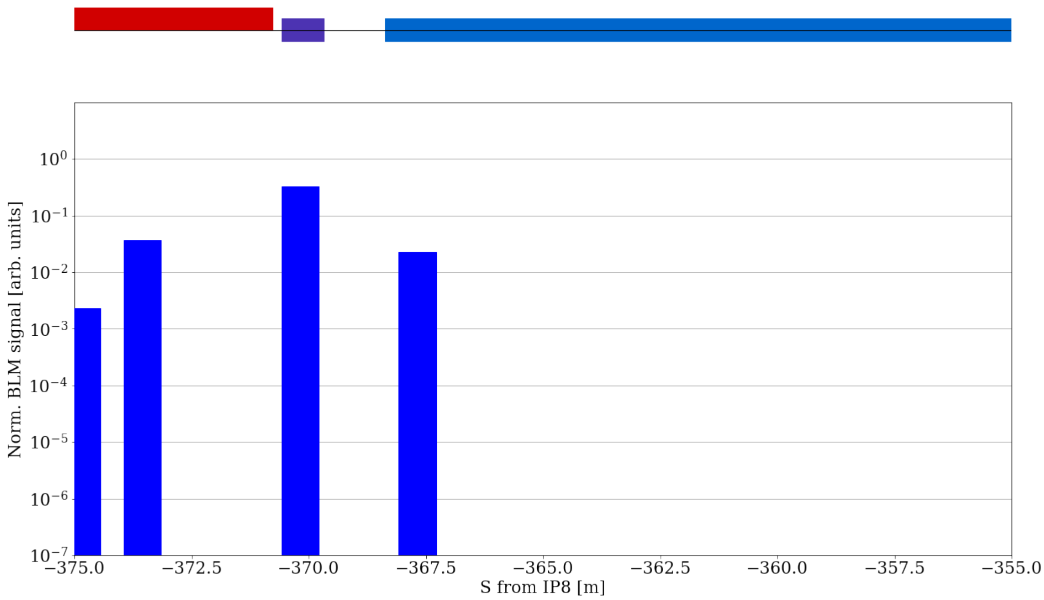

(b) Beam 2, region between 355 m and 375 m at the left side of IP8.

Figure 4.3: BLM signals at right and left side of IP8, where BFPP losses are expected to be found. Signals extracted for fill #7477, at the timestamp $2018-11-26\ 22:45$.

there are no BLMs installed within about 10 m. Another reason to explain such shift forward is that the actual aperture of beam pipe might be slightly misaligned or larger than the aperture accounted in simulation model, which accounts for a small error margin on the perfect design aperture. In this regard, the simulation of BFPP loss patterns for 2018 operating conditions has been carried out again changing the aperture of the model in order to quantify how a larger aperture impacts on the shift of losses. Only the aperture on the side of the losses matters, but for simplicity the full aperture was changed.

The results for an effective aperture increase of 1, 2 and 3 mm are summarized in Table 4.2. Enlarging the aperture of 1 mm shifts the centre of loss pattern a little less than 2 m downstream. Hence we can expect that a combination of the effects above mentioned leads to shift some meters downstream the measured losses with respect to the predictions.

	B1	**B2**
nominal aperture	386.35 m	365.26 m
+1 mm	388.21 m	367.10 m
+2 mm	389.98 m	368.90 m
+3 mm	391.33 m	370.71 m

Table 4.2: Mean positions of BFPP losses from IP8 for larger apertures, computed with SixTrack (6.37 Z TeV energy and 2.3 μm emittance).

4.1.3. BFPP alleviation through orbit bumps in IR8

A full alleviation of the BFPP losses in IR8 through a new TCLD collimator is not possible in the short term. Hence we explore other partial alleviation methods, which are possible to implement but do not show the same potential for increasing the peak luminosity. In particular, we study the shifting of losses using orbit bumps.

The BLM thresholds were decreased at Q10 magnets to reduce the risk of symmetric quenches [51], therefore moving the losses out of cell 10 even to another magnet could ensure a higher BLM signal tolerance. Moreover, moving the losses into a region where the beam has a larger spot size could potentially reduce the peak power load, thanks to a wider impact distribution. For these reasons, an horizontal orbit bump around Q10 has been implemented with MAD-X match for both B1 and B2. The horizontal kickers MCBCH.8R8.B1, MCBCH.10R8.B1 and MCBCH.12R8.B1 have been employed for B1, whereas MCBCH.8L8.B2, MCBCH.10L8.B2 and MCBCH.12L8.B2 for B2. The computations of orbit bump amplitudes have been performed considering the beam with largest transverse dimensions, i.e. 6.37 Z TeV energy and 2.3 μm emittance. As a result, the minimum required orbit bumps that can pull the BFPP beam away from the aperture

		Angular kick [rad]	Magnetic field [T]
B1	MCBCH.8R8.B1	-3.94204e-05	1.022
	MCBCH.10R8.B1	-1.21153e-05	0.314
	MCBCH.12R8.B1	-3.15698e-05	0.818
B2	MCBCH.8L8.B2	-3.73127e-05	0.967
	MCBCH.10L8.B2	-1.47736e-05	0.383
	MCBCH.12L8.B2	-2.71897e-05	0.705

Table 4.3: Kicker strengths needed to realize an orbit bump of -5.3 mm on MQML.10R8.B1 and one of +5 mm on MQML.10L8.B2, expressed in terms of angular kick and magnetic field (for a 7 Z TeV beam).

at the first peak of the dispersive trajectory, plus a 3σ beam envelope, are -5.1 mm on MQML.10R8.B1 for B1 and +4.7 mm on MQML.10L8.B2 for B2. These values have been increased up to -5.3 mm and 5 mm respectevely, in order to lose no particle in cell 10 out of the 10000 tracked. The required kicks, reported in Table 4.3, are around 30% of maximum available strength, which for MCBCH kickers is 3.11 T. These orbit bumps can thus be implemented without issue in operation. With the orbit bump in place, the beam loss occurs instead at the second peak of BFPP dispersive trajectory, in cell 12. Closed orbit and BFPP beam trajectories from IP8, with and without orbit bump as calculated by MAD-X, are shown in Fig. 4.4.

The new loss patterns on the magnets have been simulated, repeating the studies with SixTrack (4.1.1), but this time including the implemented orbit bumps in the optics input. The results for 6.37 Z TeV energy and 2.3 μm emittance, i.e. the operating conditions in the 2018 run, are shown in Fig. 4.5. All the BFPP particles of B1 and B2 are now lost at MB.C12R8.B1 and MB.C12L8.B2 respectively, and their impact distributions are much wider than those obtained at MB.B10R8.B1 and MB.B10L8.B2 without orbit bump. This widening can be attributed to the difference in the chromatic β-function, i.e. the β-function with starting conditions calculated for the off-momentum beam. It is larger at the new impact location, and hence the transverse size of the BFPP beam as well as the spot size of the losses are larger. The resulting standard deviations of the loss patterns simulated for the different combinations of emittance and energy are summarized in Table 4.4.

The most concentrated losses have been obtained for B2, 7 Z TeV energy and 1.6 μm emittance, that is the scenario with the smaller transverse beam dimensions. In any simulation case, the loss patterns on MB.C12 are broader than those on MB.B10 by a factor ~5.9 for B1 and ~4 for B2. Thus, an orbit bump performed around the first peak of dispersion function could bring two main benefits in view of maximizing the levelling target for LHCb luminosity: i) it would avoid the risk of symmetric quench in cell 10, allowing to take advantage of the higher BLM threshold in cell 12; ii) it would lower the local temperature increase thanks to the wider impact distributions, ensuring a less severe risk of magnet quenching.

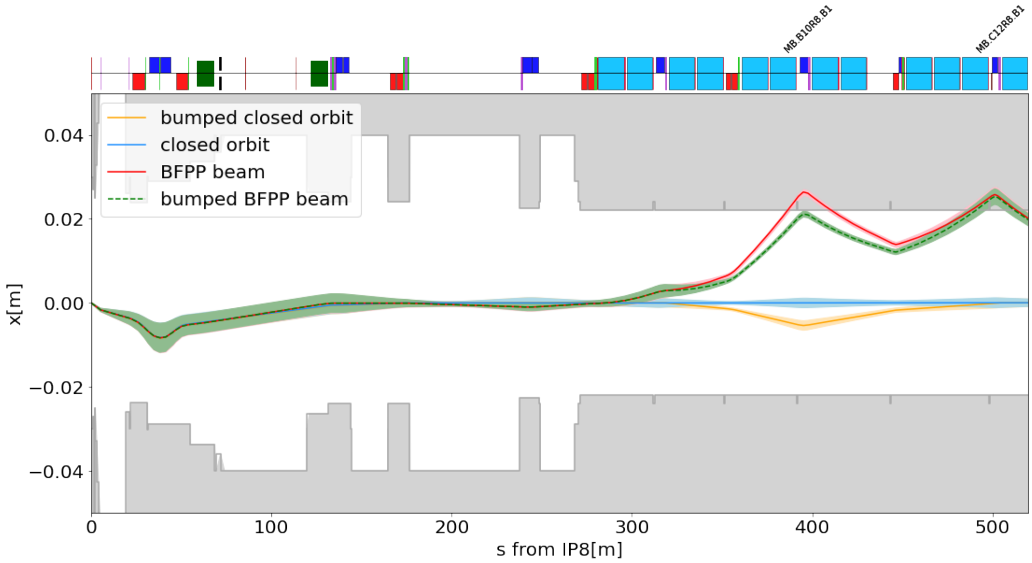

(a) Beam 1.

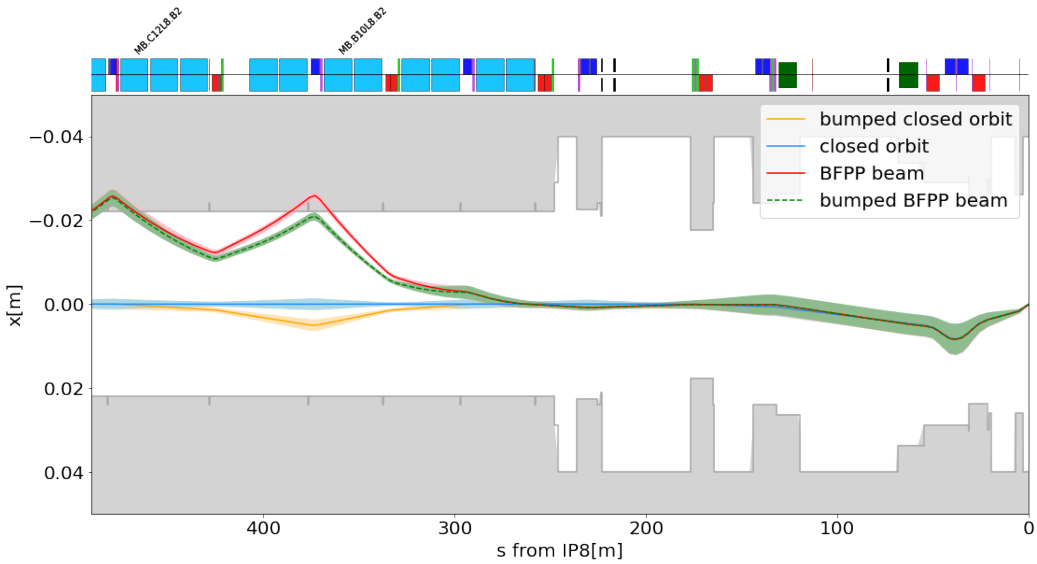

(b) Beam 2.

Figure 4.4: Trajectories computed by MAD-X with and without orbit bump for both B1 and B2 (3σ envelopes). The aperture of the machine is represented by the grey shaded area.

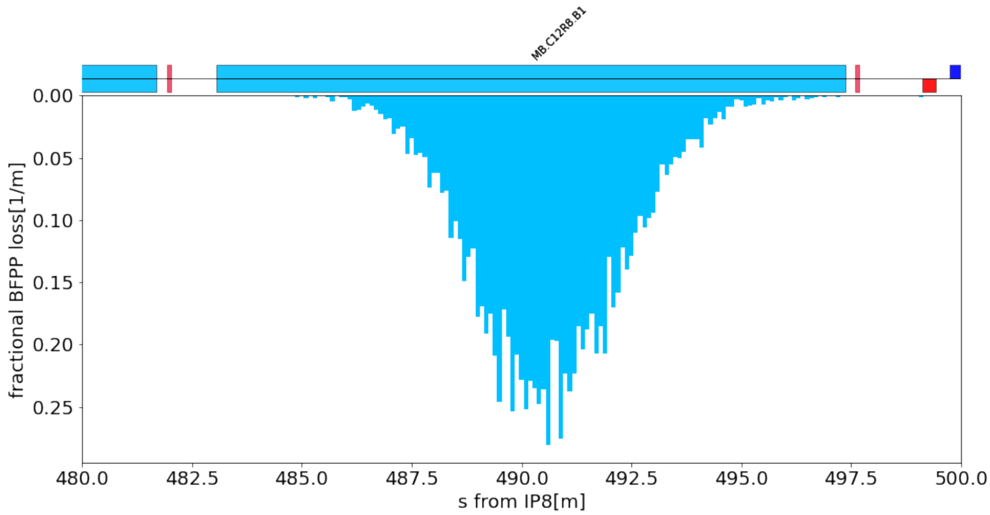

(a) Beam 1, losses at 490.619 ± 1.657 m.

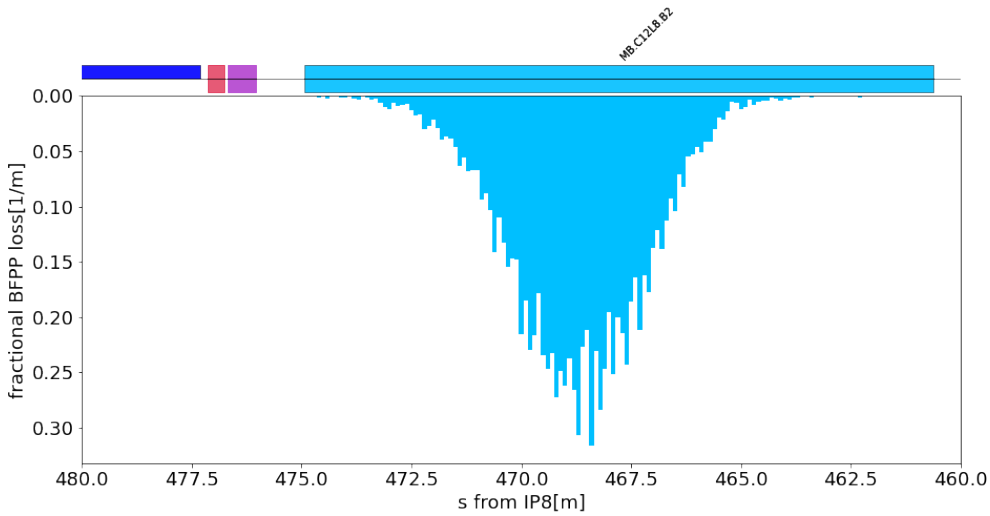

(b) Beam 2, losses at 468.724 ± 1.507 m.

Figure 4.5: BFPP loss patterns on MB.C12R8.B1 and MB.C12L8.B2, simulated for an energy of 6.37 Z TeV and an emittance of 2.3 μm with SixTrack. The coordinate axis has $s = 0$ at IP8.

		B1 ($s = 490.6$ m)	**B2** ($s = 468.7$ m)
6.37 Z TeV	1.6 μm	1.383 m	1.256 m
	2.3 μm	1.657 m	1.507 m
7 Z TeV	1.6 μm	1.319 m	1.199 m
	2.3 μm	1.582 m	1.438 m

Table 4.4: Standard deviations of loss patterns of BFPP beams deflected with orbit bumps for different values of emittance and energy.

The results of this simulation have been used as input in another study [28] to estimate the power load on the superconductive coils of MB.B10R8.B1 and MB.C12R8.B1 in the two scenarios, with and without orbit bump. In this FLUKA study it has been assumed a beam energy of 6.37 Z TeV, an instantaneous luminosity of 10^{27} cm^{-2}s^{-1} at IP8, two possible normalized transverse emittances of 2.3 and 1.6 μm. From the case with 1.6 μm normalized transverse emittance, it results that the maximum radially averaged power density is ∼12 mW/cm^3 without bump and ∼3 mW/cm^3 with the orbit bump (Fig. 4.6). This confirms that the partial alleviation of BFPP losses around IP8 through orbit bumps, proposed in this thesis, would be possible. It would allow to safely increase the levelled luminosity of IP8 by a factor 2–3 in future runs.

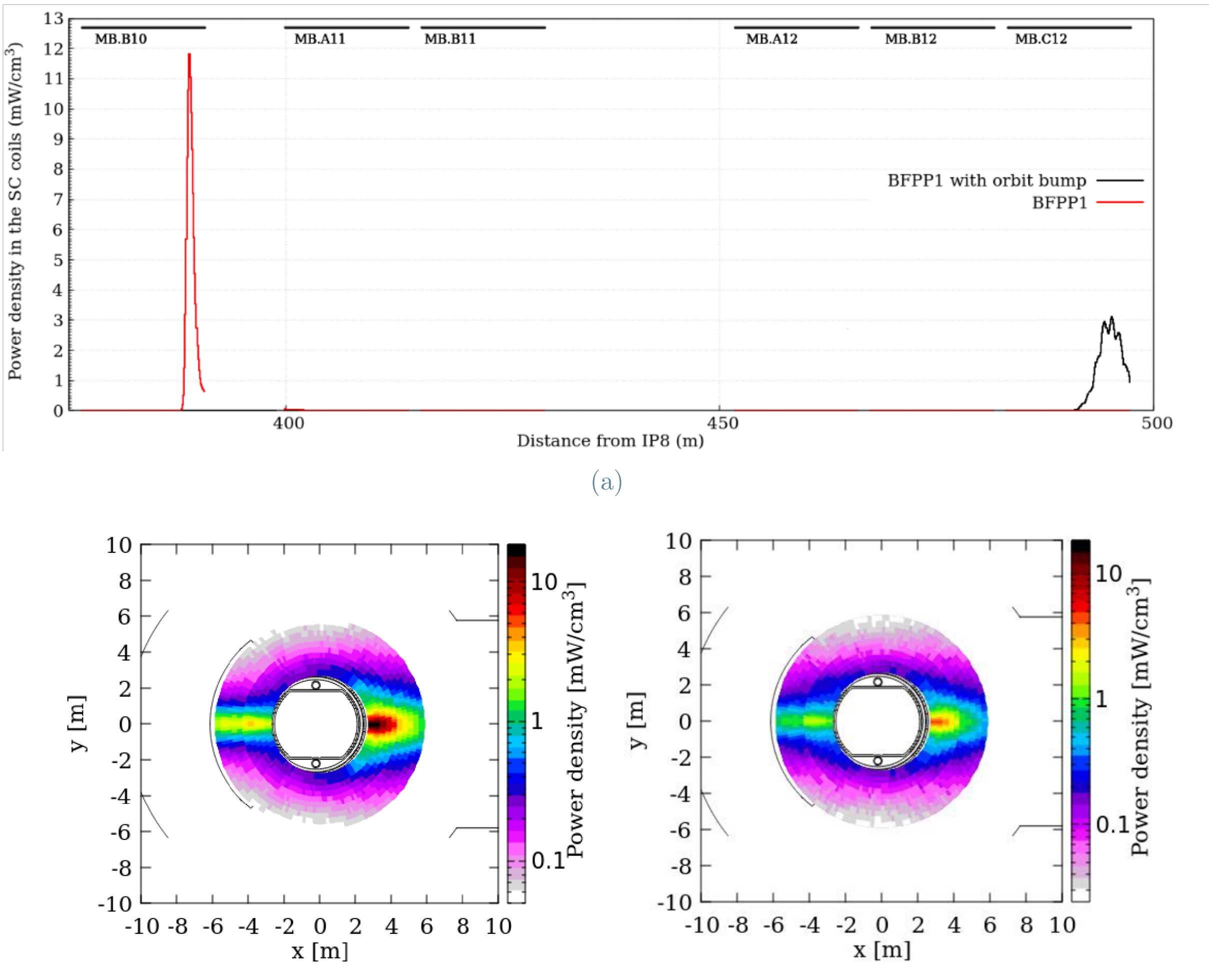

(a)

(b) Power load without orbit bump

(c) Power load with orbit bump

Figure 4.6: FLUKA simulation of power load on the superconductive coils caused by BFPP beam emerging from IP8. A luminosity of 10^{27} cm^{-2}s^{-1} and a normalized transverse emittance of 1.6 μm have been assumed. Courtesy of Alessia Ciccotelli [28].

4.2. Simulations of losses from EMD and inelastic interactions

The SixTrack-FLUKA coupling, together with the possibility of setting up a beam-beam collision source in FLUKA, gives the opportunity to simulate the losses arising around LHC ring due to interactions occurring at the experiments. The products from inelastic and EMD interactions between two $^{208}\mathrm{Pb}^{+82}$ beams at flat top energy can be sampled by a FLUKA collision source inside an IP pipe geometry. The collision products can then be sent back to SixTrack for standard tracking along LHC lattice.

The analysis of B1 collision products and relative losses from Pb-Pb collisions in IP1 is shown in the following. A similar procedure has been followed systematically to simulate each of the physical processes occurring in the collisions, and the results are added up to obtain the so-called collisional master lossmap. For the simulation, the LHC optics employed in 2018 for Run 2 (see Table 2.1) has been used. A normalized emittance of 2.3 μm in both x and y planes, a bunch length of 1.1 ns, an energy of 6.37 Z TeV and a momentum spread of 1.06e-4 have been assumed for the beam [25, 39]. The collision source has been setup to have a target beam that mimics B2: it is a twin beam of $^{208}\mathrm{Pb}^{+82}$ ions coming from the opposite direction but with the same parameters as B1. EMD and nuclear inelastic interactions have been activated separately in order to individually study their effects. A total sample of 10^5 ions, with an initial Gaussian distribution in space before the interactions take place, has been assumed in each simulation. FLUKA samples the collisions with a longitudinal profile following a Gaussian distribution, centered at the middle of the IP1 pipe geometry. A standard deviation of 5.83 cm is chosen, taking into account that the distribution of collision points in space is still a Gaussian but narrower than the bunch distribution by a factor $\sqrt{2}$, as explained in Subsec. 4.1.1. A characterization of the products of the two types of interaction is provided below. An analysis of the simulated losses arising from this simulation setup follows.

4.2.1. EMD

The distribution of products from EMD in Pb-Pb collision at 6.37 Z TeV energy per beam is shown through a nuclide chart in Fig. 4.7. Most of them are light nuclei, such as protons, deuterium, tritium and alphas, coming from the nuclear evaporation of the original $^{208}\mathrm{Pb}^{+82}$ ions. Indeed, the nuclides around $^{208}\mathrm{Pb}^{+82}$ form another peak of concentration. A minor part of the products is given by intermediate nuclides generated by nuclear fragmentation. In this context the fragmentation processes are induced by

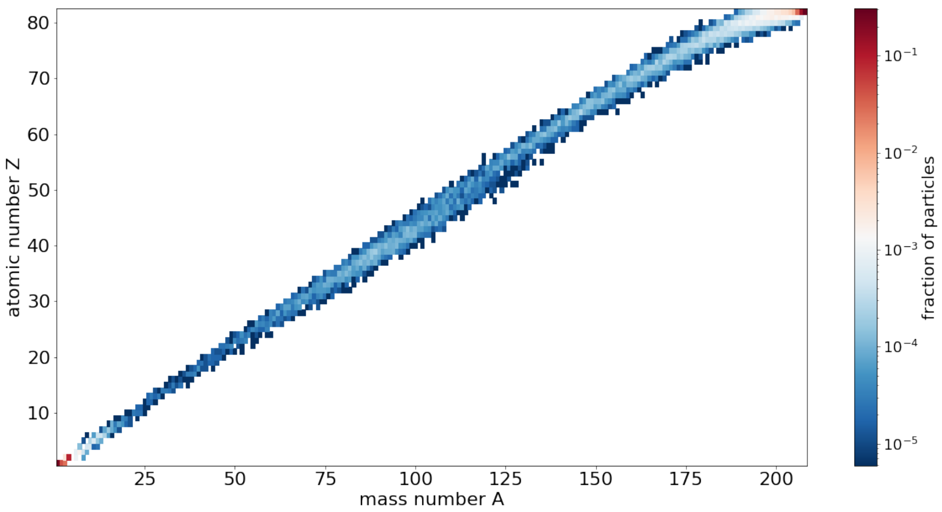

Figure 4.7: Nuclide chart of EMD products from Pb-Pb collisions simulated with 6.37 Z TeV beam energy. The interactions have been simulated by FLUKA DMPJET3 event generator.

(virtual) photon-nuclear interactions.

Figure 4.8 illustrates instead the distributions of scattering angle and energy per nucleon. These scattering angles are determined as the angles of the products with respect to the angle of the initial ion before the interaction. This distribution evidently shows the peripheral nature of EMD. Only a small fraction of particles, of the order of 10^{-5}, has a scattering angle greater than 0.02 rad. The distribution of energy of the products is peaked around the original beam value of 2511.25 GeV/nucleon (indicated by a red dashed line).

However, the dynamics for different particles with similar energy per nucleon can still be quite different. Therefore, we study also the distribution in magnetic rigidity (1.5), displayed in Fig. 4.9a. This is of particular interest since all the particles having a magnetic rigidity different from the value for main beam follow different dispersive trajectories and could hence be lost. From a simple visualization, it can be seen that the distribution shows several contributions. An attempt has been made to study which ion species give rise to the different clusters. The clusters have been arbitrarily isolated and highlighted in different colours. The one in red is centered around the main beam value of 21248.03 Tm and is the most prominent one. The distribution of mass number A has been studied separately for the products of each cluster, and plotted with the corresponding colour coding in the same histogram in Fig. 4.9b (for each colour the sum of the bins gives the unity). For instance, the major contribution to the red area of rigidity distribution

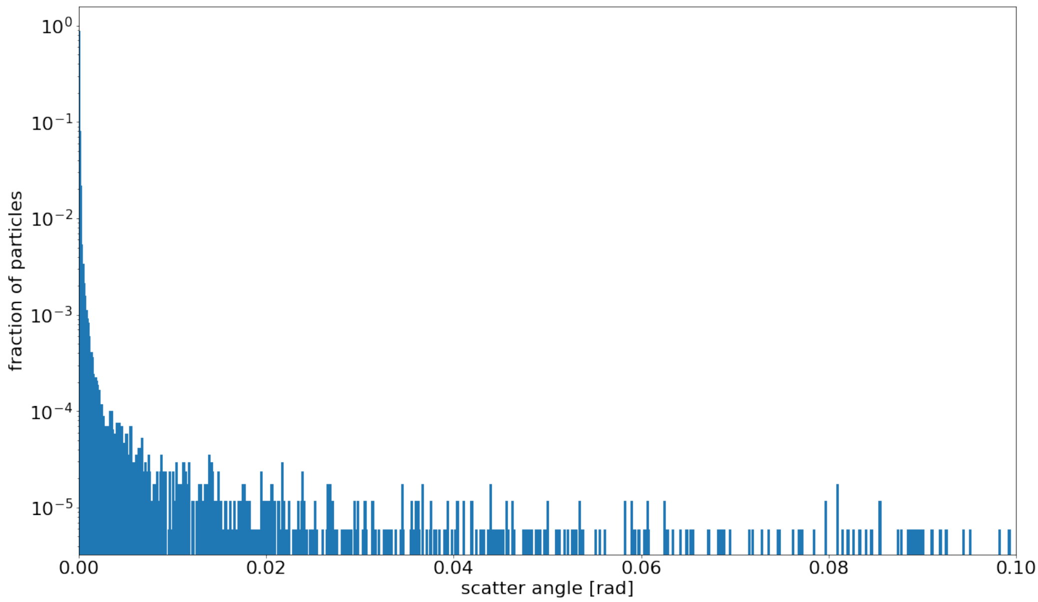

(a) Distribution of scattering angles.

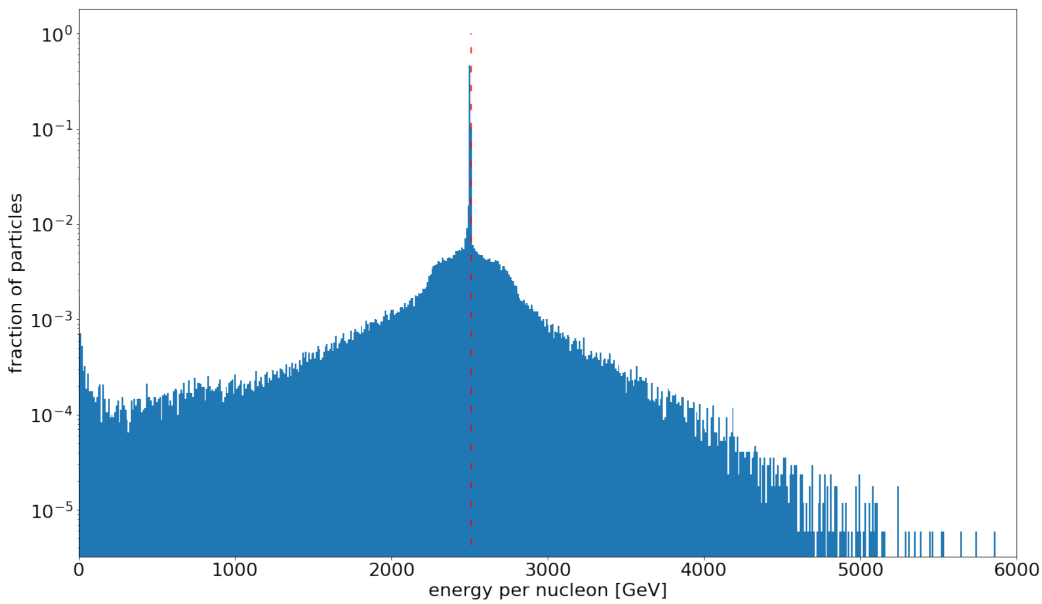

(b) Distribution of energy per nucleon. The red dashed line indicates the energy per nucleon of the original beam.

Figure 4.8: Distributions of scattering angles (a) and energy per nucleon (b) for EMD products from Pb-Pb collisions simulated with 6.37 Z TeV beam energy. The interactions have been simulated by FLUKA DMPJET3 event generator.

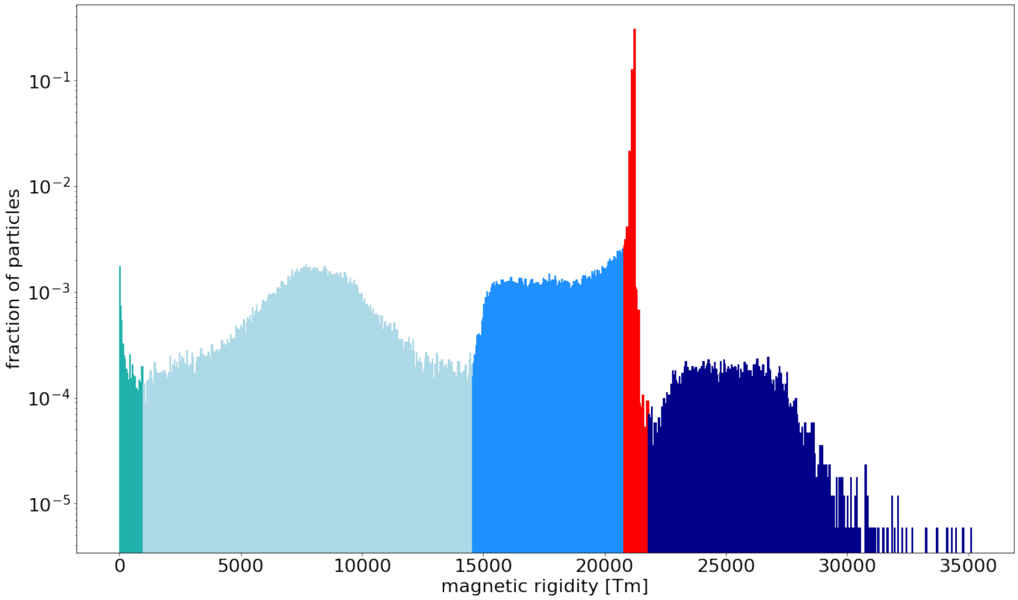

(a) Distribution of magnetic rigidity. The portion in red indicates a range around the original magnetic rigidity of 21248.03±500 Tm.

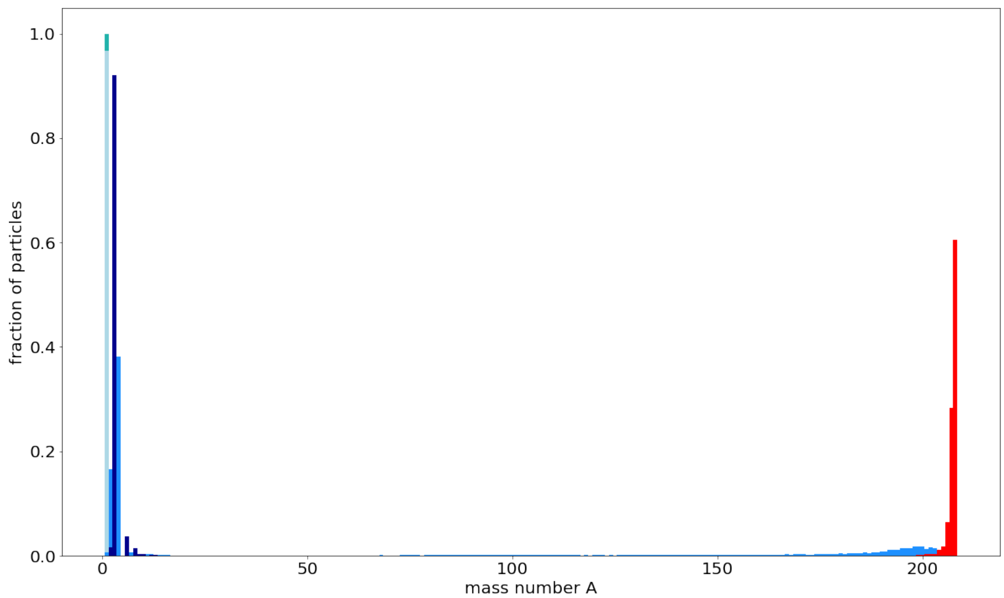

(b) Distribution of nuclide mass number for each portion of the magnetic rigidity distribution.

Figure 4.9: Distributions of magnetic rigidity (a) and contributing-particle mass number (b) for EMD products from Pb-Pb collisions simulated with 6.37 Z TeV beam energy. The interactions have been simulated by FLUKA DMPJET3 event generator.

comes from the heaviest ions. These are the ions undergoing EMD that lost only few neutrons or protons and which are most likely lost later. The lighter nuclides contribute to the remainder of the distribution. Specifically, the peak below 1000 Tm is given by the lowest energy protons, while the second, distinguishable between 1000 and 14500 Tm, by more energetic protons coming from a different EMD reaction channel. The following plateau above 14500 Tm is mainly due to alphas and deuterium. The last cluster above 21748.03 Tm mostly consists of tritium.

4.2.2. Inelastic interactions

Figure 4.10 shows the nuclide chart for the products of inelastic interactions. The distribution only peaks around the lightest ions, particularly protons, deuterium, tritium and alpha particles. The fraction of products close to $^{208}Pb^{+82}$ is much less significant, since inelastic interactions tend to fragment the lead ions more than EMD.

Another important difference between the two interactions can be seen in the distribution of scattering angles (Fig. 4.11a). Inelastic interaction produces on average scattering angles of one order of magnitude (10^{-1} rad) larger than EMD. The distribution of energy per nucleon (Fig. 4.11b) has a similar shape to the one arising from EMD but with a greater contribution of low energy protons, which are even more abundant than the products with the initial value of 2511.25 GeV/nucleon (red dashed line on the histogram).

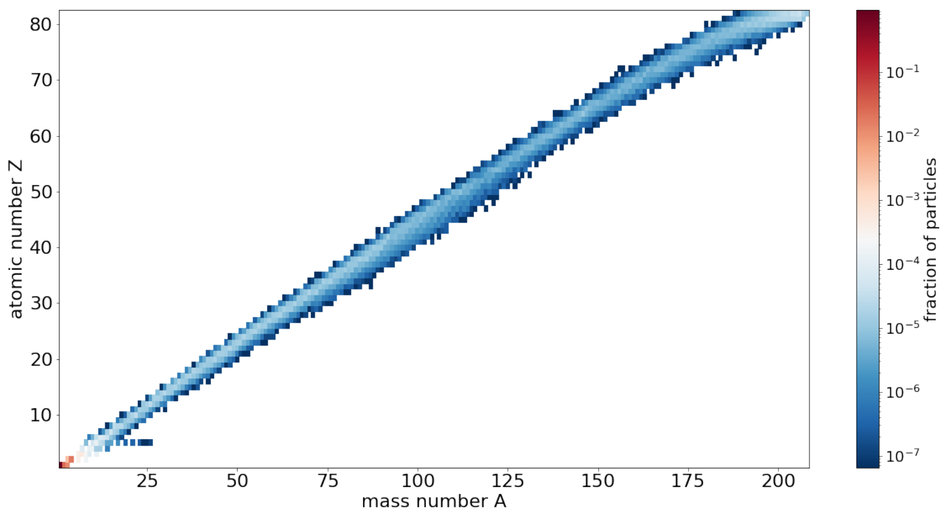

Figure 4.10: Nuclide chart of inelastic interaction products from Pb-Pb collisions simulated with 6.37 Z TeV beam energy. The interactions have been simulated by FLUKA DMPJET3 event generator.

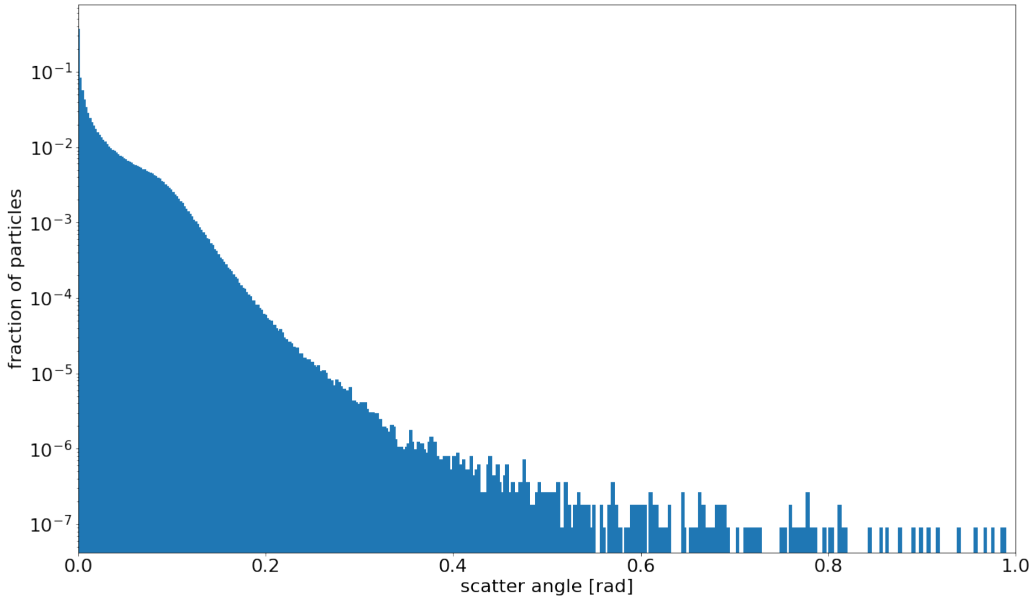

(a) Distribution of scattering angles.

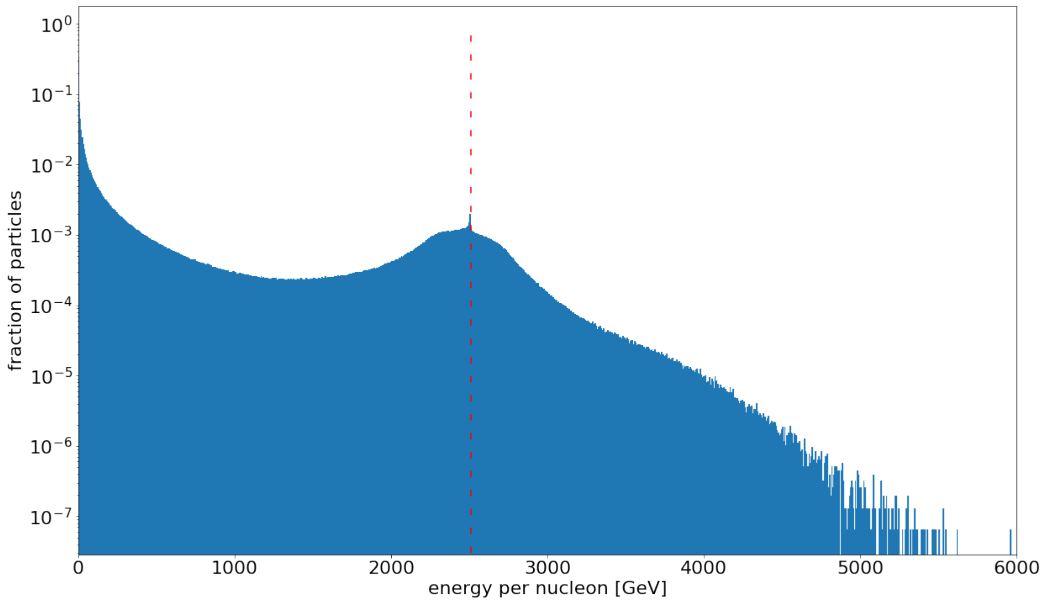

(b) Distribution of energy per nucleon. The red dashed line indicates the energy per nucleon of the original beam.

Figure 4.11: Distributions of scattering angles (a) and energy per nucleon (b) for inelastic interaction products from Pb-Pb collisions simulated with 6.37 Z TeV beam energy. The interactions have been simulated by FLUKA DMPJET3 event generator.

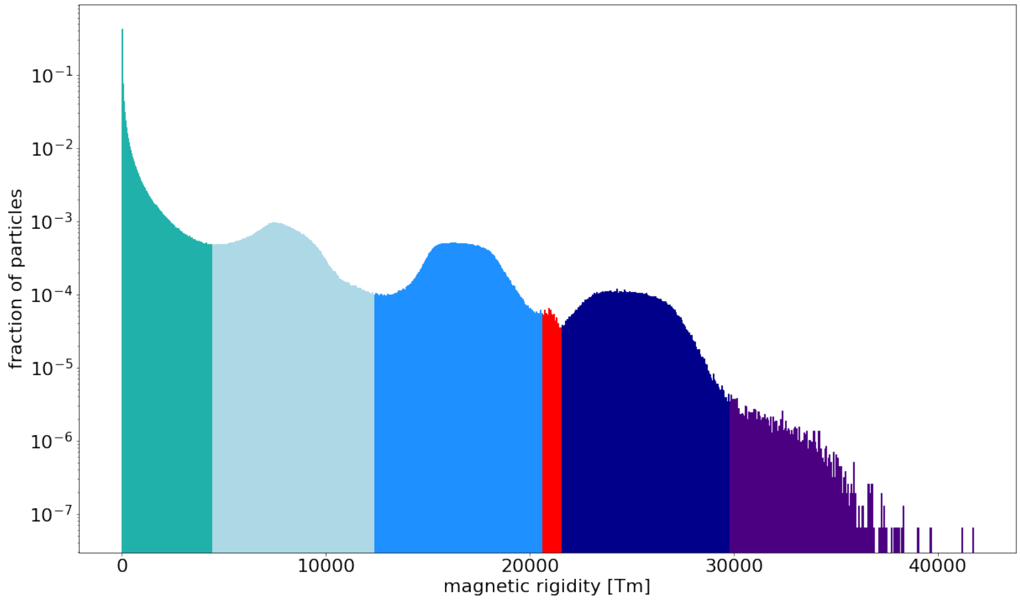

(a) Distribution of magnetic rigidity. The portion in red indicates a range around the original magnetic rigidity of 21248.03±500 Tm.

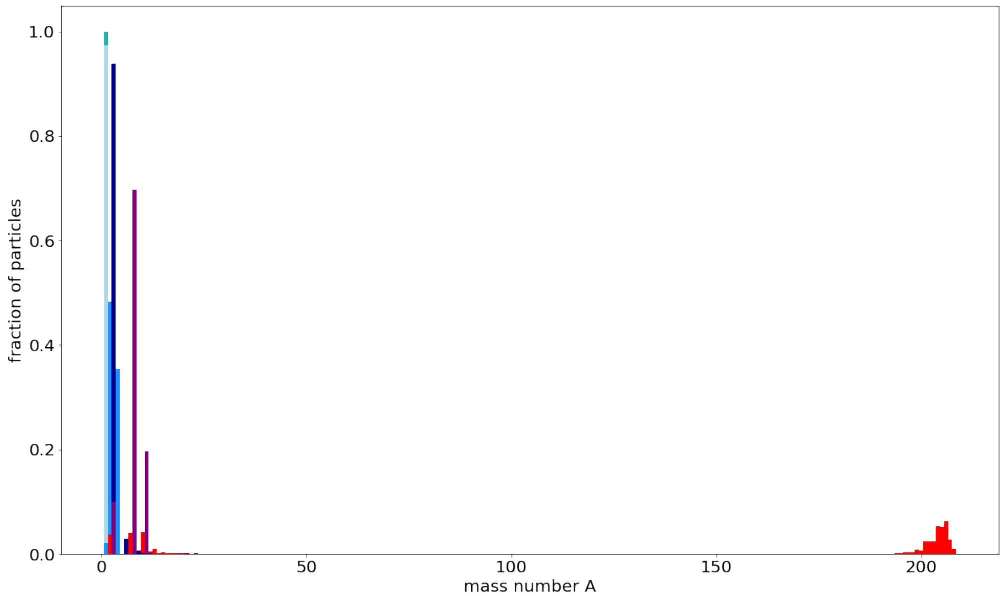

(b) Distribution of nuclide mass number for each portion of the magnetic rigidity distribution.

Figure 4.12: Distributions of magnetic rigidity (a) and contributing-particle mass number (b) for inelastic interaction products from Pb-Pb collisions simulated with 6.37 Z TeV beam energy. The interactions have been simulated by FLUKA DMPJET3 event generator.

From these observations it can be expected that the magnetic rigidity is poorly preserved after inelastic collisions. This is confirmed by the distribution of magnetic rigidity (4.12a) not showing a peak around the main-beam value of 21248.03 Tm (red area). This distribution has been analysed in a similar way to that from EMD products in the previous subsection. The numerous collision products responsible for the different peaks of the distribution are displayed in Fig. 4.12b with the corresponding colour coding. Again, the distribution of magnetic rigidity is dominated by low energy protons, giving the highest peak. Protons with larger energy produce instead the cluster between 4500 and 12500 Tm. The third cluster is mostly given by deuterium and alphas, whereas the one above the initial rigidity by tritium. Among the several ions contributing to the red cluster, centered around the original value of magnetic rigidity, a significant fraction is given by heavy ions with $A > 200$. They are dominated by isotopes of lead and thallium. The tail above 30000 Tm mainly consists of $^{8}\mathrm{He}^{+2}$ and $^{11}\mathrm{Li}^{+3}$.

4.2.3. Losses

The losses in the LHC ring arising from the B1 collision products studied above, emerging from IP1, are reported in two separate lossmaps for the EMD and inelastic interactions in Fig. 4.13. The shown losses are labeled as "collimator", "cold" and "warm", depending on whether they occur at a collimator, at a superconducting magnet or elsewhere, respectively. They have been normalized to express the power load in W/m around LHC ring for the IP1 peak luminosity of 2018 run (see Table 2.1). This can be accomplished first by normalizing them by a bin width of 10 cm, then dividing them by the total number of interactions simulated and multiplying them by the IP luminosity and the interaction cross section for each studied process. The cross sections considered for the normalization are those reported in Ref. [24] for Pb-Pb collisions at 6.37 Z TeV beam energy, and specifically 223 b for EMD and 7.7 b for inelastic interactions. The abscissa indicates the longitudinal coordinate s in metres for the entire LHC ring, travelled clockwise, following B1 and with $s = 0$ at IP1. For this reason the losses from B1 collision debris are observed only at the right side of IP1.

For both interaction types, the losses are clustered in the immediate vicinity after IP1 and in the two cleaning regions, IR3 and IR7 in order. The main difference between EMD and inelastic interaction losses is the relative significance of the losses in IR3 with respect to those around IP1. In EMD the scattering angles are very small and many ions retain a value of magnetic rigidity close to the initial one. These products can stay within the ring aperture for a longer distance, being eventually removed by IR3 collimators. Since a particle with a charge different from that of main beam particles has also a different

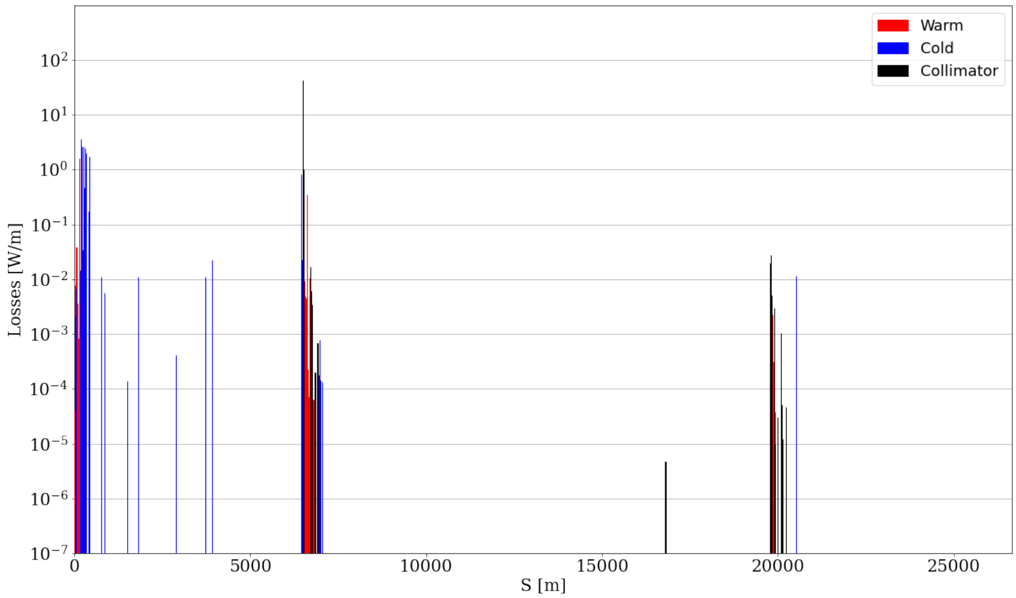

(a) Losses from EMD products.

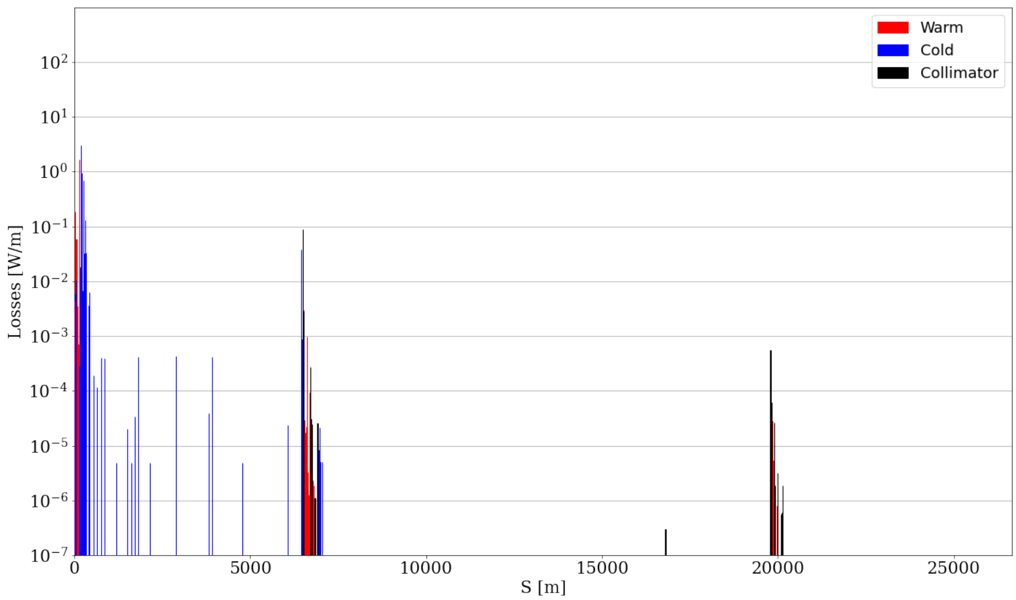

(b) Losses from inelastic interaction products.

Figure 4.13: Simulation of B1 losses from EMD (a) and inelastic interactions (b) in Pb-Pb collisions in IP1 at 6.37 Z TeV beam energy and $6.1\times10^{27}\text{cm}^{-2}\text{s}^{-1}$ luminosity. The losses have been simulated with the SixTrack-FLUKA coupling, setting up a collision source in IP1.

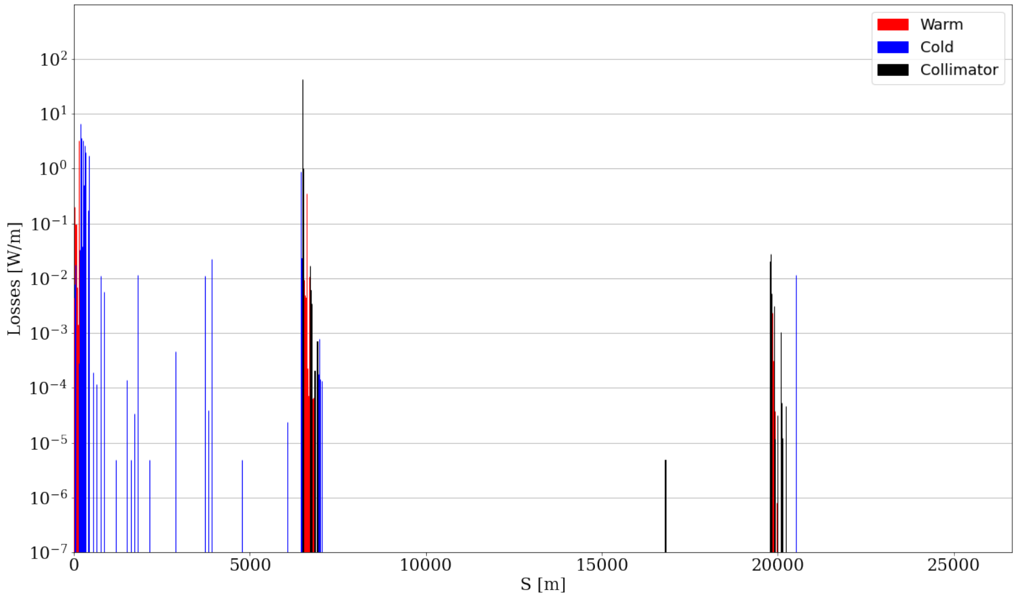

Figure 4.14: Combination of B1 losses from EMD and inelastic interactions in Pb-Pb collisions in IP1 at 6.37 Z TeV beam energy and $6.1{\times}10^{27}\mathrm{cm}^{-2}\mathrm{s}^{-1}$ luminosity. The losses have been simulated with the SixTrack-FLUKA coupling, setting up a collision source in IP1.

magnetic rigidity, it follows a dispersive trajectory just like an off-momentum one. Because of this, IR3 cleans out most of the off-rigidity particles that make it here, i.e. in particular $^{207}\mathrm{Pb}^{+82}$ ions from EMD1. Figure 4.13a clearly shows that losses from EMD are larger by about one order of magnitude in IR3 than at IR1. On the contrary, inelastic interactions have larger scattering angles and more fragmentation of beam ions. As a result only a small fraction inelastic products conserve a good value of magnetic rigidity and most of them are lost close to IP1 (4.13b). The contributions from the two types of interaction are added up in Fig. 4.14.

In order to have a quantitative analysis of which particles give rise to the different losses around the ring, the distribution of main nuclides has been studied for each loss bin. Figures 4.15, 4.16 and 4.17 show three zooms of the lossmap in Fig. 4.14, on IP1 right side and at the beginning of the two cleaning regions respectively, together with a colour code displaying the contribution from the different particles to the respective losses. Each loss bar has been coloured proportionally to the fraction of ions lost in the corresponding bin, using a different colour for each of the main nuclides (the logarithmic scale in the y-scale does not apply to these fractional losses). The losses at the extreme proximity of the collision point are caused almost only by protons. Light ions as deuterium, tritium

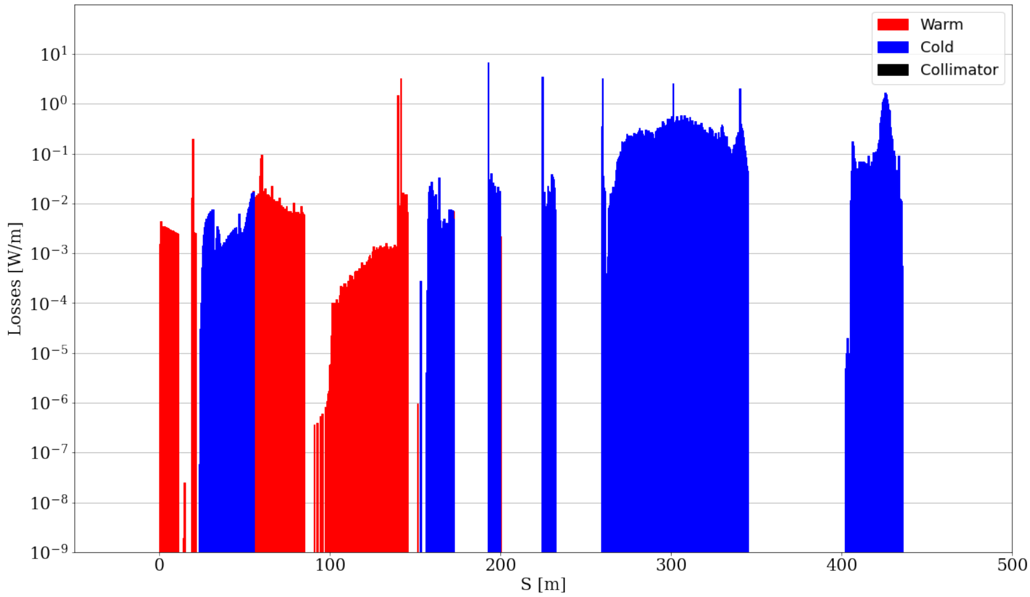

(a) Zoom on IP1 right side.

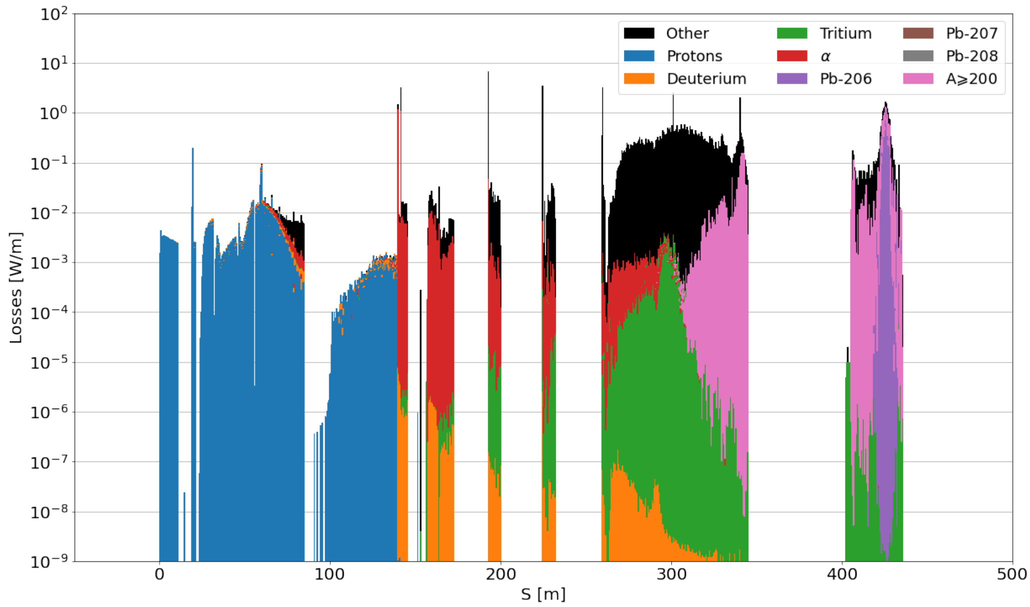

(b) Contribution from main ions to losses.

Figure 4.15: Zoom of the lossmap in Fig. 4.14 on the right side of IP1 (a) and mask showing the contribution from main nuclides (b). The contributions are shown in terms of fractional number of particle lost in a bin (the logarithmic scale in the y-scale does not apply to these fractional losses).

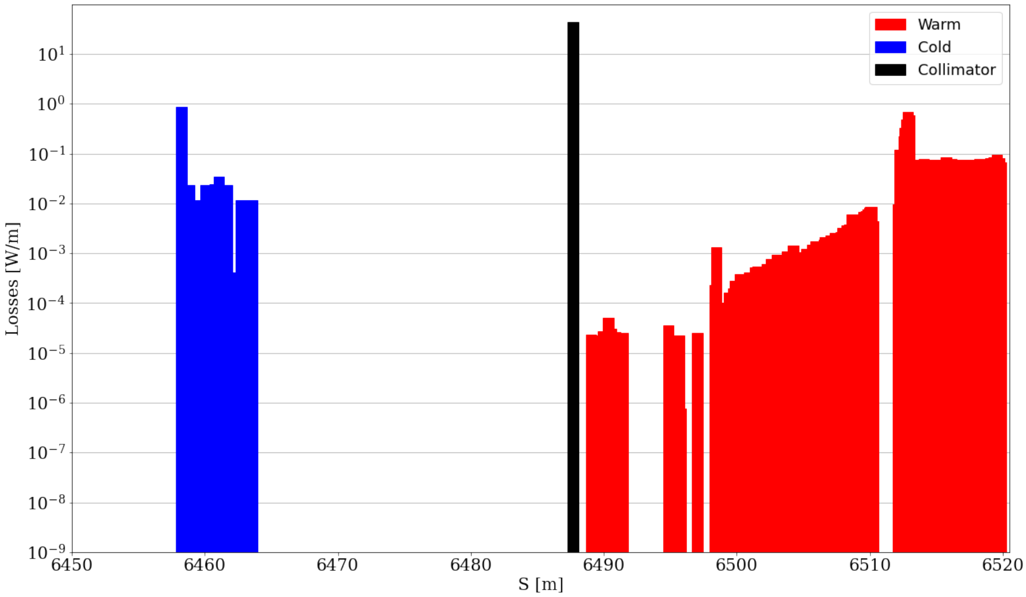

(a) Zoom at the beginning of IR3.

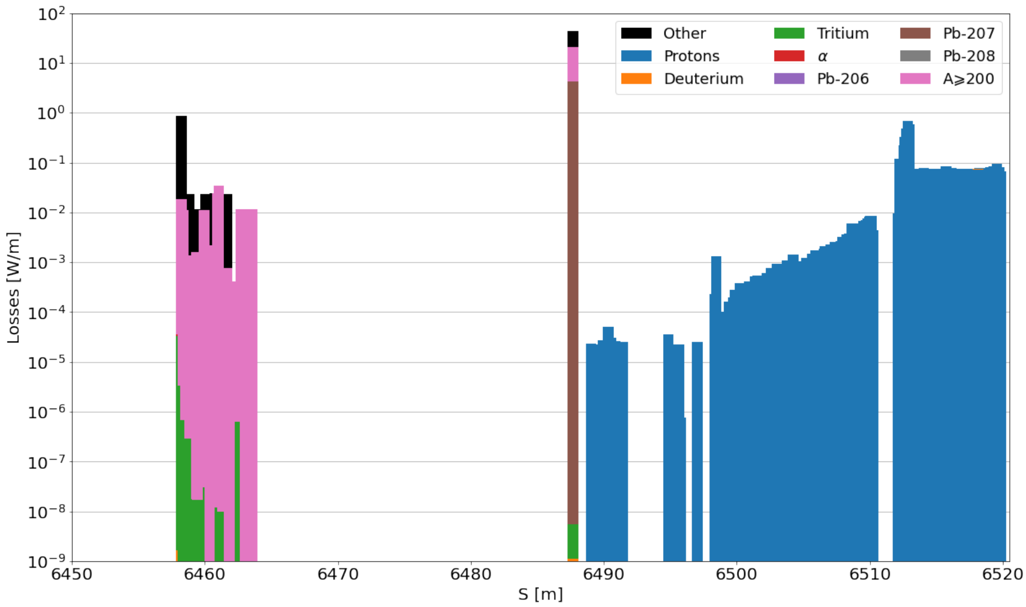

(b) Contribution from main ions to losses.

Figure 4.16: Zoom of the lossmap in Fig. 4.14 at the beginning of IR3 (a) and mask showing the contribution from main nuclides (b). The contributions are shown in terms of fractional number of particle lost in a bin (the logarithmic scale in the y-scale does not apply to these fractional losses).

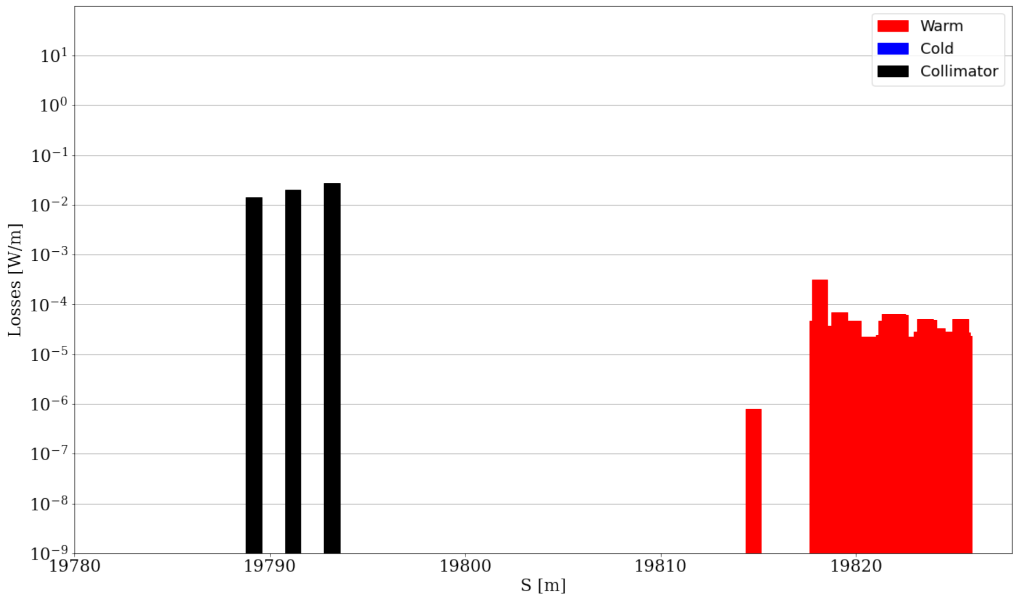

(a) Zoom at the beginning of IR7.

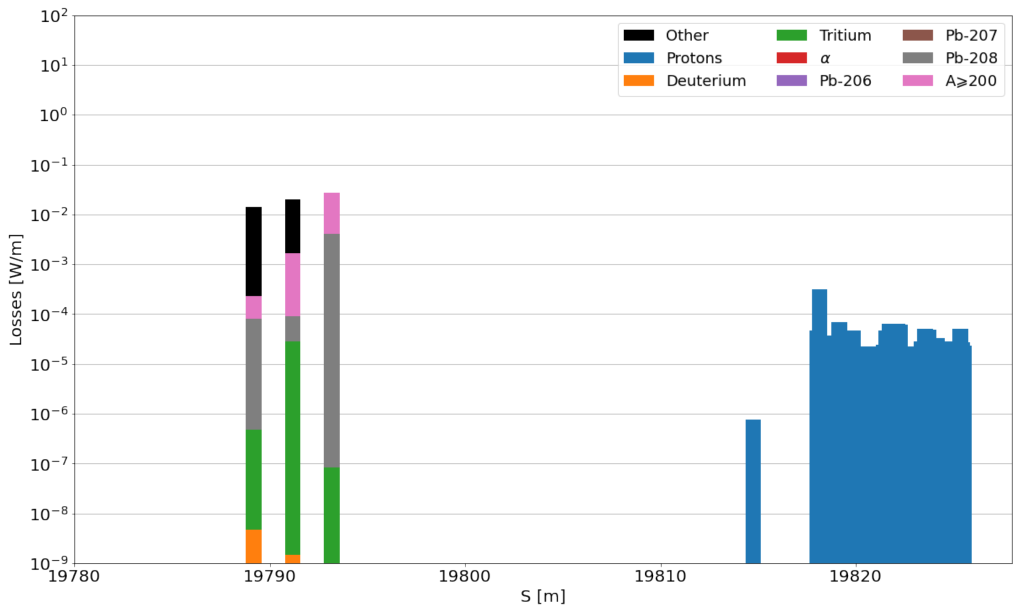

(b) Contribution from main ions to losses.

Figure 4.17: Zoom of the lossmap in Fig. 4.14 at the beginning of IR7 (a) and mask showing the contribution from main nuclides (b). The contributions are shown in terms of fractional number of particle lost in a bin (the logarithmic scale in the y-scale does not apply to these fractional losses).

and alpha particles dominate the losses between 150 and 300 m downstream of IP1. Heavy ions ($A \geq 200$) contribute to the losses starting from 300 m and the localised peak of losses given by $^{206}Pb^{+82}$ ions from EMD2 (see Subsec. 2.3.1) can be observed at about 430 m.

Figure 4.16b clearly shows that the losses just before IR3 are mainly caused by heavy ions and that almost all the particles striking the primary collimator TCP.6L3.B1 are $^{207}Pb^{+82}$ ions from EMD1. The losses downstream of the collimator instead consist only of protons escaping the collimator jaws where they are produced from the interaction of the ions. Finally, the zoom at the beginning of IR7 shows that the few $^{208}Pb^{+82}$ ions preserving their nuclear structure after interacting come this far and are intercepted by the primary collimators TCP.D6L7.B1, TCP.C6L7.B1 and TCP.B6L7.B1. Some other heavy fragments can also reach IR7, as well as tritium and small amounts of deuterium.

In conclusion, the simulations show that light ion fragments are primarily lost close to the interaction point where they were created, due to a typically large offset in magnetic rigidity with respect to the main beam. Heavy fragments emerging from IP1, primarily created through EMD, travel further, with $^{206}Pb^{+82}$ causing localised losses at the DS, and $^{207}Pb^{+82}$ hitting the IR3 primary collimator. A small amount of particles, including all the $^{208}Pb^{+82}$ ions produced, reach also IR7.

4.3. Simulation of 2018 master lossmap

In Sec. 4.2 it has been shown how the losses caused by the collision products from EMD and inelastic interactions occurring in an IP can be simulated. Instead, a method to simulate the trajectory of BFPP particles from a collision point and the relative losses has been explained in Sec. 4.1. Repeating these two procedures for each IP and both beams and combining together all the results, it is possible to reproduce what we call a master lossmap, predicting the losses that are observed during Pb-Pb collisions. The simulation was carried out for 2018 operating conditions, taking again fill #7477 with timestamp $2018-11-26\ 22:45$ as reference. The simulation assumptions are reported in Table 4.5.

Optics	Run 2 2018
Beam energy	6.37 Z TeV
Normalized emittance	2.3 μm
Momentum spread	1.06e-04
Bunch length	1.1 ns

Table 4.5: Assumptions for 2018 Pb-Pb master lossmap simulation.

For what concerns EMD and inelastic interaction losses, a total sample of 10^6 $^{208}\mathrm{Pb}^{+82}$ ions has been simulated with SixTrack-FLUKA coupling for each beam, IP and interaction. BFPP losses have been added, tracking with SixTrack 10^5 off-momentum ($\frac{82}{81} \times 6.37$ Z TeV/c) $^{208}\mathrm{Pb}^{+82}$ ions from each IP, for both beams. Then, the so computed losses have been normalized with the same procedure adopted in the previous section, in order to express the actual power load in W/m around LHC ring for the reference timestamp. The reference values for fill #7477 are listed in Table 4.6.

The resulting lossmaps with all relevant collisional processes included are presented in Fig. 4.18, and they are first shown separately for each IP. In each of them the losses are clustered around the IP where collisions are simulated and in correspondence of the cleaning regions. Both IR3 and IR7 always present an asymmetric pattern of losses, which depends on the location of the IP from which the collisional debris comes from. This can be understood by studying the layout of the LHC ring (Fig. 2.2) and the order in which outgoing collision products encounter the other IRs. B1 collisional debris from IP1, IP2 and IP8 is cleaned first by IR3 collimators and then by IR7 ones. Vice-versa, B2 collisional debris from IP1, IP2 and IP8 is cleaned first by IR7 collimators. For this reason, the collisional lossmaps of these IPs have higher losses at B1 collimators of IR3 and B2 collimators of IR7. Following the same reasoning, the opposite is true for IP5 collisional lossmap, where B2 collimators of IR3 and B1 collimators of IR7 have the higher losses.

These four lossmaps have been combined in the master lossmap in Fig. 4.19. As expected, the normalization gives higher losses around the experiments with higher luminosity, IP1 and IP5, where more intense collisional debris is observed. A minor part of the losses occurs around IR6, due to the collimators placed in this region and to the hadronic showers triggered by their interaction with the beam. The asymmetry in IR3 and IR7 loss patterns is still present in the master lossmap, since only IP5 out of the four experiments contributes to the losses with highest contributions on the sides of IR3 and IR7 that are closer to IR5. The highest losses are given by the localized BFPP peaks, found at each side of each IP, and IR3 primary collimators which, as explained in Section 4.2, remove

$\mathcal{L}_{IP1}$	5.2233e27 $\mathrm{cm^{-2}s^{-1}}$
$\mathcal{L}_{IP2}$	9.9820e26 $\mathrm{cm^{-2}s^{-1}}$
$\mathcal{L}_{IP5}$	5.2296e27 $\mathrm{cm^{-2}s^{-1}}$
$\mathcal{L}_{IP8}$	9.7746e26 $\mathrm{cm^{-2}s^{-1}}$

σ_{EMD}	223 b
σ_{BFPP1}	278 b
σ_{inel}	7.7 b

Table 4.6: Luminosity values extracted from logged data at $2018-11-26$ $22:45$ and process cross sections for Pb-Pb collisions at 6.37 Z TeV beam energy [24].

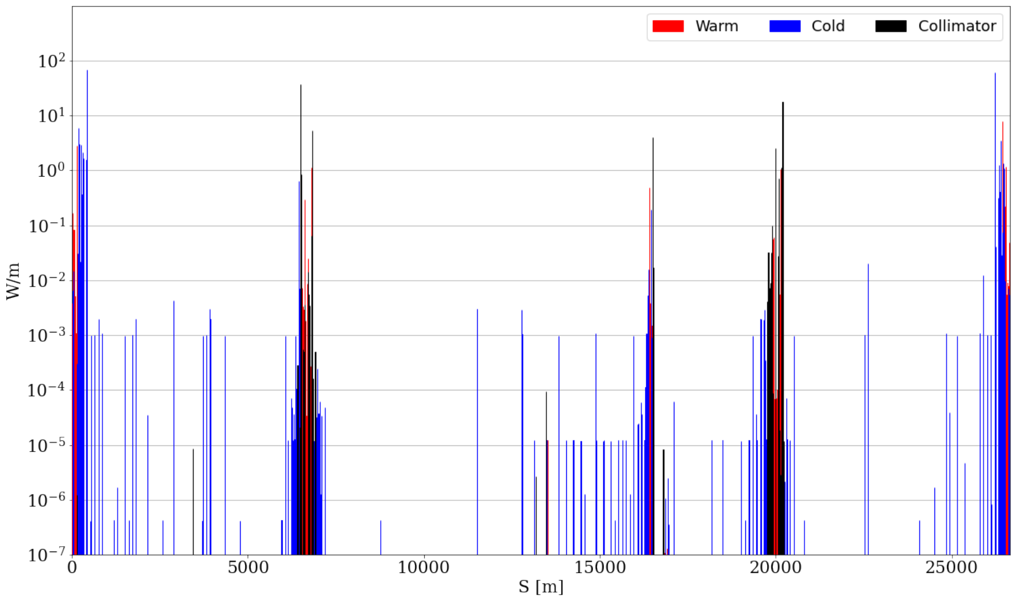

(a) Losses from IP1 collision debris.

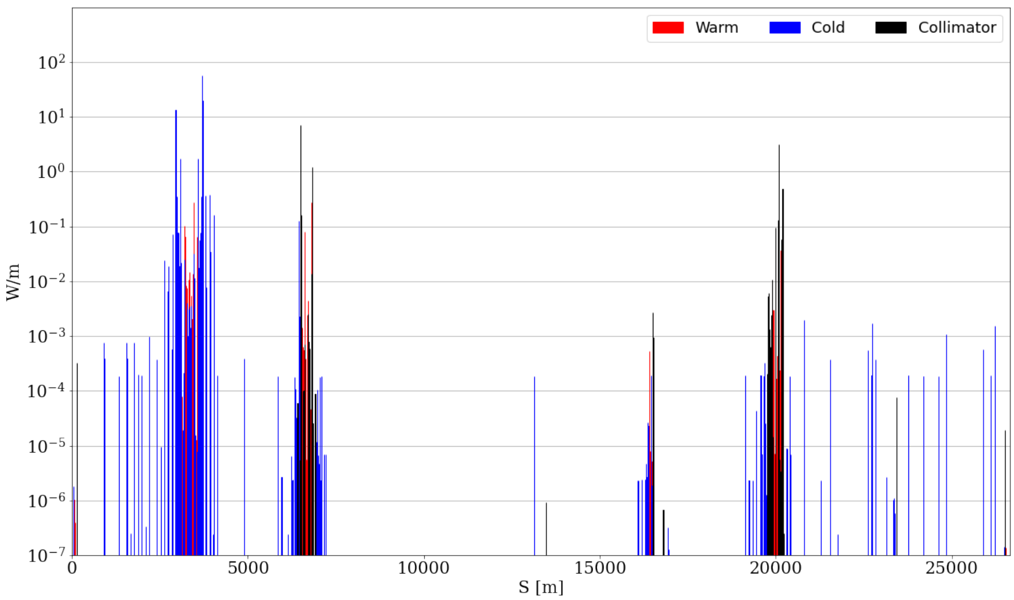

(b) Losses from IP2 collision debris.

Figure 4.18: SixTrack-FLUKA simulation of 2018 Pb-Pb collisional lossmaps for the four experiments.

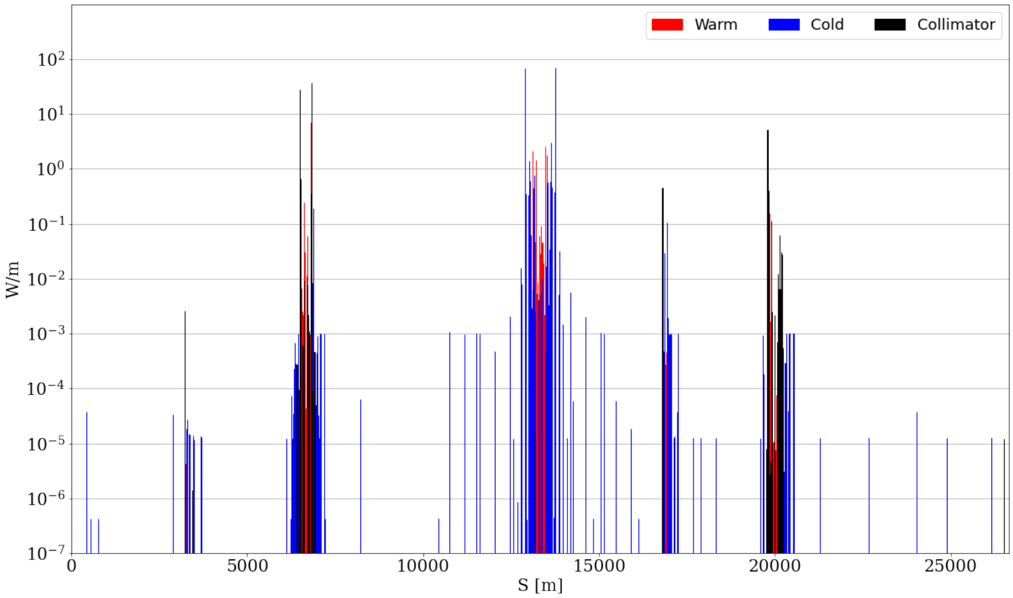

(c) Losses from IP5 collision debris.

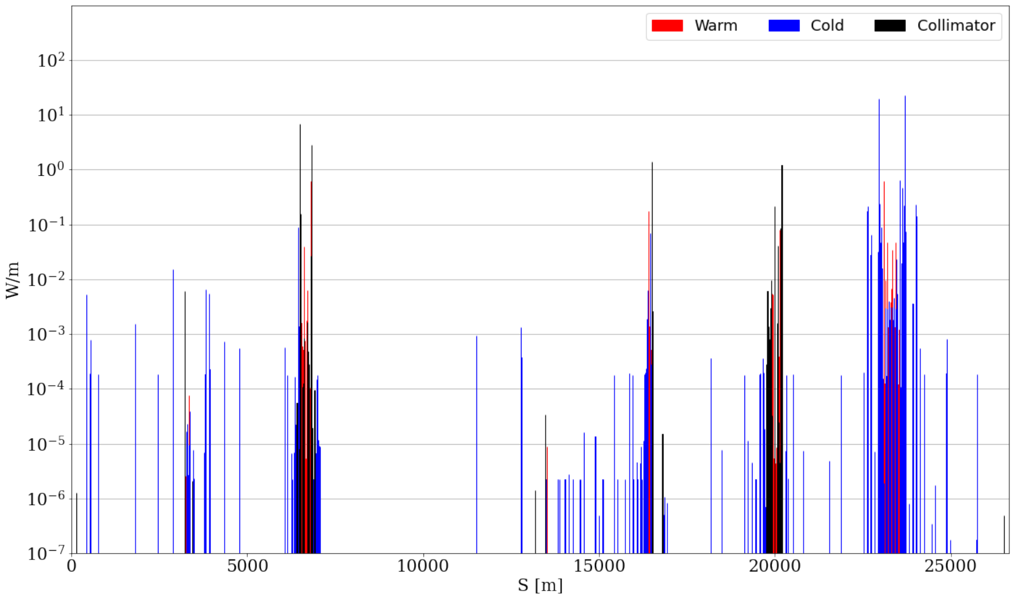

(d) Losses from IP8 collision debris.

Figure 4.18: SixTrack-FLUKA simulation of 2018 Pb-Pb collisional lossmaps for the four experiments.

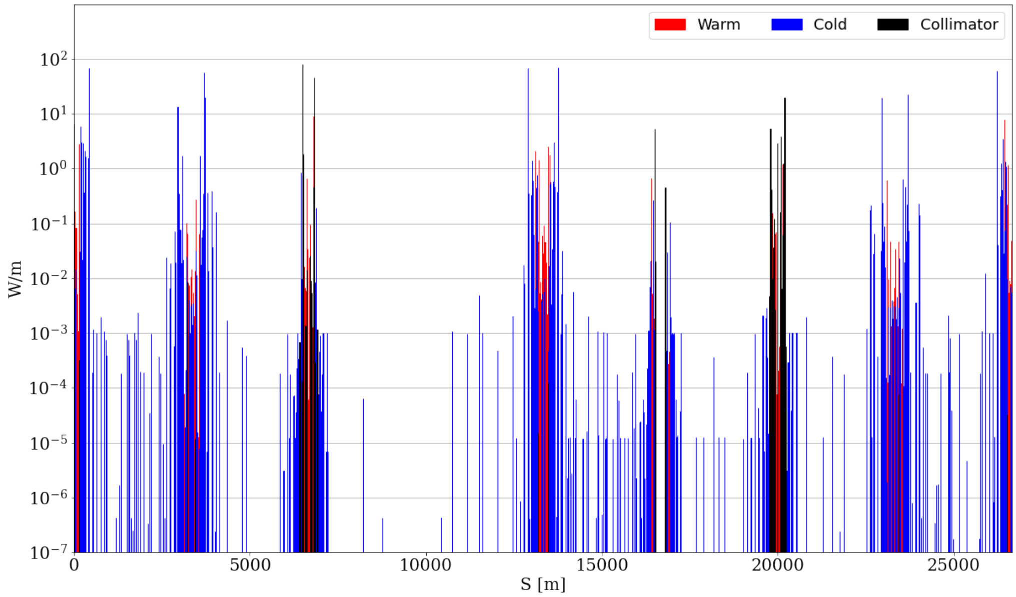

Figure 4.19: SixTrack-FLUKA simulation of 2018 Pb-Pb collisional master lossmap.

most of the heavy off-rigidity fragments such as $^{207}Pb^{+82}$. The estimated losses in W/m are compatible with the conservative quench limit of ∼9 W/m assessed at the design stage of LHC [17]. The only cold losses above that limit are indeed the BFPP peaks, which for IP1 and IP5 are not a concern since they are displaced to a position where the machine is less sensitive (see Subsec. 2.3.2). The unexpected height of the BFPP peak at the right side of IP2 is clearly a simulation artifact due to the combined effect of a step in the aperture model and the 10 cm binning of the losses—it is only one 10-cm bin that shows a high power load, and it is located exactly at a step in the aperture model that is less sharp in the real machine. At this point, losses that in reality would be a bit more spread out are intercepted at one point. With a larger bin width, the height of this loss would be lower, since the losses in neighbouring bins are much lower. The other peaks at IP2 and IP8 are anyway below the more recent estimate of quench limit, which is higher by a factor 4-5 [12].

4.4. Comparison with measured 2018 Pb-Pb lossmap

The BLM signals for the reference timestamp of fill #7477 have been extracted from LHC logged data, with a 1.3 s integration time. This allows to get a measured lossmap[1] during Pb-Pb collisions that can be compared to the simulated one for benchmarking purpose. It must be pointed out that a quantitative absolute comparison is not fully meaningful since BLMs do not directly measure the particle losses computed by the simulation but the secondary particle showers caused by the primary losses. This means that the BLM signal strongly depends on the material interposed between the location of the primary loss and the ionization chamber, where the particle showers develop. As a consequence, a BLM can detect the particle showers triggered by losses further upstream and thus measure their convolution instead of a local loss. On top of this, the imperfections of the real machine, such as magnetic field errors and beam pipe misalignments, can contribute to shift the losses of several metres. As a final remark, it is worth noticing that BLMs are not continuously placed along the 27 km of the ring, but only in the most sensitive regions. Nevertheless, a qualitative comparison of loss locations is still meaningful. Comparing the losses in different parts of the ring in relative is meaningful to a certain extent, but a factor 10 or so difference can easily appear just due to the difference in BLM response [20].

A comparison between the simulated and measured 2018 Pb-Pb collisional lossmaps is provided in Fig. 4.20. The measured lossmap (at the bottom) shows the BLM signals recorded around the ring, normalized to the highest signal and with the background noise subtracted. The background noise level was obtained by averaging the logged BLM signals over a time interval without beam in the machine, occurring shortly before the first injections in the studied fill. The same number of orders of magnitude is shown on the y-scale for both lossmaps.

In general, the agreement is very good in spite of the error sources mentioned above and the fact that the losses span many orders of magnitude. Relative to each other, the simulated losses at the IPs agree very well with the measurements. BFPP loss peaks and IR3 losses are the highest losses in the measured lossmap as well. The losses in IR3 and IR7 are very well predicted, both in terms of height and asymmetric pattern. The most striking difference in the simulated lossmap is represented by the lack of the smaller part of losses measured in IR4. This may be due to the aperture model used in the simulations, which does not exactly reproduce IR4 geometries. Furthermore, it should be noted that the simulations only contain collisional losses, and not beam losses from other sources

[1]In a measured lossmap the losses are labeled in the same way as in a simulated one, with the addition of the label "Roman pot". Roman pots are detectors designed to detect particles that have been only slightly deflected in the collisions occurring at the IPs.

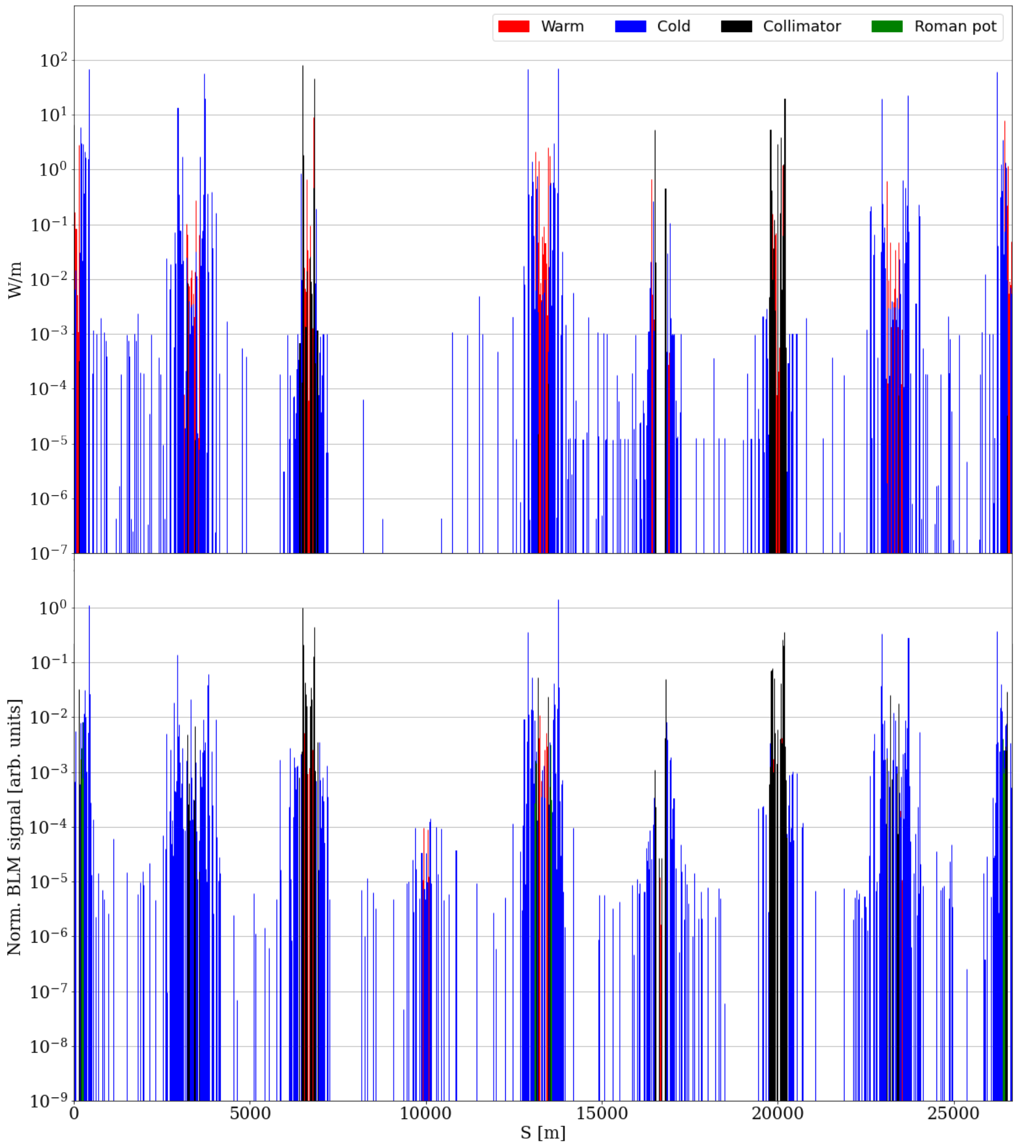

Figure 4.20: Comparison between simulated (top) and measured (bottom) 2018 Pb-Pb collisional lossmaps. The measured lossmap reports the normalized BLM signals (originally in Gy/s) for fill #7477, at the timestamp $2018-11-26\ 22:45$.

such as diffusion, non-linearities, imperfections on feedbacks and power supplies, rest-gas collisions etc., which could account for losses not present in the simulation. On the other hand, the fact that the highest loss peaks are so well reproduced by the simulations, shows that the other loss sources cannot be very important and that collisional losses are indeed dominating.

A detailed comparison of simulated and measured losses around IP1 is provided in Fig. 4.21. Comparisons of the other IPs can be found in Appendix A. The zoom in IP1 clearly shows that the simulation can predict all the main peaks of losses. As expected, the measured losses do not have the hard-edge pattern of the simulated ones, because of the intrinsic difference of the detected signal. The absence of measured signal in the warm regions around IP1 is caused by the absence of BLMs installed there. Some differences are observed also in the absence of a few single bins with much higher losses than the surrounding bins. These very localized losses, occurring at aperture transitions, cannot be detected with the BLMs that typically are spaced by at least a few meters and detect the superimposed showers of upstream losses over several metres as well.

Overall, the agreement between simulations and measurements is found to be very good, and the remaining discrepancies are not unexpected and can be explained. It is therefore concluded that the simulation model works very well in reproducing the losses in the LHC during Pb-Pb operation, and that it can be used to reliably study losses in future machine configurations.

4.5. Prediction of Pb-Pb collision losses for Run 3-4

After the validation against 2018 measured data, the simulation approach presented in Section 4.3 has proven to be reliable. This allows to use the same procedure to obtain a qualitatively good prediction of collisional losses for future runs. Pb-Pb collisional lossmap has been simulated for Run 3 and HL-LHC (Run 4) setup and design beam energy of 7 Z TeV. A similar optics will be used in the two cases, but with a lower beam energy of 6.8 Z TeV in Run 3 and 7 Z TeV for HL-LHC. The most critical case with the higher beam energy has been chosen for this study.

The Run 3 heavy-ion optics is so similar to the one used in Run 2 [24], that the same magnetic strengths can be used, however, with slightly changed values of the crossing angles (see Table 2.1). This setup features the TCLD collimators installed in IR2 during LS2 to intercept the BFPP losses [9] and increase ALICE luminosity [25]. The BFPP orbit bumps around IP8, implemented in Subsec. 4.1.3, have been added to the optics envisaged for Run 3. The BFPP bumps used in Run 2 around IP1 and IP5 have also been

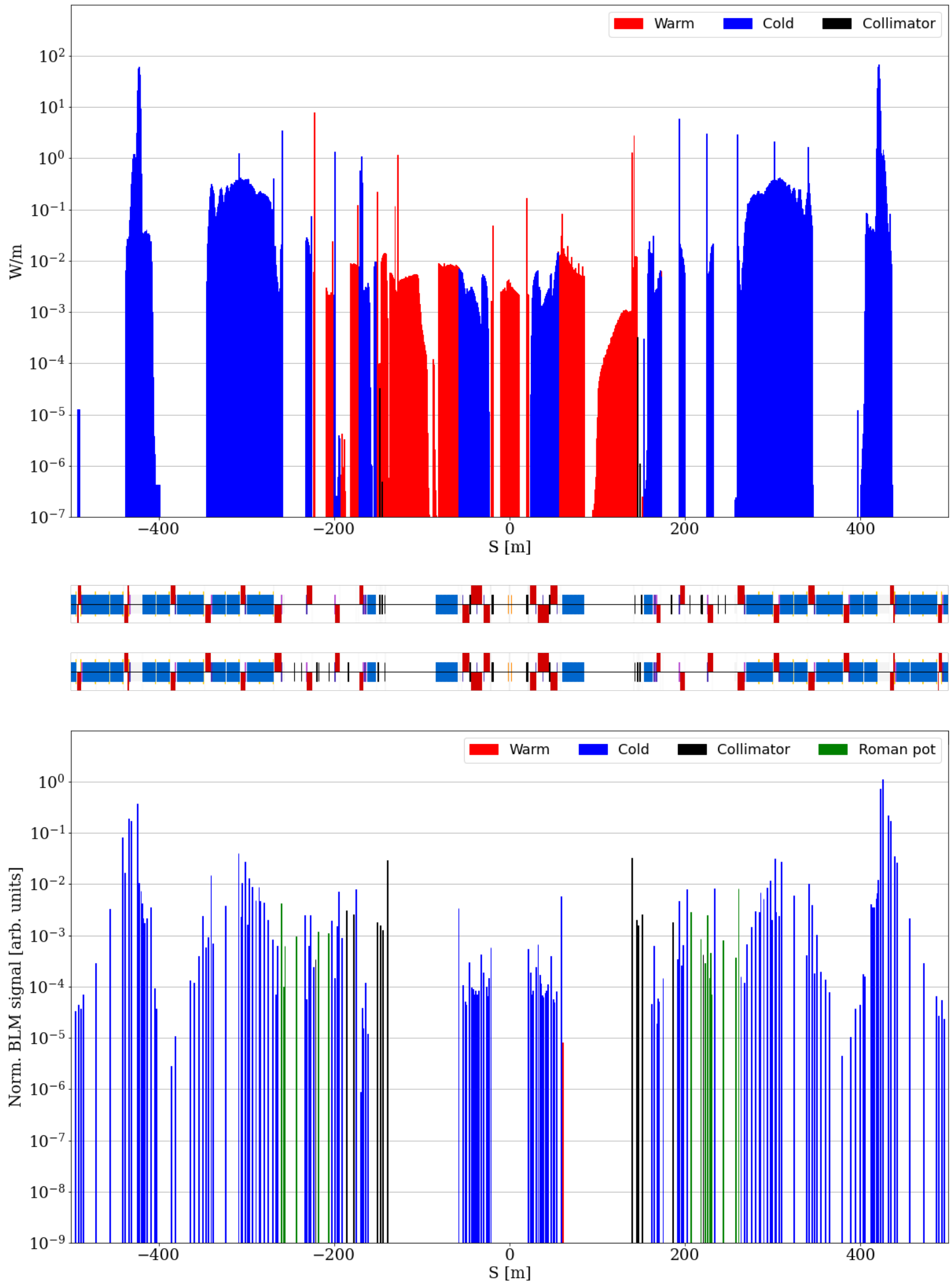

Figure 4.21: Comparison between simulated (top) and measured (bottom) 2018 Pb-Pb collisional losses around IP1. The measured lossmap reports the normalized BLM signals (originally in Gy/s). A schematic of the lattices for B1 and B2 is shown in between the lossmaps.

included, as well as the BFPP bump around IP2, however, with the amplitude increased so that the BFPP beam completely misses the first peak of the dispersion and instead hits the new TCLD. The general simulation assumptions and the used amplitudes of the BFPP bumps at the different IRs are summarized in Table 4.7.

The same statistics as for the 2018 master lossmap has been simulated, again using SixTrack-FLUKA coupling to simulate EMD and inelastic interaction losses and SixTrack with off-momentum ($\frac{82}{81} \times 7\ Z$ TeV/c) $^{208}\mathrm{Pb}^{+82}$ ions for BFPP losses. Simulations have again been carried out for all four IPs and for the two beams. The normalization of these losses has been carried out taking into account the process cross sections computed for 14 Z TeV centre-of-mass energy and the luminosities simulated for HL-LHC [24]. These values are reported in Table 4.8.

The lossmaps predicted for each IP collisional debris are shown in Fig. 4.22. The main differences with respect to those simulated for 2018 are due to the presence of the TCLD collimators around IP2. These collimators, designed to dispose of BFPP particles coming from IP2, manage to intercept a significant part of B1 off-rigidity collision products that would be otherwise cleaned out in IR3. This effect is very significant for the ion fragments created at IP2, but also for fragments created at the other IPs in B1. This is not the case for B2 collision products from the other IPs, which always pass first through IR3 and then IR2 (see the LHC ring layout in Fig. 2.2). As a result, in IP1, IP5 and IP8 lossmaps the losses on TCLD.A11R2.B1 are higher than those on TCLD.A11L2.B2 and the losses on TCP.6L3.B1 are lower than those on TCP.6R3.B2. IP2 lossmap needs a special mention, since here the losses on TCLD.A11R2.B1 and TCLD.A11L2.B2 are symmetric and replace the peaks of BFPP cold losses present in 2018 simulation. Furthermore, in IR8, the inclusion of BFPP orbit bumps in IR8 decreased the BFPP peaks by a factor ∼2.71 in B1 and ∼2.24 in B2, so that they are now below the value of 10 W/m. The master lossmap combining all the losses from each IP collisional debris is illustrated in Fig. 4.23. The

Optics	Run 3
Beam energy	7 Z TeV
Normalized emittance	1.6 μm
Momentum spread	1.06e-04
Bunch length	1.1 ns

	Right side, **B1** (mm)	Left side, **B2** (mm)
IP1	-2.6	-2.6
IP2	-4.3	-4.9
IP5	-2.5	-1.6
IP8	-5.4	-5.3

Table 4.7: Assumptions for master lossmap simulation of future runs. The table on the left reports the general assumptions, whereas the one on the right reports the amplitudes of the BFPP orbit bumps used at the different IRs.

$\mathcal{L}_{IP1/2/5}$	6.4e27 cm^{-2}s^{-1}
$\mathcal{L}_{IP8}$	1e27 cm^{-2}s^{-1}

σ_{EMD}	226 b
σ_{BFPP1}	281 b
σ_{inel}	7.8 b

Table 4.8: Luminosity values simulated for HL-LHC and process cross sections computed for 14 Z TeV centre-of-mass energy [24].

only cold losses above the conservative quench limit of ~9 W/m [17] are the BFPP peaks at IP1 and IP5, which are not a concern as mentioned above, and two localised peaks at both sides of IP2. However, they do not overcome the more recent estimate of quench limit [12] and may be simulation artifacts due to the fine binning of losses.

In conclusion, the prediction of Pb-Pb collisional losses for the future runs does not highlight any particular operational criticality. As in the past runs, the higher losses are expected to be the localised BFPP peaks, with the only difference that in IR2 they give rise to collimator losses because of the new TCLDs. These are expected to intercept most of the off-rigidity ions produced and, for this reason, the losses in IR3 are predicted to be lower than in 2018 run, despite the higher beam energies and luminosities. Losses from other sources different from collisions are expected to be less significant than the predicted ones (see Sec. 4.4) and hence this study can be considered exhaustive.

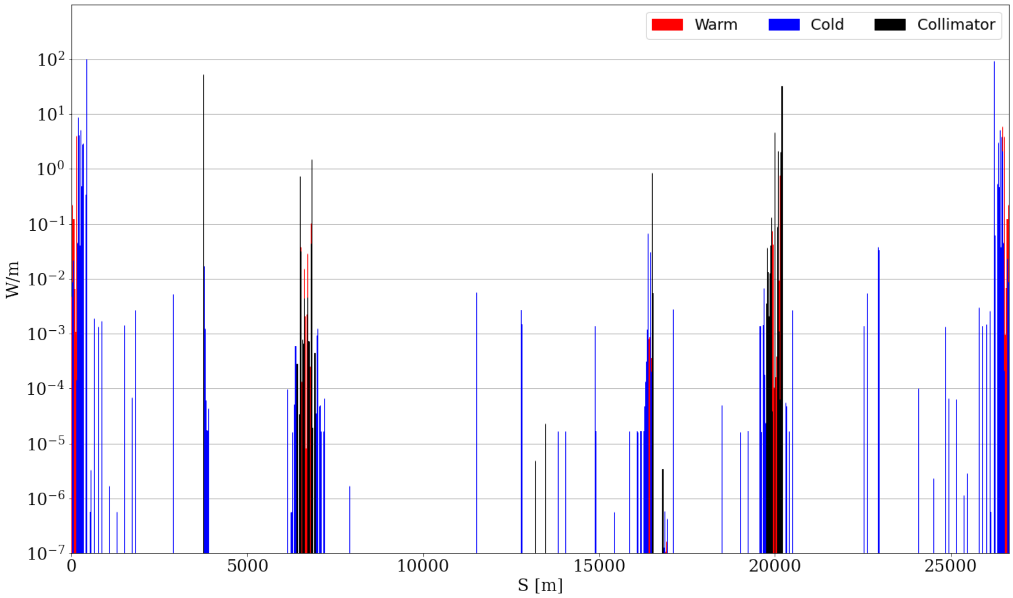

(a) Losses from IP1 collision debris.

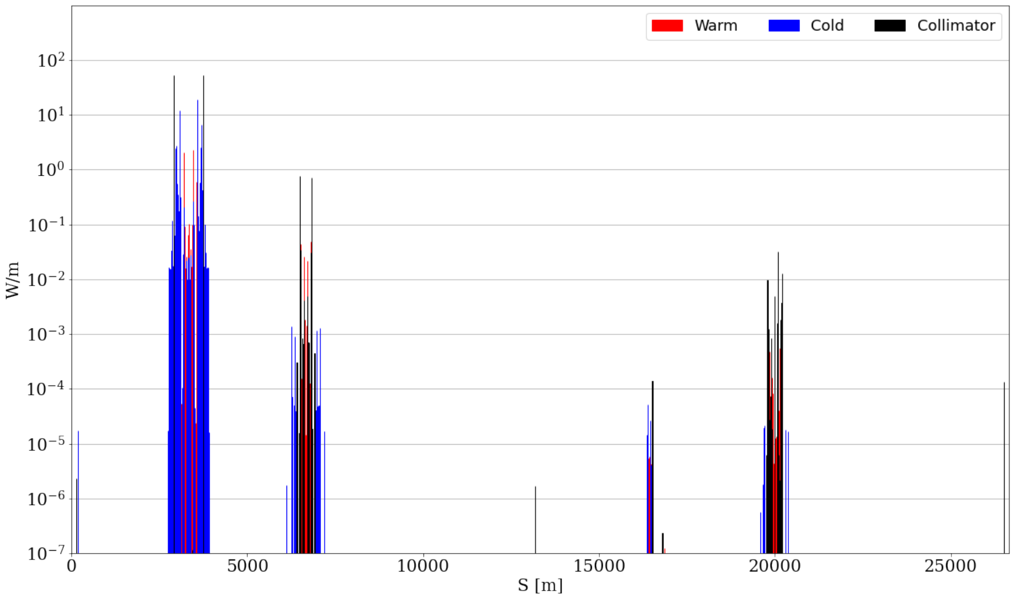

(b) Losses from IP2 collision debris.

Figure 4.22: SixTrack-FLUKA simulation of Run 3 Pb-Pb collisional lossmaps for the four experiments.

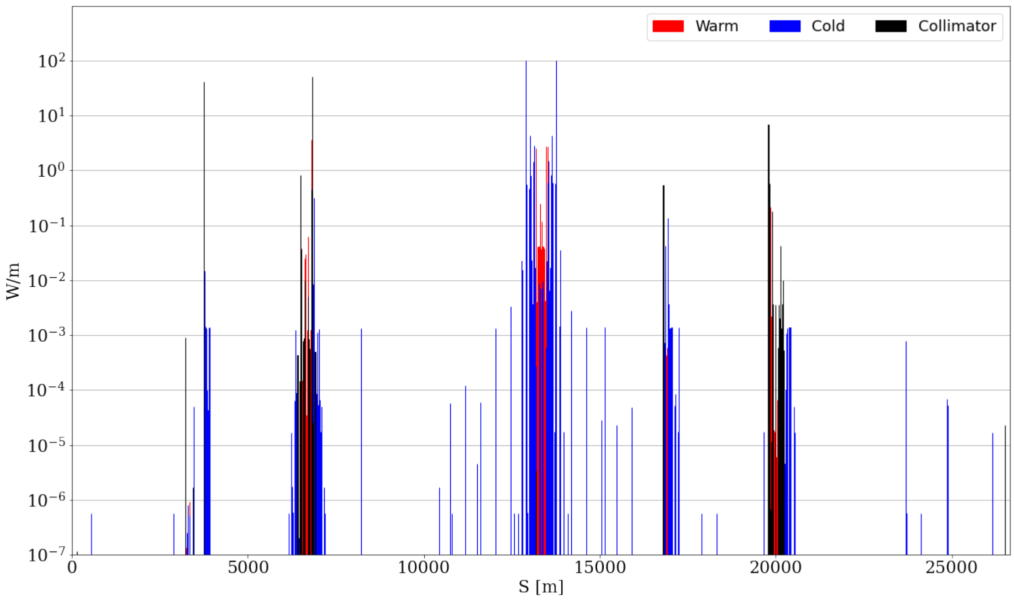

(c) Losses from IP5 collision debris.

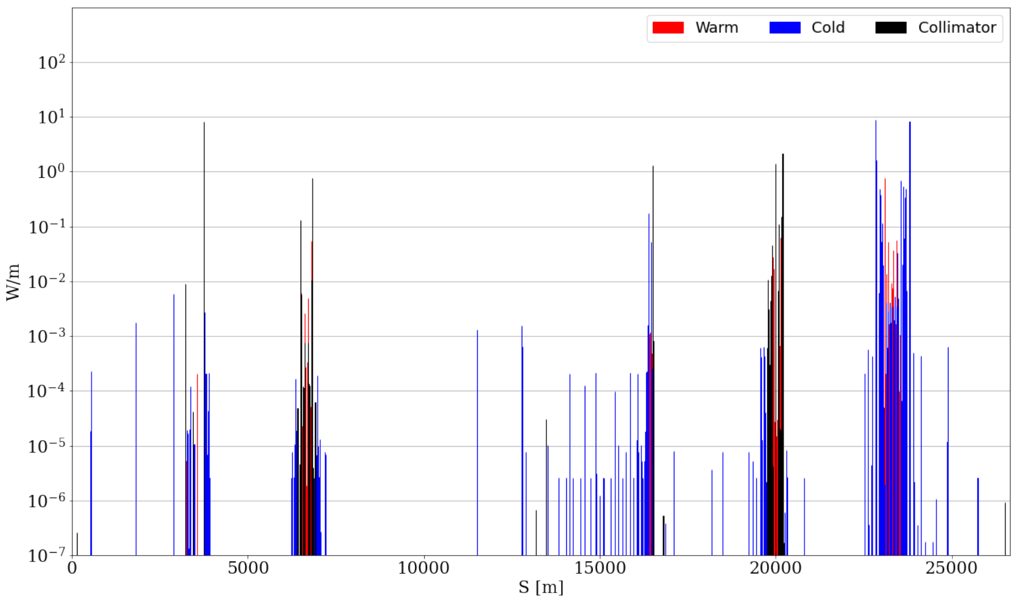

(d) Losses from IP8 collision debris.

Figure 4.22: SixTrack-FLUKA simulation of Run 3 Pb-Pb collisional lossmaps for the four experiments.

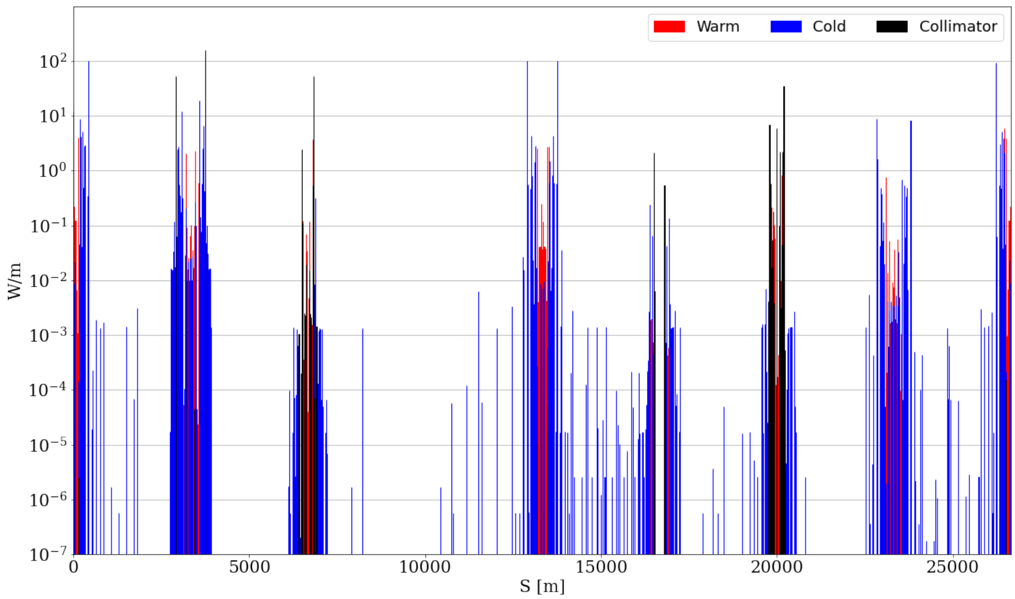

Figure 4.23: SixTrack-FLUKA simulation of Run 3 Pb-Pb collisional master lossmap.

5 | Study of collisional losses for p-Pb

The last chapter of this thesis is dedicated to the simulation of the losses from asymmetric p-Pb collisions in the LHC. The physics of p-Pb collisions is not different from that of Pb-Pb collisions, but the lower charge of the proton plays an important role. Since the density of virtual photons around the nuclei is proportional to Z^2, the electromagnetic interactions are much less probable in p-Pb than in Pb-Pb collisions. For this reason BFPP, together with elastic interactions, have been neglected in this study, as they are not expected to cause significant losses. Similarly to the Pb-Pb study, the results from simulations have been compared to LHC data of previous p-Pb runs and used to predict these losses in future runs.

An analysis of the simulated distribution of p-Pb collision products from EMD and inelastic interaction and the relative losses provoked is first presented, investigating the differences with Pb-Pb collisions. Afterwards, the results from the simulation of 2016 p-Pb collisional lossmap, containing the weighted losses caused by both the interactions, are shown and discussed. The simulated master lossmap is then compared to a corresponding measured one. Finally, following the benchmark, an estimation of p-Pb collisional losses from EMD and inelastic interactions for future runs is given.

5.1. Simulations of losses from EMD and inelastic interactions

The high generality of implementation allowed by the FLUKA collision source setup enables simulations of asymmetric collisions between p and Pb beams. Therefore, it is possible to use the SixTrack-FLUKA coupling to simulate the distribution of products from p-Pb collisions in an IP and the respective loss locations around the LHC ring. The analysis of the results from the setup of a p-Pb collision source in IP1 is carried out in the following.

The LHC optics deployed for 2016 p-Pb run at 6.5 Z TeV beam energy (see Table 2.2) has been assumed in the simulation. Normalized transverse emittances of 1.6 μm and 1.3 μm have been respectively used for the Pb beam (B1) and the p beam (B2), for both the horizontal and the vertical planes. A bunch length of 1.1 ns and a momentum spread of 1.1e-4 have been used for both beams. Since the p beam products do not include any other particles than protons that can stay within the ring acceptance, the distribution of the scattered Pb beam is more interesting and potentially more problematic for the machine. Therefore, only the products of Pb beam have been considered in the following analysis. Hence, the collision source has been setup to have a main $^{208}Pb^{+82}$ beam colliding with an opposing p beam, having the characteristics of B2. EMD and inelastic interactions have been forced separately in two case studies, each consisting of a total sample of 10^5 ions with Gaussian distribution in space before interactions. The collisions have been sampled at the center of a FLUKA geometry describing the an IP pipe, following a Gaussian distribution along the longitudinal direction, with a standard deviation of 5.83 cm accounting for the narrower distribution of collision points in space. The distributions of the products from the two types of interaction are provided and compared below. A discussion on the losses simulated by this simulation setup follows.

5.1.1. EMD

Figure 5.1 shows, through a nuclide chart, the distribution of Pb beam products from EMD in p-Pb collisions at 6.5 Z TeV beam energy. Protons and heavy nuclei around $^{208}Pb^{+82}$ are the most concentrated species, as in the distribution of products from EMD in in Pb-Pb collisions (Fig. 4.7). The major difference with Pb-Pb collisions is given by the low presence of the intermediate nuclides, for the same statistical sample of simulated interactions. This is due to the lower charge of protons in the target beam, causing less nuclear fragmentation. The lower proton charge also causes even smaller scattering angles (Fig. 5.2), which in most cases do not overcome 0.01 rad.

The distributions of energy per nucleon and magnetic rigidity have both the same characteristics of those shown for EMD in Pb-Pb collisions, hence the same discussion of Subsec. 4.2.1 applies. The reader can find these distributions in Appendix B.

5.1.2. Inelastic interactions

The nuclide chart in Fig. 5.3 shows the distribution of Pb beam products from inelastic interactions in p-Pb collisions at 6.5 Z TeV energy per beam. It looks very similar to the distribution obtained for Pb-Pb inelastic interactions, with a high concentration of light

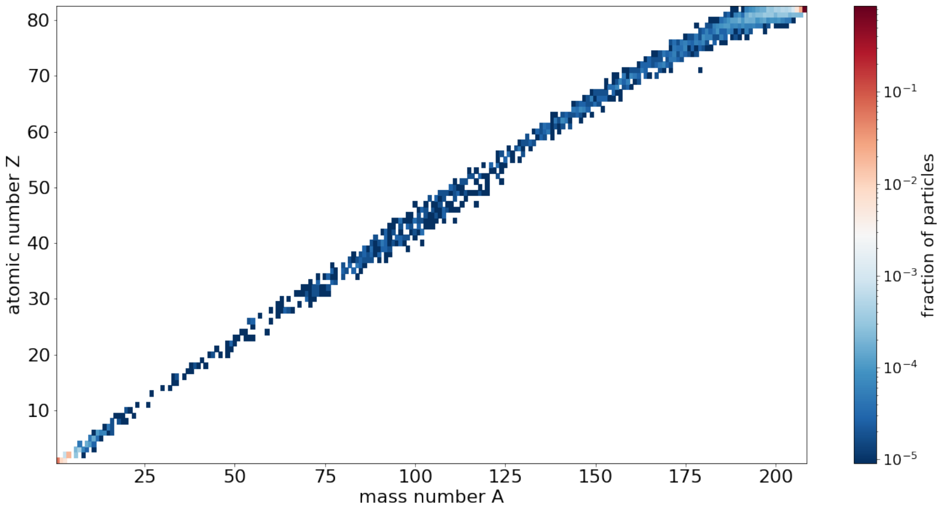

Figure 5.1: Nuclide chart of Pb beam EMD products from p-Pb collisions simulated with 6.5 Z TeV beam energy. The interactions have been simulated by FLUKA DMPJET3 event generator.

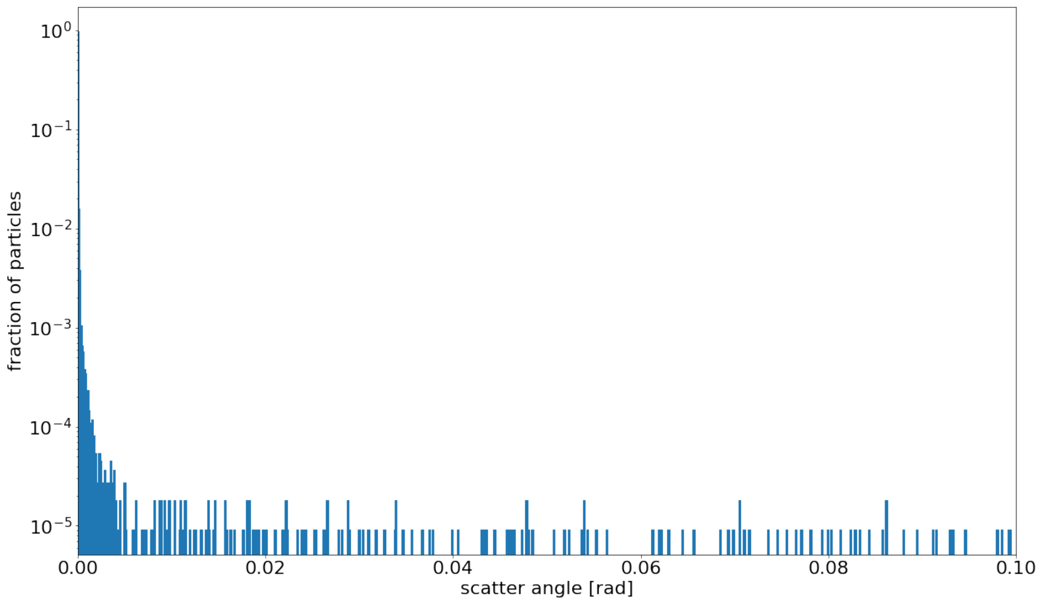

Figure 5.2: Distribution of scattering angles for Pb beam EMD products from p-Pb collisions simulated with 6.5 Z TeV beam energy. The interactions have been simulated by FLUKA DMPJET3 event generator.

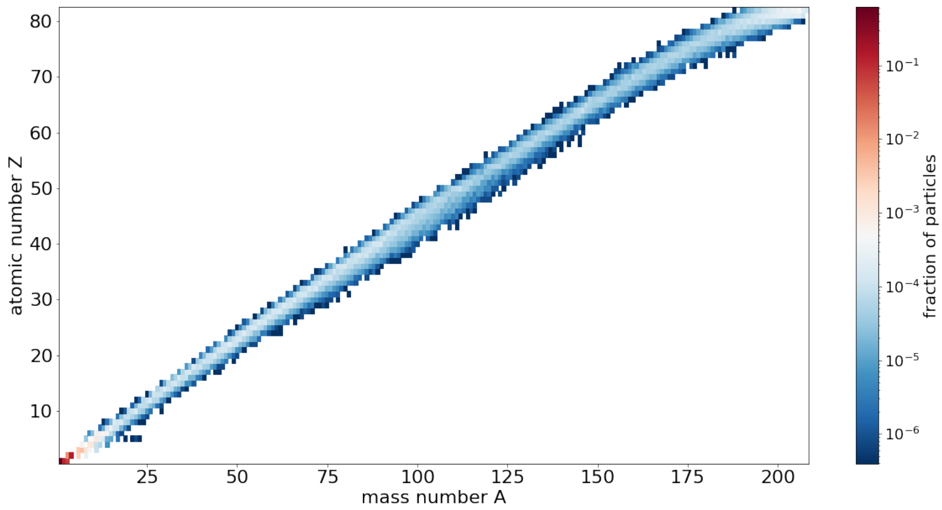

Figure 5.3: Nuclide chart of Pb beam inelastic interaction products from p-Pb collisions simulated with 6.5 Z TeV beam energy. The interactions have been simulated by FLUKA DMPJET3 event generator.

nuclei as protons, deuterium, tritium and alphas and very few heavy ions. The potential for fragmentation caused by the opposing p beam at 6.5 TeV energy is then comparable to the one of the Pb beam at 6.37 Z TeV. Instead, the lower mass of protons with respect to Pb nuclei affects the distribution of scattering angles (Fig. 5.4). These are significantly smaller than those of Pb-Pb inelastic interactions (Fig. 4.11a), being concentrated only below 0.3 rad.

Again, the products of the Pb beam from inelastic interactions with a p beam have distributions of energy per nucleon and magnetic rigidity rather close to those resulting from Pb-Pb inelastic interactions. Therefore, a discussion similar to that in Subsec. 4.2.2 is not repeated here, but these distributions are shown in Appendix B.

5.1.3. Losses

The losses around the LHC ring caused by the products from p-Pb collisions studied above have been normalized to express the power load in W/m for the peak luminosity of IP1 in 2016 6.5 Z TeV run (see Table 2.2). The interaction cross sections for p-Pb collisions reported in Ref. [53] have been taken into account in the normalization process. Specifically, for p-Pb the total cross section is dominated by inelastic interactions, as opposed to Pb-Pb where the electromagnetic interactions (BFPP and EMD) dominate (the cross sections are 35.2 mb and 2.12 b for EMD and inelastic interactions, respectively).

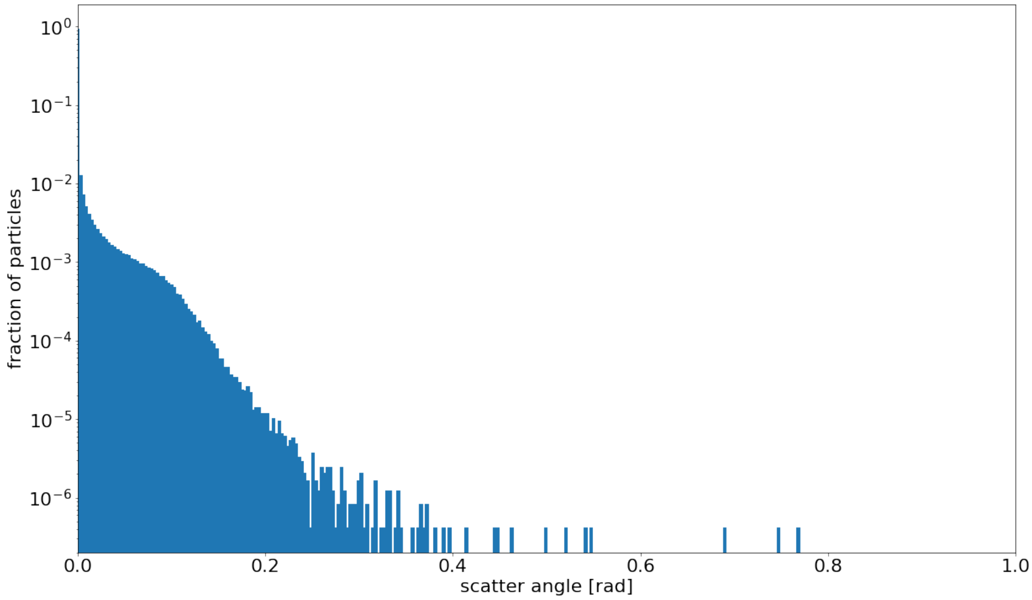

Figure 5.4: Distribution of scattering angles for Pb beam inelastic interaction products from p-Pb collisions simulated with 6.5 Z TeV beam energy. The interactions have been simulated by FLUKA DMPJET3 event generator.

The simulated losses are shown separately for the two interaction types in Fig. 5.5. As already discussed in Subsec. 4.1.1, the relative importance of the losses in the momentum cleaning region with respect those in the immediate proximity of IP1 is greater for EMD than for inelastic interactions. The more significant fragmentation and spread in scattering angles of inelastic interactions cause most of their products to be outside of the momentum acceptance of LHC and therefore they are predominantly lost locally in IR1. From an absolute point of view, losses from inelastic interactions are always larger by a couple of orders of magnitude then those from EMD, because of their larger cross section. This is the opposite of what happens in Pb-Pb collisions, where the electromagnetic interactions are much more significant than the hadronic ones.

The losses from the two types of interaction are added up in the lossmap shown in Fig. 5.6. From a comparison between this lossmap and the one including only the losses from inelastic interactions in Fig. 5.5b, it is evident that EMD losses give a negligible contribution due to the much lower cross section.

Since the distributions of Pb beam products from p-Pb collisions is qualitatively very close to those from Pb-Pb collisions, the analysis of which particles give rise to the several losses

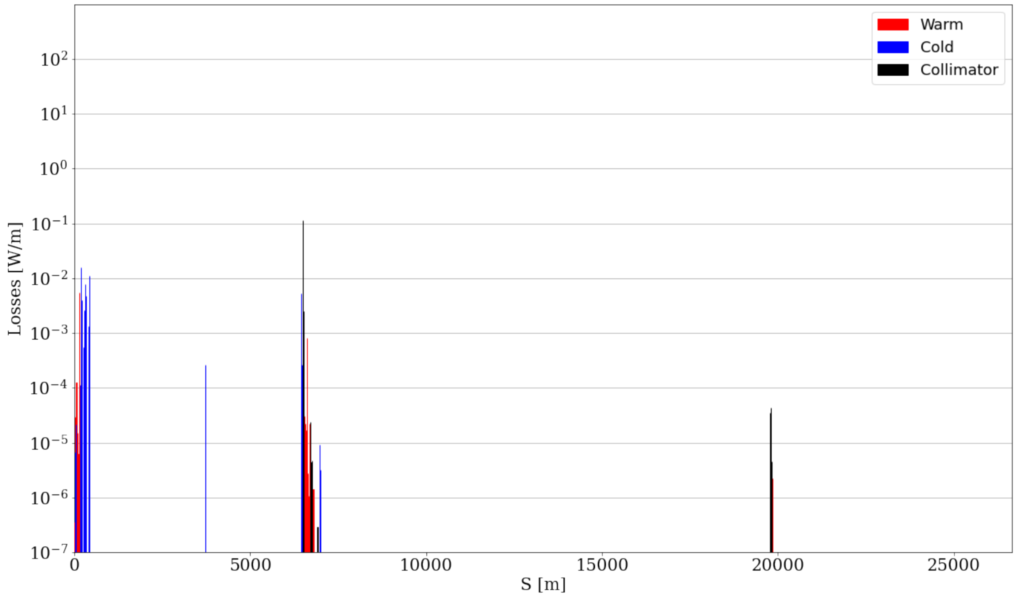

(a) Losses from EMD products.

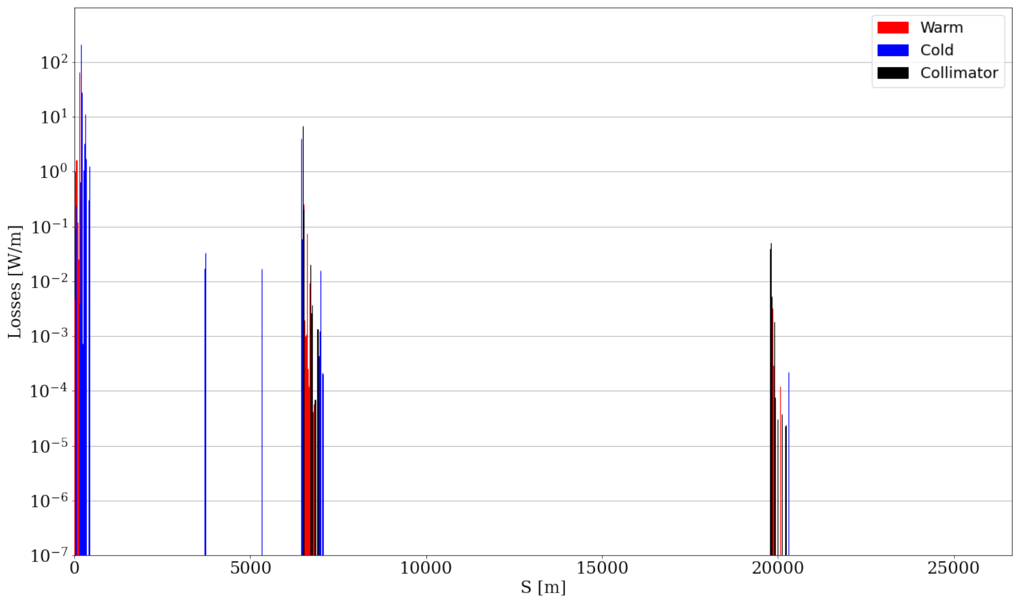

(b) Losses from inelastic interaction products.

Figure 5.5: Simulation of B1 losses from EMD (a) and inelastic interactions (b) in p-Pb collisions in IP1 at 6.5 Z TeV beam energy and $8.9\times10^{29}\mathrm{cm}^{-2}\mathrm{s}^{-1}$ luminosity. The losses have been simulated with the SixTrack-FLUKA coupling, setting up a collision source in IP1.

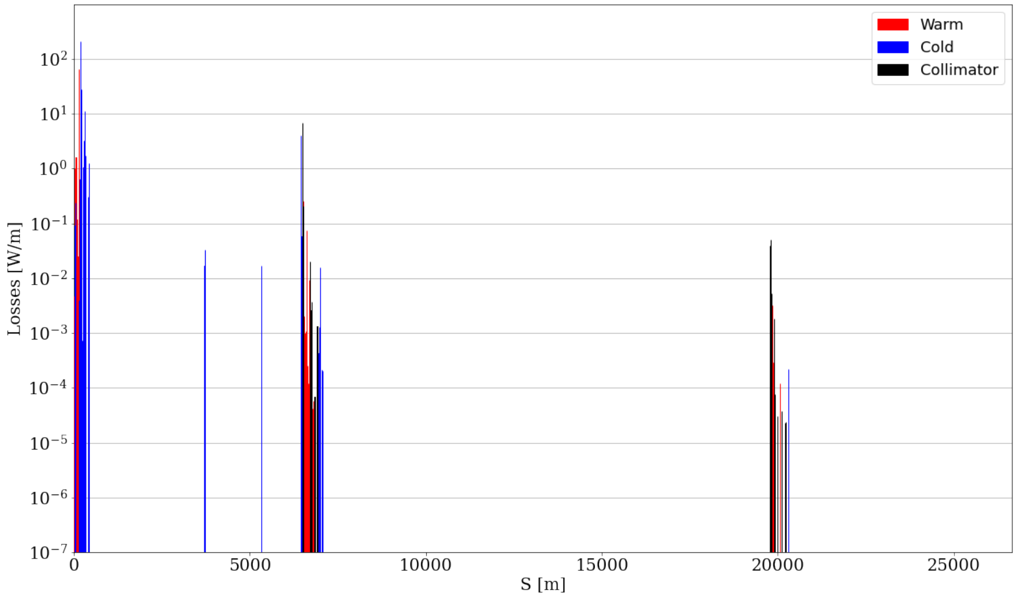

Figure 5.6: Combination of B1 losses from EMD and inelastic interactions in p-Pb collisions in IP1 at 6.5 Z TeV beam energy and $8.9\times10^{29}\text{cm}^{-2}\text{s}^{-1}$ luminosity. The losses have been simulated with the SixTrack-FLUKA coupling, setting up a collision source in IP1.

gives results analogous to those shown in Figs. 4.15, 4.16 and 4.17. The only differences are given by the lower significance of p-Pb EMD interactions: the loss peak of $^{206}\text{Pb}^{+82}$ in the DS is around two orders of magnitude lower, a lower fraction of $^{207}\text{Pb}^{+82}$ ions hits the primary collimator TCP.6L3.B1 and no $^{208}\text{Pb}^{+82}$ ions strike the primary collimators in IR7. The reader can find these plots for p-Pb collisions in Appendix B.

5.2. Simulation of 2016 master lossmap

The procedure presented in the previous section to simulate the losses from EMD and inelastic interaction in p-Pb collisions with the SixTrack-FLUKA coupling can be used to reproduce a master lossmap predicting the losses observed during experimental p-Pb operation in the LHC. The master lossmap is obtained by repeating this simulation procedure for each IP and both Pb and p beams, weighting and adding up all the results. It has been chosen to simulate the collisional lossmap for 2016 p-Pb run, taking fill #5559 with timestamp $2016-11-30\ 11:54$ as reference. The simulation assumptions are summarized in Table 5.1.

A total sample of 10^6 interactions has been simulated with SixTrack-FLUKA coupling

	^{208}**Pb**$^{+82}$ **beam**	**p beam**
Optics	Run 2 2016 (B1)	Run 2 2016 (B2)
Beam energy	6.5 Z TeV	6.5 TeV
Normalized emittance	1.6 μm	1.3 μm
Momentum spread	1.1e-04	1.1e-04
Bunch length	1.1 ns	1.1 ns

Table 5.1: Assumptions for 2016 p-Pb master lossmap simulation.

from each IP, for both EMD and inelastic interaction and both beams. It is assumed to have Pb ions in B1 and protons in B2. BFPP and elastic interactions have been neglected because of their negligible contribution to the losses. The resulting losses have been normalized following the procedure explained in Subsec. 4.1.1, taking into account the interaction cross sections and the IP luminosities at the reference timestamp. These values are reported in Table 5.2

The obtained lossmaps including the two interaction types are shown in Fig. 5.7, separately for the collisions of each IP. In each lossmap the losses are clustered around the IP where the collision source is placed and at the momentum and betatron cleaning regions (IR3 and IR7). The asymmetric collisions cause an asymmetric pattern of losses around the LHC ring. At each IP, the losses from the Pb beam (right side) are higher by a couple of orders of magnitude than those from the p beam (left side). This applies also to the losses at the collimation insertions: the losses on B1 collimators are always larger than the losses on B2 collimators, especially at IR3 where B1 collimators remove most of the heavy off-rigidity fragments from Pb beam.

These four lossmaps have been combined in the master lossmap in Fig. 5.8. It is clearly dominated by Pb beam losses, which have the highest peaks at IP1 and IP5, as expected from their higher luminosities. These cold peaks at IP1 and IP5, together with an isolated one at IP8, are higher than the conservative quench limit of ~9 W/m [17]. Nevertheless, they are few single bins with much higher losses than the surrounding bins, and hence they are most likely simulation artifacts due to aperture model transition and the binning of the losses.

$\mathcal{L}_{IP1}$	8.3562e29 cm^{-2}s^{-1}
$\mathcal{L}_{IP2}$	1.1664e29 cm^{-2}s^{-1}
$\mathcal{L}_{IP5}$	8.7280e29 cm^{-2}s^{-1}
$\mathcal{L}_{IP8}$	8.5087e28 cm^{-2}s^{-1}

σ_{EMD}	35.2 mb
σ_{inel}	2.12 b

Table 5.2: Luminosity values extracted from logged data at $2016-11-30$ $11:54$ and process cross sections for p-Pb collisions at 6.5 Z TeV beam energy [53].

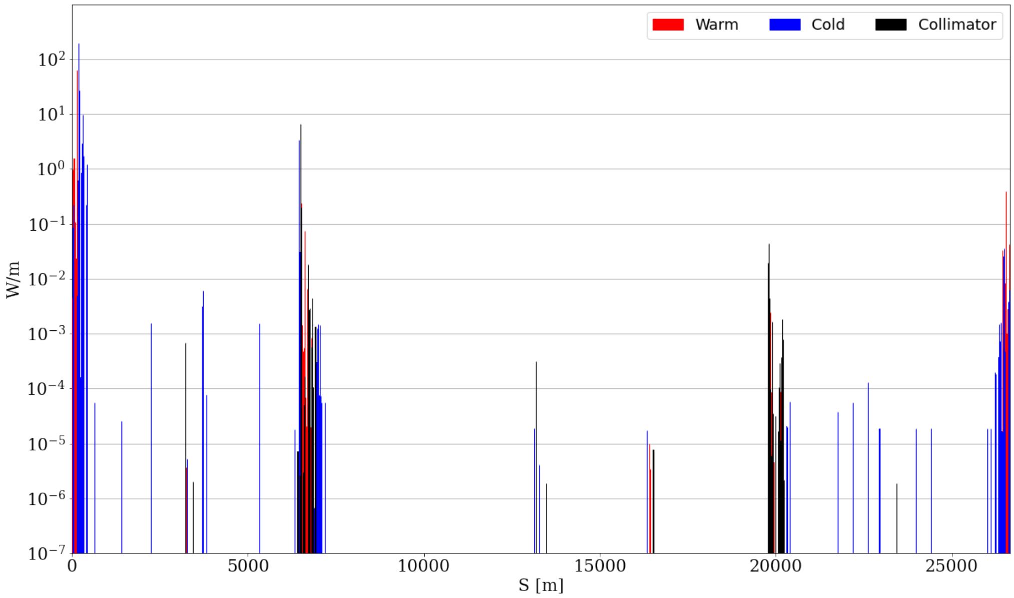

(a) Losses from IP1 collision debris.

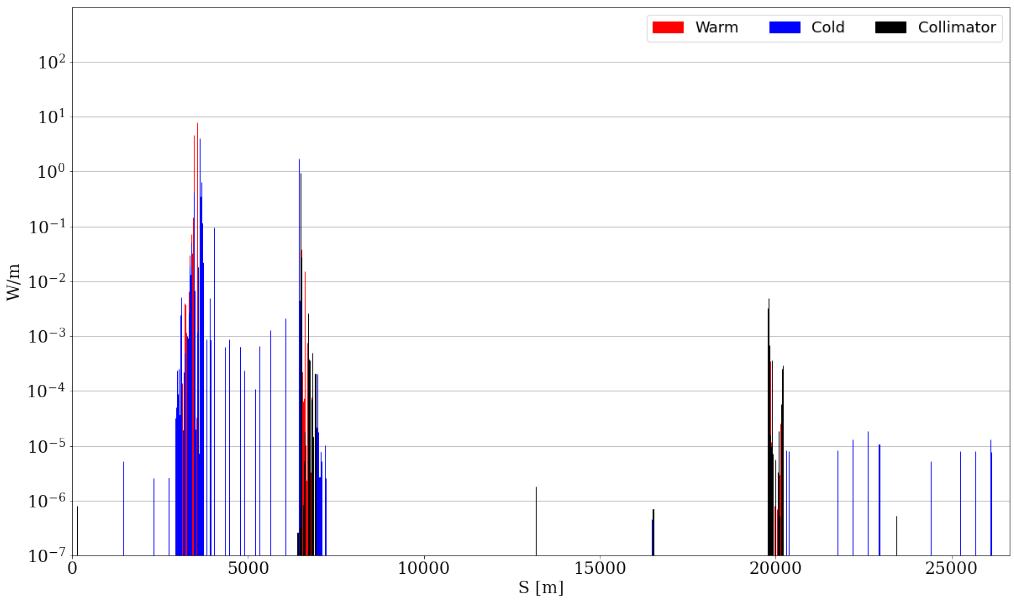

(b) Losses from IP2 collision debris.

Figure 5.7: SixTrack-FLUKA simulation of 2016 p-Pb collisional lossmaps for the four experiments.

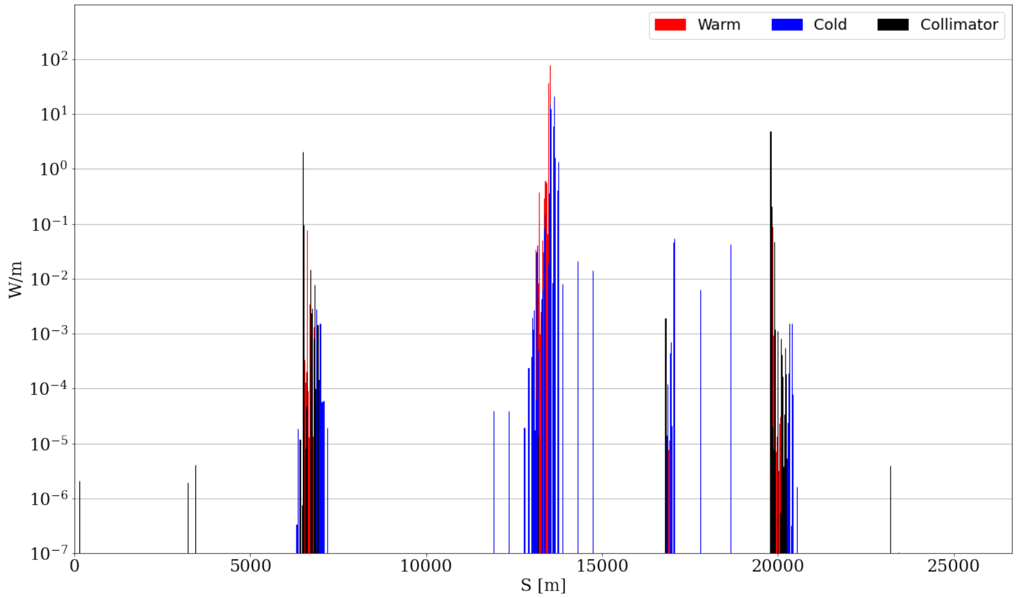

(c) Losses from IP5 collision debris.

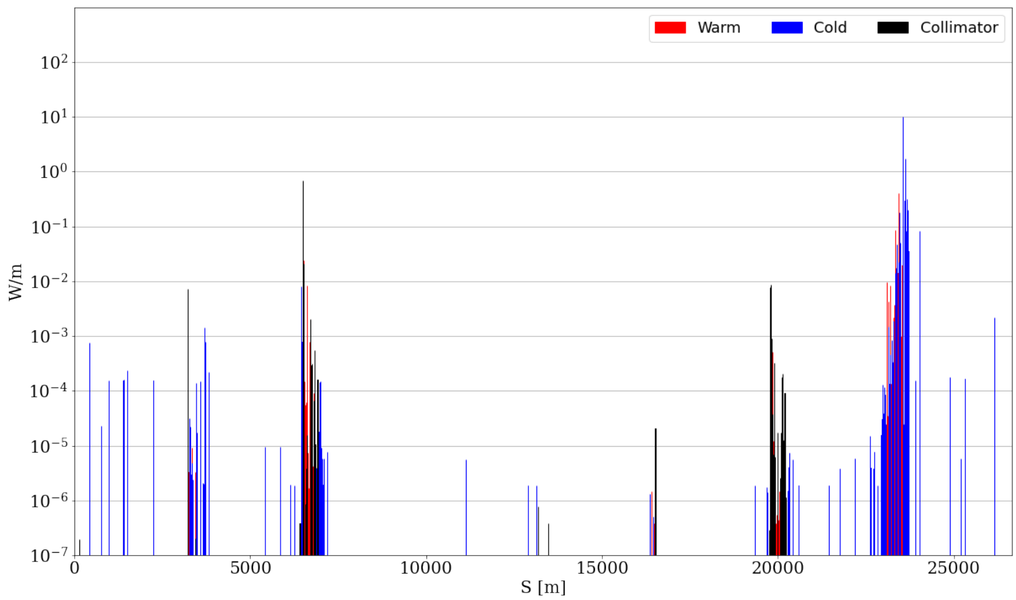

(d) Losses from IP8 collision debris.

Figure 5.7: SixTrack-FLUKA simulation of 2016 p-Pb collisional lossmaps for the four experiments.

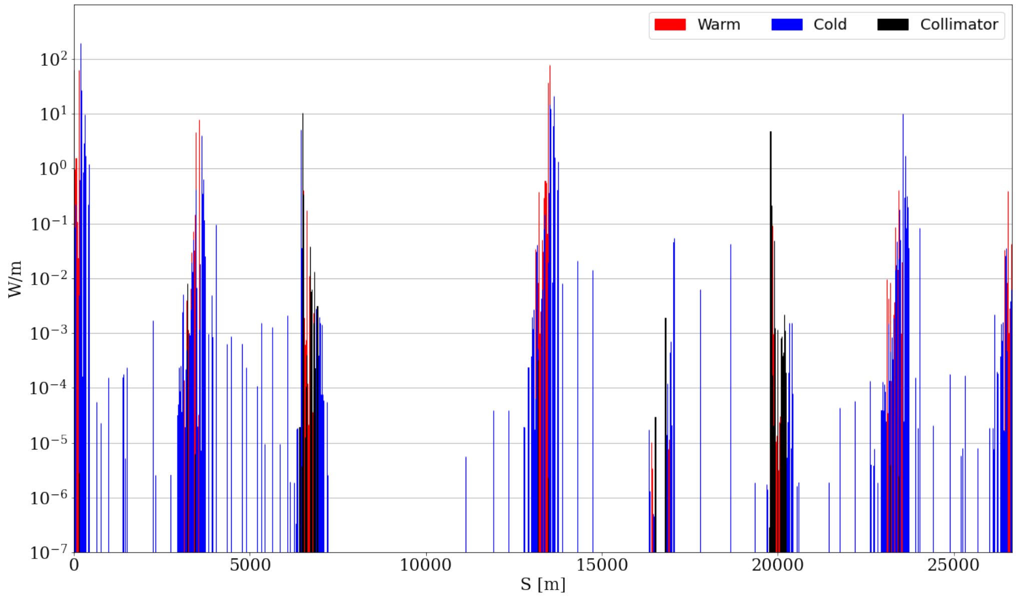

Figure 5.8: SixTrack-FLUKA simulation of 2016 p-Pb collisional master lossmap.

5.3. Comparison with measured 2016 p-Pb lossmap

In order to benchmark the simulation approach used to simulate the 2016 p-Pb master lossmap, a comparison with a corresponding measured lossmap has been carried out. The measured lossmap has been obtained by extracting the BLM signals for the reference timestamp $2016-11-30$ $11:54$ (fill #5559) from LHC logged data, with a 1.3 s integration time. The remarks made in Sec. 4.4 on the comparison between a simulated and a measured lossmap have general validity and apply in this case as well. Therefore, a perfect agreement is not expected, but a qualitative comparison is still meaningful and points out if all the main losses are predicted by the simulation.

The simulated and measured 2016 p-Pb collisional lossmaps are compared in Fig. 5.9, where the same number of orders of magnitude is shown on the y-scale for both lossmaps. The background noise, obtained by averaging over 5 s the BLM signals measured before the first injections of the beams in the reference fill, has been subtracted from the measured lossmap. Apart from the minor losses missing in IR4, the main clusters of losses are all well predicted. The height of the simulated losses at each IP are in scale to each other with the same proportion shown by the measured lossmap. Even though the asymmetry between the losses on B1 and B2 collimators is found in the measured lossmap as well,

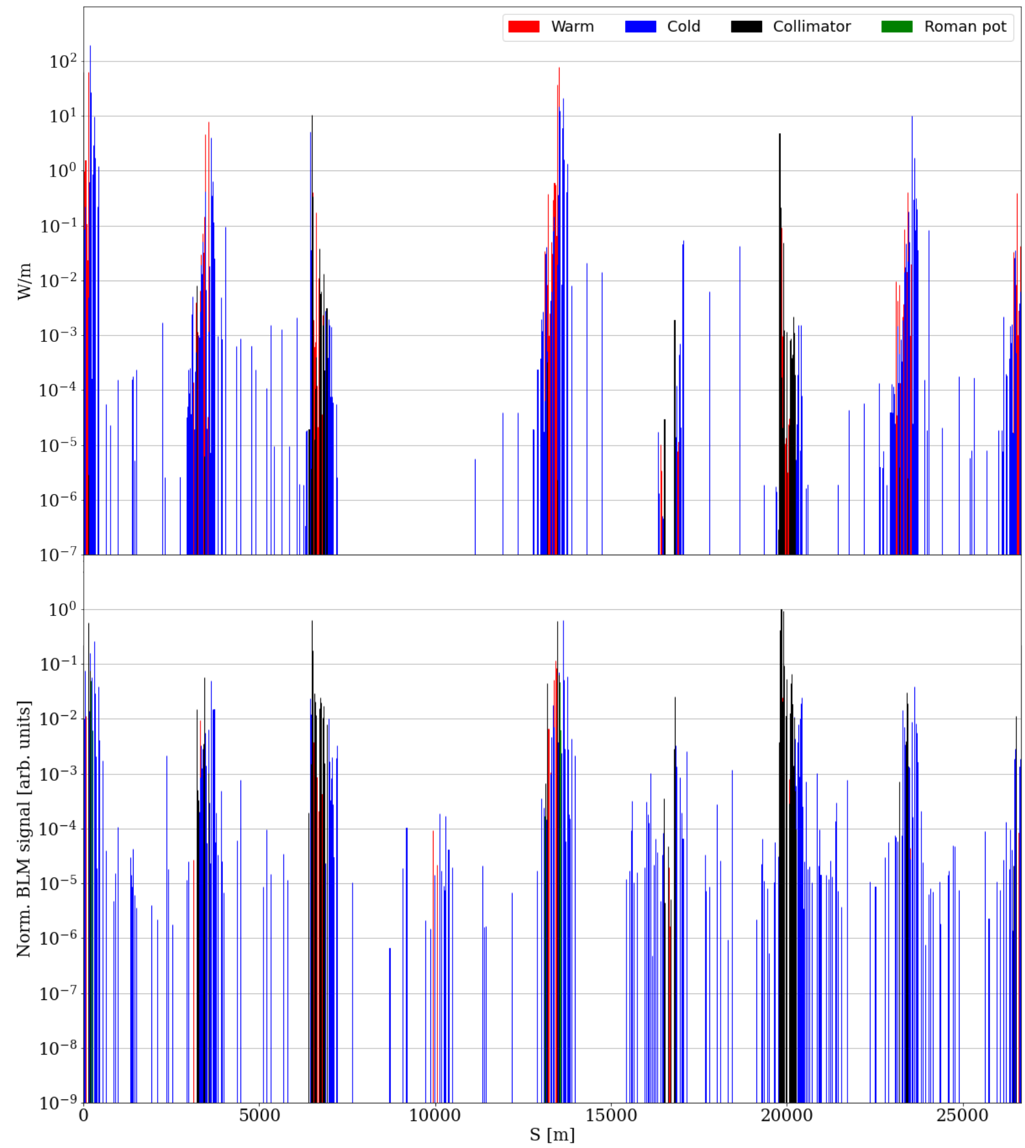

Figure 5.9: Comparison between simulated (top) and measured (bottom) 2016 p-Pb collisional lossmaps. The measured lossmap reports the normalized BLM signals (originally in Gy/s) for fill #5559, at the timestamp $2016 - 11 - 30\ 11:54$.

the measured collimator losses in IR3 and IR7 are higher by 1–2 orders of magnitude. This brings the measured losses on primary collimators to the same level as the highest losses around IP1 and IP5. Therefore, the simulated collisional losses describe well the main sources of aperture losses around the IPs, but not those on the collimators. It can be concluded that during p-Pb collisions, other mechanisms for beam losses than the collisional ones explained in Sec. 1.4, and which are not included in the simulation, dominate over the collisions to give collimator losses.

A detailed comparison of the zoom on losses around IP1 is shown in Fig. 5.10. Comparisons for the other IPs can be found in Appendix C. The asymmetry in the loss pattern between the left and the right side of the IPs is very well reproduced. It can be noticed from a closer view what has been observed above. While the main peaks of aperture losses are present in the simulation within a reasonable deviation, the losses on TCT collimators seem to be totally underestimated. However, it should be noted that the TCTs are placed on the incoming beam and they are therefore not even included in the tracking of the outgoing beam. The measured BLM signal at the TCTs could be also due to the showers of nearby losses on the outgoing beam, and not due to losses on the collimator itself. The remainder of the discrepancies is expected since it is mainly due to the spacing of BLMs and the fundamental difference of the signal they detect. For instance, most of the predicted warm losses are not present in the measurement because there are no BLMs installed at those locations.

In conclusion, the overall agreement between the simulated and the measured lossmap is very good, with the only exception of the losses at the momentum and betatron cleaning regions being underestimated, especially for the proton beam. The simulation model proved reliable in reproducing the losses in the LHC during 2016 p-Pb operation, and therefore it can be used to study losses in future machine configurations, bearing in mind that in real operation higher losses at cleaning regions IR3 and IR7 are expected.

5.4. Prediction of p-Pb collision losses for Run 3-4

The SixTrack-FLUKA coupling simulation approach, discussed in the previous sections, proved valid in reproducing losses in LHC during p-Pb collisions after the benchmark with 2016 data. For this reason, it has been used to predict the losses arising during p-Pb collisions in future LHC configurations. A p-Pb master lossmap has been simulated for Run 3 and HL-LHC setup and design beam energy of 7 Z TeV. The optics envisaged for Run 3 p-Pb operation is the same as Run 3 Pb-Pb operation, hence featuring the same magnetic strengths as Run 2 but with slightly different crossing angles (see Table 2.2).

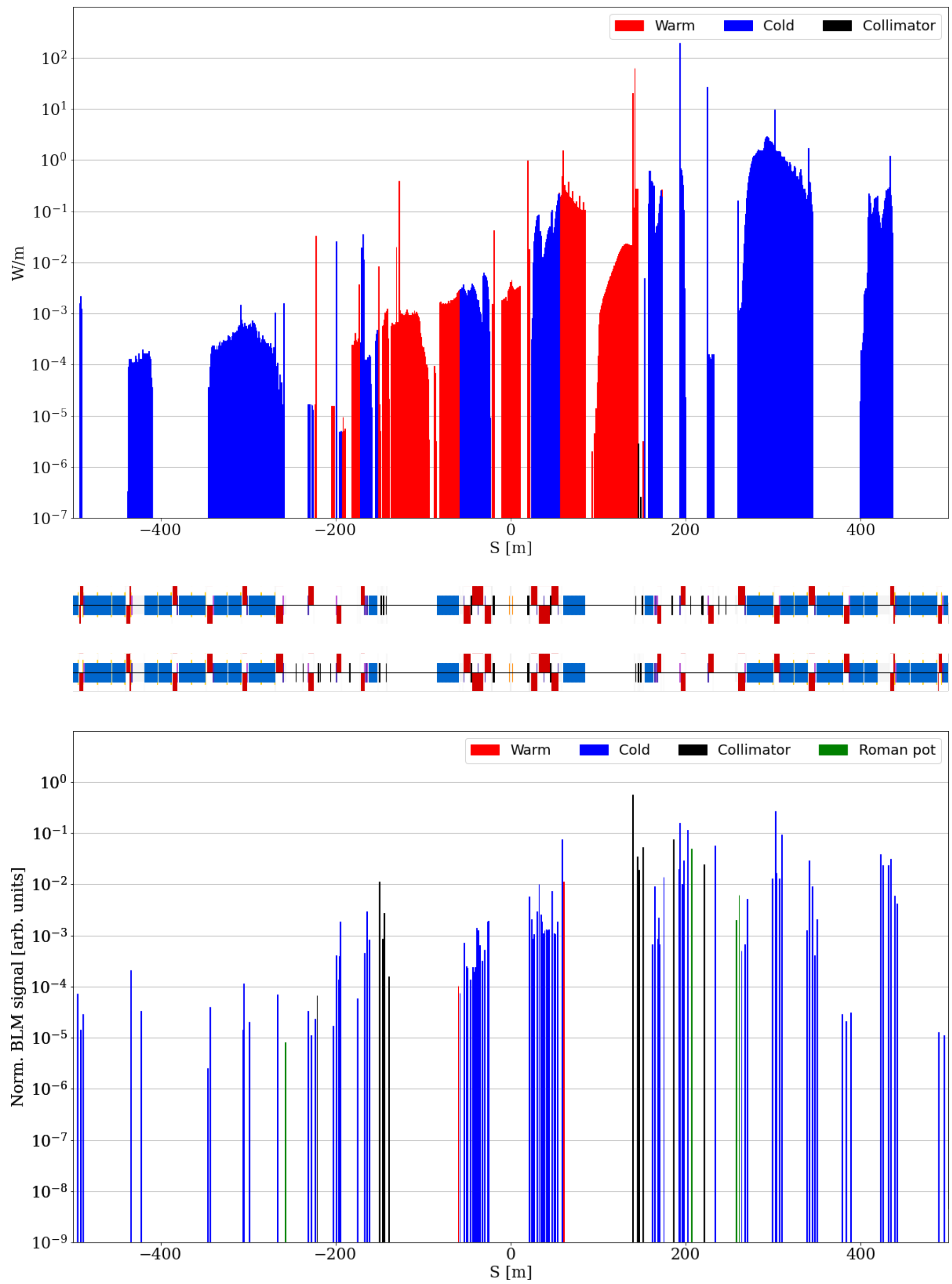

Figure 5.10: Comparison between simulated (top) and measured (bottom) 2016 p-Pb collisional losses around IP1. The measured lossmap reports the normalized BLM signals (originally in Gy/s). A schematic of the lattices for B1 and B2 is shown in between the lossmaps.

However, no BFPP orbit bumps are included in p-Pb Run 3 optics, since BFPP does not constitute a performance limiting factor, given the lower cross section of electromagnetic interactions in p-Pb collisions. For the same reason, the TCLD collimators in IR2 have been completely retracted in the simulation setup. The general assumptions of the simulations are summarized in Table 5.3.

	$^{208}\mathbf{Pb}^{+82}$ **beam**	**p beam**
Optics	Run 3 (B1)	Run 3 (B2)
Beam energy	7 Z TeV	7 TeV
Normalized emittance	1.6 μm	2.5 μm
Momentum spread	1.06e-04	1.1e-04
Bunch length	1.1 ns	1.1 ns

Table 5.3: Assumptions for Run 3 p-Pb master lossmap simulation.

The SixTrack-FLUKA coupling has been used to simulate EMD and inelastic interactions for a total sample of 10^6 particles per IP, beam and interaction type. The losses obtained have been weighted and added up, taking into account for normalization the luminosities foreseen for p-Pb future runs [24] and the p-Pb interaction cross sections computed for 7 Z TeV energy per beam [24]. These values are reported in Table 5.4.

The lossmaps obtained by simulating the collisional debris at the different IPs are shown separately in Fig. 5.11. As expected from the very similar machine configuration, the predicted lossmaps for future runs do not show any major difference with respect to those simulated for 2016 Run 2 configuration (Sec. 5.2). These four lossmaps have been combined in the master lossmap for Run 3 p-Pb operation (Fig. 5.12). Most of the simulated Run 3 losses are higher by a factor of few, given the increased beam energies and luminosities taken into account in the simulation. This is especially true for the losses around IR2, larger by an order of magnitude, since ALICE luminosity is the one that has been relatively increased the most. Both IR1, IR2, IR5 and IR8 present few cold loss peaks above the quench limit. They are most likely simulation artifacts, but a full energy deposition study is needed as future work to assess whether they could be dangerous or not.

$\mathcal{L}_{IP1/5}$	16e29 cm^{-2}s^{-1}
$\mathcal{L}_{IP2}$	5e29 cm^{-2}s^{-1}
$\mathcal{L}_{IP8}$	2e29 cm^{-2}s^{-1}

σ_{EMD}	35.5 mb
σ_{inel}	2.13 b

Table 5.4: Levelled and simulated luminosities for HL-LHC p-Pb operation and process cross sections computed for p-Pb collisions with 7 Z TeV energy per beam [24].

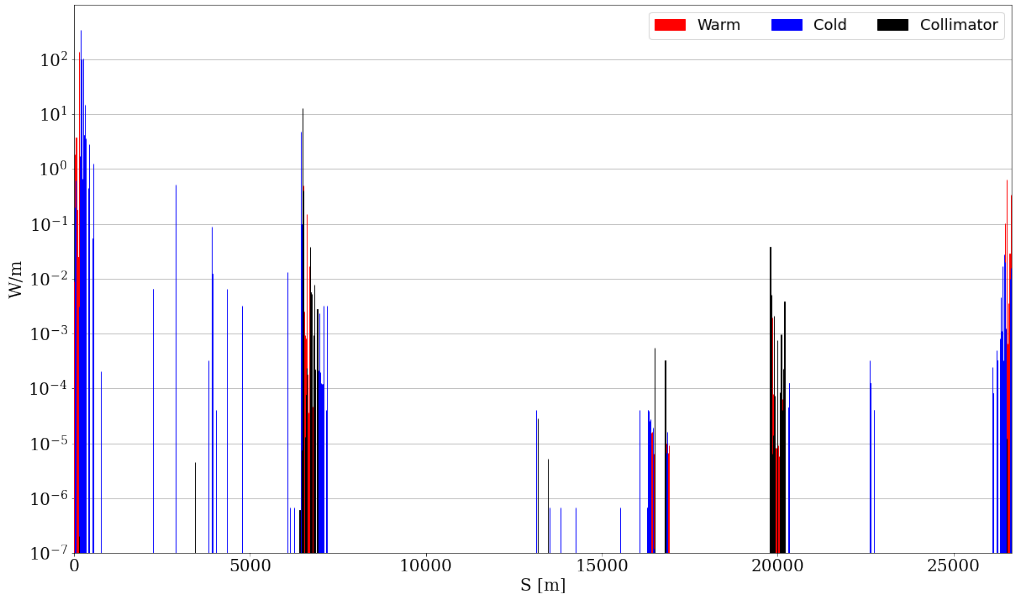

(a) Losses from IP1 collision debris.

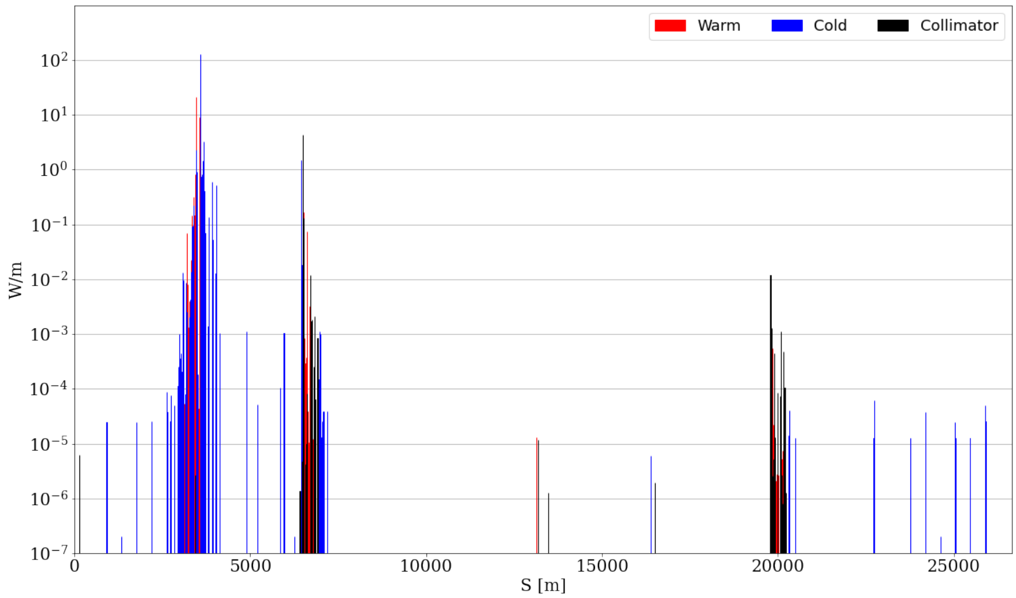

(b) Losses from IP2 collision debris.

Figure 5.11: SixTrack-FLUKA simulation of Run 3 p-Pb collisional lossmaps for the four experiments.

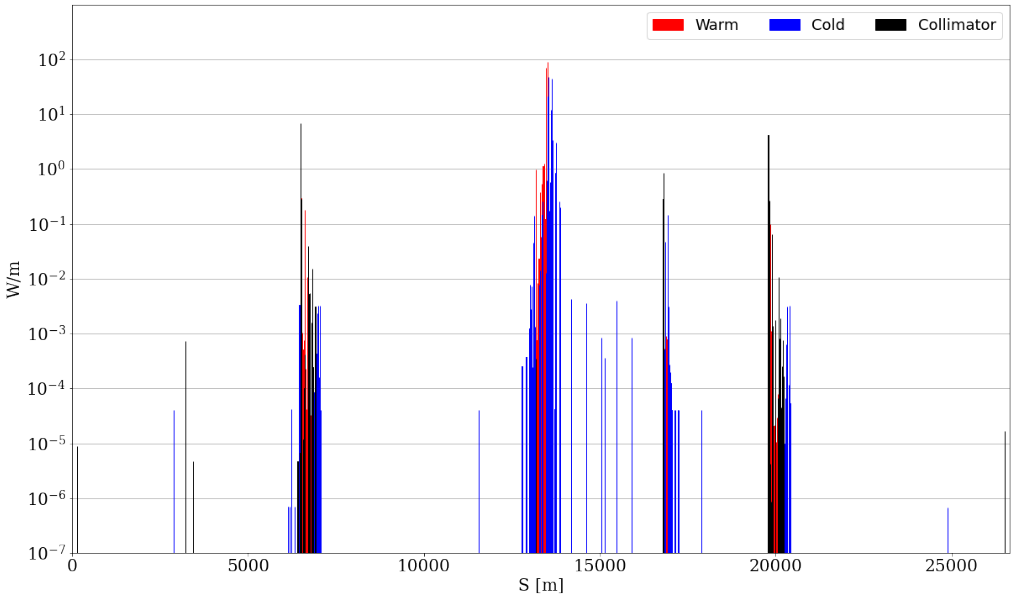

(c) Losses from IP5 collision debris.

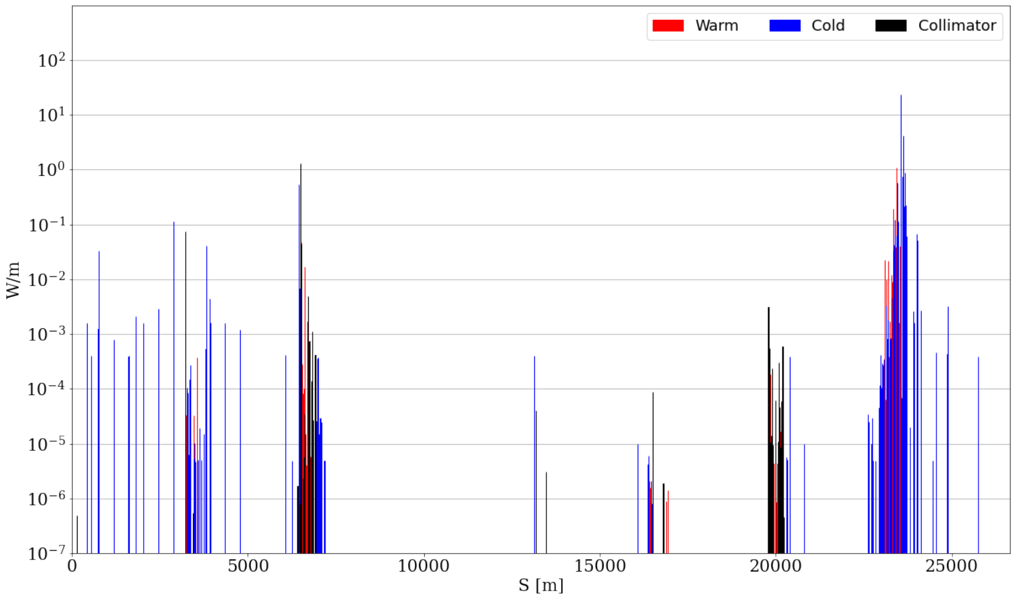

(d) Losses from IP8 collision debris.

Figure 5.11: SixTrack-FLUKA simulation of Run 3 p-Pb collisional lossmaps for the four experiments.

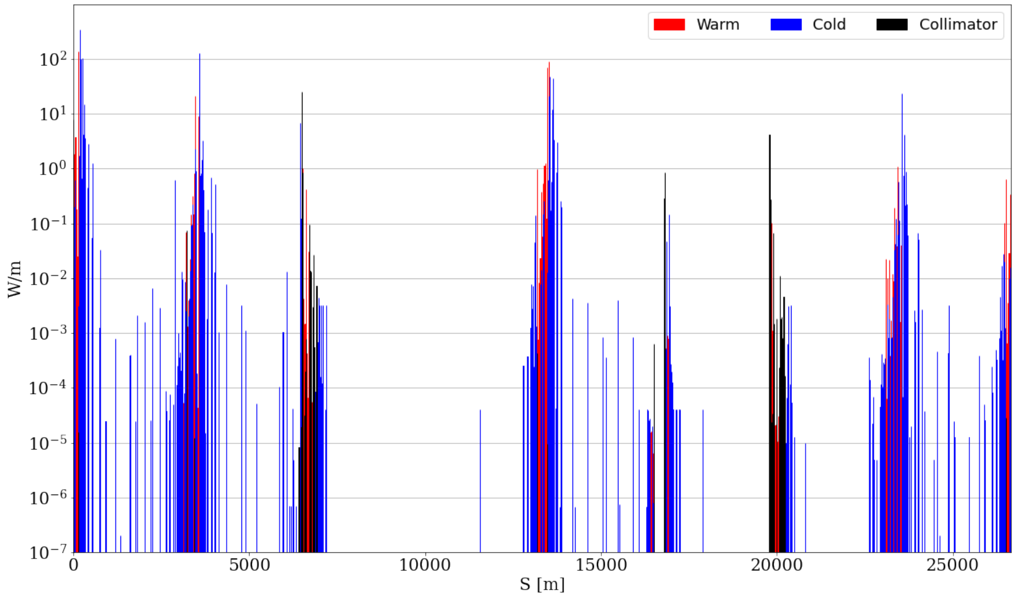

Figure 5.12: SixTrack-FLUKA simulation of Run 3 p-Pb collisional master lossmap.

It can be concluded that no particular challenges will arise in future p-Pb runs, from the point of view of beam losses. The expected loss pattern is pretty close to that measured in 2016 p-Pb run, with losses higher by a factor determined by the increased beam energies and IP luminosities. Detailed energy deposition studies at the locations of the loss peaks overcoming the quench limit are needed to verify the safety of operation. The simulated master lossmap for Run 3 gives an estimation in W/m of the losses expected during p-Pb collisions, but it must be considered that the losses at collimation regions are possibly underestimated by one and two orders of magnitude for Pb and p beam, respectively. Therefore, a dedicated study of the collimation losses due to beam halo cleaning for Run 3 p-Pb operation should be carried out to have a better evaluation.

Conclusions

The Large Hadron Collider (LHC) at CERN is the largest and highest-energy particle accelerator ever built. Inside its 27 km long ring two counter-rotating beams of protons or ions are accelerated up to 7 Z TeV and brought into collision in the four experiments ATLAS, ALICE, CMS and LHCb. For about one month per operational year, the LHC is typically operated with fully-stripped lead ions ($^{208}Pb^{+82}$), which are made to collide between themselves (Pb-Pb) or with protons (p-Pb). Four Pb-Pb runs have been executed in 2010, 2011, 2015, and 2018, and two p-Pb runs in 2013 and 2016. The LHC heavy-ion programme is foreseen to continue during Run 3 and 4 with Pb-Pb and p-Pb operation.

Apart from the desired hadronic interactions, ultraperipheral electromagnetic interactions are a very frequent phenomenon in heavy-ion collisions and they are responsible of two main effects that introduce luminosity limitations: bound-free pair production (BFPP) and electromagnetic dissociation (EMD). In BFPP an electron is created in a bound state at one of the ions, whereas in EMD an excited nucleus decays emitting one or more nucleons. As a result, secondary beams with a slightly modified charge-to-mass ratio emerge in both directions from the collision points, at small angles to the main beam. They follow dispersive trajectories, and some eventually hit the aperture of the machine, where the induced heating risks triggering beam dumps or magnet quenches. This puts an upper limit on the luminosity. Given the importance of these processes, this work aims both at studying alleviations for the most critical ones, as well as setting up detailed and reliable simulation models that can be used to study these beam losses in future operation. In this context, a full study of the main losses arising around the LHC ring during Pb-Pb and p-Pb collisions has been carried out.

First of all, a specific study on the alleviation of losses caused by BFPP in Pb-Pb collisions at the LHCb experiment has been conducted for the first time. BFPP losses were studied and successfully mitigated for all the other LHC experiments in the past, but not for LHCb. Because of a recent request to increase the LHCb luminosity, the need arose to find an alleviation strategy for this experiment. The loss patterns caused by BFPP particles have been simulated with SixTrack, assuming the LHC setup of 2018 Pb-Pb run, for both B1 and B2. The BFPP beams hit the superconducting dipoles MB.B10R8.B1 and

MB.B10L8.B2, respectively at 386 m and 365 m downstream of the experiment, with an uncertainty lower than 1 m. This prediction has been confirmed by the measured signals of the beam loss monitors (BLMs), extracted for a typical fill in the 2018 Pb-Pb run. The highest measured loss signal has been found slightly downstream of the simulated location ($\sim$7 m for B1 and $\sim$5 m for B2). This small discrepancy can be fully explained by the fact that the BLMs detect losses on the outside of the magnets downstream of the actual impact position, the incomplete spatial coverage of the BLMs, as well as possible imperfections in the aperture and orbit.

By checking the BFPP beam trajectories from IP8 with MAD-X, it has been observed that the installation of new TCLD collimators is required for the full alleviation of BFPP losses. Since this is not possible in the short term, a partial mitigation by means of an orbit bump has been investigated. For both B1 and B2, an horizontal orbit bump has been implemented with MAD-X to make the BFPP beam miss the impact location at the first peak of the dispersion in cell 10 and instead continue to the second dispersion peak in cell 12. The new loss patterns have been simulated with SixTrack including the implemented orbit bumps in the input. These are localised at the superconducting dipoles MB.C12R8.B1 and MB.C12L8.B2, respectively at 491 m and 469 m from IP8. At these locations the β-function is larger, and hence the transverse size of the BFPP beam as well as the spot size of the losses are larger, meaning that the power deposition is more spread out. In addition, a risk of symmetric quenches, present in cell 10 and not cell 12, leads to higher beam abort thresholds in cell 12, adding even more margin. As a result, with proposed orbit bumps in place, the levelled luminosity of LHCb can be safely increased by a factor 2–3 in future runs, which would be very important for LHCb.

In addition to the dedicated study of BFPP losses at LHCb, a new simulation approach to simulate the losses arising around the LHC ring during Pb-Pb and p-Pb collisions has been proposed and benchmarked in this work. It relies on the use of the SixTrack-FLUKA coupling and on the possibility of setting up a collision source in FLUKA. The interactions occurring in beam-beam collisions at the experiments are forced by FLUKA inside a geometry describing the IP pipe. The collision products are then sent back to SixTrack for standard tracking along the LHC lattice. Repeating this procedure for each experiment, beam and interaction creating significant beam losses, and weighting and adding up the resulting losses, it is possible to reproduce a collisional master lossmap.

Such a study has been performed for both Pb-Pb and p-Pb collisions, including also a detailed study of the distribution of created collision products. For Pb-Pb, EMD dominates in terms of cross section, while in p-Pb collisions, the nuclear inelastic interactions dominate. It has been found that the light ion fragments are primarily lost close to the interaction point where they were created, whereas the heavy fragments, mainly from EMD, travel further, in some cases up to the collimation regions.

In order to prove the reliability of the proposed simulation approach, master lossmaps of 2018 Pb-Pb run and 2016 p-Pb run have been simulated and compared to the corresponding measured ones. For 2018 Pb-Pb master lossmap, losses from BFPP, EMD and inelastic interactions have been included in the simulation. EMD and inelastic interactions have been simulated with the SixTrack-FLUKA coupling, whereas BFPP losses have been added up from SixTrack simulations. Instead, BFPP losses have been neglected for 2016 p-Pb master lossmap simulation because of the much lower cross section.

In both cases the simulated lossmaps have shown a very good agreement with the experimental data, reproducing all the main clusters and peaks of losses with ratios as in the measured lossmaps. The only exception is represented by the losses at the collimation regions of 2016 p-Pb master lossmap simulation, which are underestimated. This shows that for Pb-Pb operation the collisional losses, the only simulated loss source, are the dominating contribution to the collimator losses, while for p-Pb operation other loss sources dominate. The remaining minor discrepancies can mainly be explained by the fundamental difficulty in comparing simulated losses on the aperture and the BLM signal caused by the induced particle showers, as mentioned above, and thus are not unexpected.

The simulation approach presented has proven capable of providing results with an excellent agreement with experimental data and hence it can be considered a valid tool to estimate the beam losses of future operation. In this work a prediction of Pb-Pb and p-Pb master lossmaps for Run 3-4 has been given, including in the simulation setup all the changes envisaged for the next machine configurations, as well as the proposed orbit bumps in the case of Pb-Pb simulations. Despite the increased beam energies and luminosities featured in future runs, most of the losses have been found to be below the conservative quench limit estimate at the design stage of LHC. The few cold loss peaks that exceed the estimated approximate quench limit are either the BFPP peaks in Pb-Pb prediction, which are safely displaced to an empty cryostat, or simulation artifacts due to the aperture model and the binning of the losses, that are not likely to cause a real danger of quenching. Nevertheless, to verify this, it would be useful as future work to study the highest losses with full energy deposition studies, modelling the actual power load on the superconducting coils.

Bibliography

[1] MAD-X program. `http://cern.ch/mad/` CERN, Geneva, Switzerland.

[2] Sixtrack web site. `http://sixtrack.web.cern.ch/SixTrack/`.

[3] LHCb technical proposal. *CERN/LHCC 98-4, LHCC/P4*, 1998.

[4] LHC Design Report Vol.1: The LHC Main Ring. 6 2004. doi: 10.5170/CERN-2004-003-V-1.

[5] A. Mereghetti *et al.* Sixtrack-FLUKA active coupling for the upgrade of the SPS scrapers. *Proceedings of the International Particle Accelerator Conference 2013, Shanghai, China*, page 2657, 2013.

[6] C. Ahdida et al. New Capabilities of the FLUKA Multi-Purpose Code. *Front. in Phys.*, 9:788253, 2022. doi: 10.3389/fphy.2021.788253.

[7] R. Alemany-Fernandez, E. Bravin, L. Drosdal, A. Gorzawski, V. Kain, M. Lamont, A. Macpherson, G. Papotti, M. Pojer, L. Ponce, S. Redaelli, G. Roy, M. S. Camillocci, W. Venturini, and J. Wenninger. Operation and Configuration of the LHC in Run 1. *CERN-ACC-NOTE-2013-0041*, 2014.

[8] ALICE Collaboration: F. Carminati, P. Foka, P. Giubellino, A. Morsch, G. Paic, J.-P. Revol, K. Safarik, Y. Schutz, and U. A. Wiedemann (editors). Alice: Physics performance report, volume i. *Journal of Physics G: Nuclear and Particle Physics*, 30(11):1517–1763, 2004.

[9] G. Apollinari, I. B. Alonso, O. Bruning, P. Fessia, M. Lamont, L. Rossi, and L. Tavian (editors). *High-Luminosity Large Hadron Collider (HL-LHC): Technical Design Report V. 0.1.* CERN Yellow Reports: Monographs. CERN-2017-007-M. CERN, Geneva, Switzerland, 2017. doi: http://dx.doi.org/10.23731/CYRM-2017-004. URL `https://cds.cern.ch/record/2284929`.

[10] R. W. Assmann. Preliminary Beam-based specifications for the LHC collimators. Technical Report LHC-PROJECT-NOTE-277, CERN, Geneva, Jan 2002. URL `http://cds.cern.ch/record/691766`.

[11] ATLAS Collaboration. The ATLAS experiment at the CERN Large Hadron Collider. *JINST*, 3:S08003, 2008.

[12] B. Auchmann, T. Baer, M. Bednarek, G. Bellodi, C. Bracco, R. Bruce, F. Cerutti, V. Chetvertkova, B. Dehning, P. P. Granieri, W. Hofle, E. B. Holzer, A. Lechner, E. Nebot Del Busto, A. Priebe, S. Redaelli, B. Salvachua, M. Sapinski, R. Schmidt, N. Shetty, E. Skordis, M. Solfaroli, J. Steckert, D. Valuch, A. Verweij, J. Wenninger, D. Wollmann, and M. Zerlauth. Testing beam-induced quench levels of LHC superconducting magnets. *Phys. Rev. ST Accel. Beams*, 18:061002, 2015. doi: 10.1103/PhysRevSTAB.18.061002.

[13] A. J. Baltz, M. J. Rhoades-Brown, and J. Weneser. Heavy-ion partial beam lifetimes due to coulomb induced processes. *Phys. Rev. E*, 54:4233, 1996. doi: 10.1103/PhysRevE.54.4233.

[14] J. Bardeen, L. N. Cooper, and J. R. Schrieffer. Theory of superconductivity. *Phys. Rev.*, 108:1175–1204, Dec 1957. doi: 10.1103/PhysRev.108.1175. URL `https://link.aps.org/doi/10.1103/PhysRev.108.1175`.

[15] G. Battistoni et al. Overview of the FLUKA code. *Annals Nucl. Energy*, 82:10–18, 2015. doi: 10.1016/j.anucene.2014.11.007.

[16] V. Boccone, R. Bruce, M. Brugger, M. Calviani, F. Cerutti, L. Esposito, A. Ferrari, A. Lechner, A. Mereghetti, E. Nowak, N. Shetty, E. Skordis, R. Versaci, and V. Vlachoudis. Beam-machine interaction at the cern lhc. *Nuclear Data Sheets*, 120:215 – 218, 2014. ISSN 0090-3752. doi: https://doi.org/10.1016/j.nds.2014.07.050. URL `http://www.sciencedirect.com/science/article/pii/S009037521400502X`.

[17] C. Bracco. *Commissioning Scenarios and Tests for the LHC Collimation System*. PhD thesis, EPFL Lausanne, 2008.

[18] R. Bruce, D. Bocian, S. Gilardoni, and J. M. Jowett. Beam losses from ultraperipheral nuclear collisions between Pb ions in the Large Hadron Collider and their alleviation. *Phys. Rev. ST Accel. Beams*, 12(7):071002, Jul 2009. doi: 10.1103/PhysRevSTAB.12.071002.

[19] R. Bruce, R. Assmann, V. Boccone, G. Bregliozzi, H. Burkhardt, F. Cerutti, A. Ferrari, M. Huhtinen, A. Lechner, Y. Levinsen, A. Mereghetti, N. Mokhov, I. Tropin, and V. Vlachoudis. Sources of machine-induced background in the ATLAS and CMS detectors at the CERN Large Hadron Collider. *Nucl. Instrum. Methods Phys. Res. A*, 729(0):825 – 840, 2013. doi: 10.1016/j.nima.2013.08.058.

[20] R. Bruce, R. W. Assmann, V. Boccone, C. Bracco, M. Brugger, M. Cauchi, F. Cerutti, D. Deboy, A. Ferrari, L. Lari, A. Marsili, A. Mereghetti, D. Mirarchi, E. Quaranta, S. Redaelli, G. Robert-Demolaize, A. Rossi, B. Salvachua, E. Skordis, C. Tambasco, G. Valentino, T. Weiler, V. Vlachoudis, and D. Wollmann. Simulations and measurements of beam loss patterns at the CERN Large Hadron Collider. *Phys. Rev. ST Accel. Beams*, 17:081004, Aug 2014. doi: 10.1103/PhysRevSTAB.17.081004. URL `http://link.aps.org/doi/10.1103/PhysRevSTAB.17.081004`.

[21] R. Bruce, G. Arduini, H. Bartosik, R. de Maria, M. Giovannozzi, G. Iadarola, J. Jowett, K. Li, M. Lamont, A. Lechner, E. Metral, D. Mirarchi, T. Pieloni, S. Redaelli, G. Rumolo, B. Salvant, R. Tomas, and J. Wenninger. LHC Run 2: Results and challenges. *Proceedings of the 57th ICFA Advanced Beam Dynamics Workshop on High-Intensity and High-Brightness Hadron Beams, Malmo, Sweden*, 2016. URL `http://accelconf.web.cern.ch/AccelConf/hb2016/papers/moam5p50.pdf`.

[22] R. Bruce, C. Bracco, R. D. Maria, M. Giovannozzi, A. Mereghetti, D. Mirarchi, S. Redaelli, E. Quaranta, and B. Salvachua. Reaching record-low β^* at the CERN Large Hadron Collider using a novel scheme of collimator settings and optics. *Nucl. Instrum. Methods Phys. Res. A*, 848:19 – 30, Jan 2017. doi: http://dx.doi.org/10.1016/j.nima.2016.12.039. URL `http://www.sciencedirect.com/science/article/pii/S0168900216313092`.

[23] R. Bruce, M. Huhtinen, A. Manousos, F. Cerutti, L. Esposito, R. Kwee-Hinzmann, A. Lechner, A. Mereghetti, D. Mirarchi, S. Redaelli, and B. Salvachua. Collimation-induced experimental background studies at the CERN Large Hadron Collider. *Phys. Rev. Accel. Beams*, 22:021004, Feb 2019. doi: 10.1103/PhysRevAccelBeams.22.021004. URL `https://link.aps.org/doi/10.1103/PhysRevAccelBeams.22.021004`.

[24] R. Bruce, T. Argyropoulos, H. Bartosik, R. D. Maria, N. Fuster-Martinez, M. Jebramcik, J. Jowett, N. Mounet, S. Redaelli, G. Rumolo, M. Schaumann, and H. Timko. HL-LHC operational scenario for Pb-Pb and p-Pb operation. *CERN-ACC-2020-0011*, 2020. URL `https://cds.cern.ch/record/2722753`.

[25] R. Bruce, M. Jebramcik, J. Jowett, T. Mertens, and M. Schaumann. Performance and luminosity models for heavy-ion operation at the CERN Large Hadron Collider. *Eur. Phys. J. Plus*, 136:745, 2021. doi: 10.1140/epjp/s13360-021-01685-5. URL `https://doi.org/10.1140/epjp/s13360-021-01685-5`.

[26] O. S. Brüning, P. Collier, P. Lebrun, S. Myers, R. Ostojic, J. Poole, and P. Proudlock

(editors). LHC design report v.1 : The LHC main ring. *CERN-2004-003-V1*, CERN, Geneva, Switzerland, 2004.

[27] C. Tambasco *et al.* Improved physics model for collimation tracking studies at LHC. *Paper in preparation*, 2014.

[28] A. Ciccotelli et al. Fluka simulations of power load from BFPP in IR8. *Presentation at the LHC Collimation Working Group #266*, July 2022. URL https://indico.cern.ch/event/1178687/contributions/4951444/attachments/2477388/4252150/BFPP_collimation_WG_8july.pdf.

[29] Z. Citron et al. Report from Working Group 5: Future physics opportunities for high-density QCD at the LHC with heavy-ion and proton beams. page 207 p, Dec 2018. doi: 10.23731/CYRM-2019-007.1159. URL https://cds.cern.ch/record/2650176.

[30] CMS Collaboration. The CMS experiment at the CERN LHC. *JINST*, 3:S08004, 2008.

[31] A. collaboration. Observation of a new particle in the search for the standard model higgs boson with the ATLAS detector at the LHC. *Physics Letters B*, 716(1):1 – 29, 2012. ISSN 0370-2693. doi: http://dx.doi.org/10.1016/j.physletb.2012.08.020. URL http://www.sciencedirect.com/science/article/pii/S037026931200857X.

[32] J. Coupard, H. Damerau, A. Funken, R. Garoby, S. Gilardoni, B. Goddard, K. Hanke, D. Manglunki, M. Meddahi, G. Rumolo, R. Scrivens, and E. Chapochnikova. LHC Injectors Upgrade, Technical Design Report, Vol. II: Ions. Technical Report CERN-ACC-2016-0041, CERN, Geneva, Apr 2016. URL https://cds.cern.ch/record/2153863.

[33] E. B. Holzer *et al*. Development, production and testing of 4500 beam loss monitors. *Proc. of the European Particle Accelerator Conf. 2008, Genoa, Italy*, page 1134, 2008.

[34] L. Evans. *The Large Hadron Collider: A Marvel of Technology*. Fundamental sciences. Taylor & Francis Group, 2009. ISBN 9782940222346. URL https://books.google.ch/books?id=tl8fLB1viQcC.

[35] F. Bordry *et al.* The First Long Shutdown (LS1) for the LHC. *Proceedings of the International Particle Accelerator Conference 2013, Shanghai, China*, page 44, 2013.

[36] A. Ferrari, P. Sala, A. Fassò, and J. Ranft. FLUKA: a multi-particle transport code. *CERN Report CERN-2005-10*, 2005.

[37] G. Battistoni *et al.* The Application of the Monte Carlo Code FLUKA in Radiation Protection Studies for the Large Hadron Collider. *Progress in Nuclear Science and Technology*, 2:358, 2011.

[38] E. Holzer, B. Dehning, E. Effinger, J. Emery, G. Ferioli, J. Gonzalez, E. Gschwendtner, G. Guaglio, M. Hodgson, D. Kramer, R. Leitner, L. Ponce, V. Prieto, M. Stockner, and C. Zamantzas. Beam Loss Monitoring System for the LHC. *IEEE Nuclear Science Symposium Conference Record*, 2:1052, 2005. doi: 10.1109/NSSMIC.2005.1596433.

[39] J.M. Jowett *et al.* Overview of ion runs during Run 2. *Proceedings of the 9th LHC Operations Evian Workshop, Evian, France*, 2019. URL `https://indico.cern.ch/event/751857/timetable/#20190130.detailed`.

[40] J. Jowett. Colliding Heavy Ions in the LHC. page TUXGBD2, 2018. doi: 10.18429/JACoW-IPAC2018-TUXGBD2. URL `https://cds.cern.ch/record/2648704`.

[41] J. Jowett, G. Arduini, R. Assmann, P. Baudrenghien, C. Carli, M. Lamont, M. S. Camillocci, J. Uythoven, W. Venturini, and J. Wenninger. First run of the LHC as a heavy-ion collider. *Proceedings of IPAC11, San Sebastian, Spain*, page 1837, 2011. URL `http://accelconf.web.cern.ch/AccelConf/IPAC2011/papers/tupz016.pdf`.

[42] J. Jowett, R. Alemany-Fernandez, P. Baudrenghien, D. Jacquet, M. Lamont, D. Manglunki, S. Redaelli, M. Sapinski, M. Schaumann, M. S. Camillocci, R. Tomas, J. Uythoven, D. Valuch, R. Versteegen, and J. Wenninger. Proton-nucleus Collisions in the LHC. *Proceedings of IPAC13, Shanghai, China*, page 49, 2013. URL `https://cds.cern.ch/record/1572994?ln=en`.

[43] J. Jowett, R. Alemany-Fernandez, R. Bruce, M. Giovannozzi, P. Hermes, W. Höfle, M. Lamont, T. Mertens, S. Redaelli, M. Schaumann, J. Uythoven, and J. Wenninger. The 2015 Heavy-Ion Run of the LHC. *Proceedings of the International Particle Accelerator Conference 2016, Busan, Korea*, page 1493, 2016. URL `http://accelconf.web.cern.ch/AccelConf/ipac2016/papers/tupmw027.pdf`.

[44] J. Jowett, M. Schaumann, B. Auchmann, C. B. Castro, M. Kalliokoski, A. Lechner, T. Mertens, and C. Xu. Bound-free pair production in LHC Pb-Pb operation at 6.37 Z TeV per beam. *Proceedings of the International Particle Accelerator Conference 2016, Busan, Korea*, page 1497, 2016. URL `https://cds.cern.ch/record/2207380?ln=en`.

[45] J. Jowett, R. Alemany-Fernandez, G. Baud, P. Baudrenghien, R. D. Maria,

D. Jacquet, M. Jebramcik, T. Lefevre, A. Mereghetti, T. Mertens, M. Schaumann, H. Timko, M. Wendt, and J. Wenninger. the 2016 proton-nucleus run of the LHC. *Proceedings of the International Particle Accelerator Conference 2017, Copenhagen, Denmark*, page 2071, 2017. URL `http://accelconf.web.cern.ch/AccelConf/ipac2017/papers/tupva014.pdf`.

[46] J. Jowett, C. B. Castro, W. Bartmann, C. Bracco, R. Bruce, J. Dilly, S. Fartoukh, A. Garcia-Tabares, M. Hofer, M. Jebramcik, J. Keintzel, A. Lechner, E. Maclean, L. Malina, T. Medvedeva, D. Mirarchi, T. Persson, B. Petersen, S. Redaelli, M. Schaumann, M. Solfaroli, R. Tomas, J. Wenninger, J. Coello, E. Fol, N. Fuster-Martinez, E. Holzer, A. Mereghetti, B. Salvachua, C. Schwick, M. Spitznagel, H. Timko, A. Wegscheider, and D. Wollmann. The 2018 Heavy-Ion Run of the LHC. *Proceedings of the 10th International Particle Accelerator Conference (IPAC2019): Melbourne, Australia, May 19-24, 2019*, page 2258, 2019. doi: https://doi.org/10.18429/JACoW-IPAC2019-WEYYPLM2.

[47] J. Jowett et al. The 2018 heavy-ion run of the LHC. page WEYYPLM2, 2019. doi: 10.18429/JACoW-IPAC2019-WEYYPLM2. URL `https://cds.cern.ch/record/2693921`.

[48] J. M. Jowett and C. Carli. The LHC as a proton-nucleus collider. *Proc. of the European Particle Accelerator Conf. 2006, Edinburgh, Scotland*, page 550, 2006.

[49] J. M. Jowett, H. H. Braun, M. I. Gresham, E. Mahner, A. N. Nicholson, and E. Shaposhnikova. Limits to the Performance of the LHC with Ion Beams. *Proc. of the European Particle Accelerator Conf. 2004, Lucerne*, page 578, 2004.

[50] V. Kain. Beam dynamics and beam losses – circular machines. *CERN Yellow Reports*, page Vol 2 (2016): Proceedings of the 2014 Joint International Accelerator School: Beam Loss and Accelerator Protection, 2016. doi: 10.5170/CERN-2016-002.21. URL `https://e-publishing.cern.ch/index.php/CYR/article/view/228`.

[51] A. Lechner, M. Albert, B. Auchmann, C. B. Castro, L. Grob, E. B. Holzer, J. Jowett, M. Kalliokoski, S. L. Naour, A. Lunt, A. Mereghetti, G. Papotti, R. Schmidt, R. Veness, A. Verweij, G. Willering, D. Wollmann, C. Xu, and M. Zerlauth. BLM Thresholds and UFOs. pages 209–214. 6 p, 2017. URL `https://cds.cern.ch/record/2293680`.

[52] S. Y. Lee. *Accelerator Physics*. World Scientific, 1999.

[53] M.A.Jebramcik. *Beam Dynamics of Proton-Nucleus Collisions in the Large Hadron*

Collider. PhD thesis, Johann Wolfgang Goethe-Universität, Frankfurt am Main, Germany, 2019.

[54] D. Manglunki, M. Angoletta, H. Bartosik, G. Bellodi, A. Blas, T. Bohl, C. Carli, E. Carlier, S. Cave, K. Cornelis, H. Damerau, and I. Efthymiopoulos. Performance of the cern heavy ion production complex. 01 2012.

[55] M. Martini. An introduction to transverse beam dynamics in accelerators. *CERN/PS 96-11*, 1996.

[56] A. Mereghetti. *Performance Evaluation of the SPS Scraping System in View of the High Luminosity LHC*. PhD thesis, University of Manchester, 2015.

[57] A. Mereghetti, V. Boccone, F. Cerutti, R. Versaci, and V. Vlachoudis. The Fluka Linebuilder and Element Database: Tools for Building Complex Models of Accelerators Beam Lines. *Proceedings of IPAC12, New Orleans, Louisiana, USA*, page 2687, 2012.

[58] S. Redaelli. Beam cleaning and collimation systems. *CERN Yellow Reports*, page Vol 2 (2016): Proceedings of the 2014 Joint International Accelerator School: Beam Loss and Accelerator Protection, 2016. doi: 10.5170/CERN-2016-002.403. URL `https://e-publishing.cern.ch/index.php/CYR/article/view/243`.

[59] G. Robert-Demolaize, R. Assmann, S. Redaelli, and F. Schmidt. A new version of sixtrack with collimation and aperture interface. *Proc. of the Particle Accelerator Conf. 2005, Knoxville*, page 4084, 2005.

[60] K. Røed, M. Brugger, D. Kramer, P. Peronnard, C. Pignard, G. Spiezia, and A. Thornton. Method for Measuring Mixed Field Radiation Levels Relevant for SEEs at the LHC. *IEEE Transactions on Nuclear Science*, 59:1040, 2012.

[61] S. Roesler, R. Engel, and J. Ranft. The Monte Carlo Event Generator DPMJET-III. *SLAC Report SLAC-PUB-8740*, 2000.

[62] S. R. Klein. Localized beampipe heating due to e- capture and nuclear excitation in heavy ion colliders. *Nucl. Inst. & Methods A*, 459:51, 2001.

[63] M. Schaumann, R. Alemany, B. Auchmann, C. B. Castro, V. Chetvertkova, R. Giachino, J. Jowett, M. Kalliokoski, A. Lechner, T. Mertens, and L. Ponce. LHC BFPP Quench Test with Ions (2015). *CERN-ACC-NOTE-2016-0024*, 2016. URL `https://cds.cern.ch/record/2127951?ln=en`.

[64] M. Schaumann, J. M. Jowett, C. Bahamonde Castro, R. Bruce, A. Lechner, and

T. Mertens. Bound-free pair production from nuclear collisions and the steady-state quench limit of the main dipole magnets of the CERN Large Hadron Collider. *Phys. Rev. Accel. Beams*, 23:121003, Dec 2020. doi: 10.1103/PhysRevAccelBeams.23.121003. URL https://link.aps.org/doi/10.1103/PhysRevAccelBeams.23.121003.

[65] F. Schmidt. SixTrack. User's Reference Manual. *CERN/SL/94-56-AP, CERN, Geneva, Switzerland*, 1994.

[66] E. Skordis, V. Vlachoudis, R. Bruce, F. Cerutti, A. Ferrari, A. Lechner, A. Mereghetti, P. Ortega, S. Redaelli, and D. S. Pastor. FLUKA coupling to Sixtrack. *CERN-2018-011-CP, Proceedings of the ICFA Mini-Workshop on Tracking for Collimation, CERN, Geneva, Switzerland*, page 17, 2018. URL https://cds.cern.ch/record/2646800?ln=en.

[67] C. Tambasco. An improved scattering routine for collimation tracking studies at LHC. Master's thesis, Università di Roma, Italy, 2014.

[68] T. Trenkler and J. Jeanneret. K2, a software package evaluating collimation systems in circular colliders (manual). *CERN SL/94105 (AP)*, 1994.

[69] V. Vlachoudis. FLAIR: a powerful but user friendly graphical interface for FLUKA. *Proc. Int. Conf. on Mathematics, Computational Methods and Reactor Physics (MC 2009), Saratoga Springs, New York*, 2009. URL http://www.fluka.org/flair/.

[70] R. Versteegen, R. Bruce, J. Jowett, A. Langner, Y. Levinsen, E. Maclean, M. McAteer, S. Redaelli, B. Salvachua, P. Skowronski, M. S. Camillocci, R. Tomas, G. Valentino, J. Wenninger, T. Persson, and S. White. Operating the LHC Off-momentum for p-Pb Collisions. *Proceedings of IPAC13, Shanghai, China*, 2013. URL http://accelconf.web.cern.ch/AccelConf/IPAC2013/papers/tupfi041.pdf.

[71] J. Wenninger. Operation and Configuration of the LHC in Run 2. *CERN-ACC-NOTE-2019-0007*, Mar 2019. URL http://cds.cern.ch/record/2668326.

[72] H. Wiedemann. *Particle Accelerator Physics.* Springer, third edition, 2007.

[73] K. Wille and J. McFall. *The Physics of Particle Accelerators: An Introduction.* Oxford University Press, 2000. ISBN 9780198505501. URL https://books.google.ch/books?id=dFILtAEACAAJ.

A | Appendix A

This appendix contains detailed comparisons of simulated and measured losses around IP2, IP5 and IP8 for 2018 Pb-Pb run. The simulation setup is discussed in Sec. 4.3.

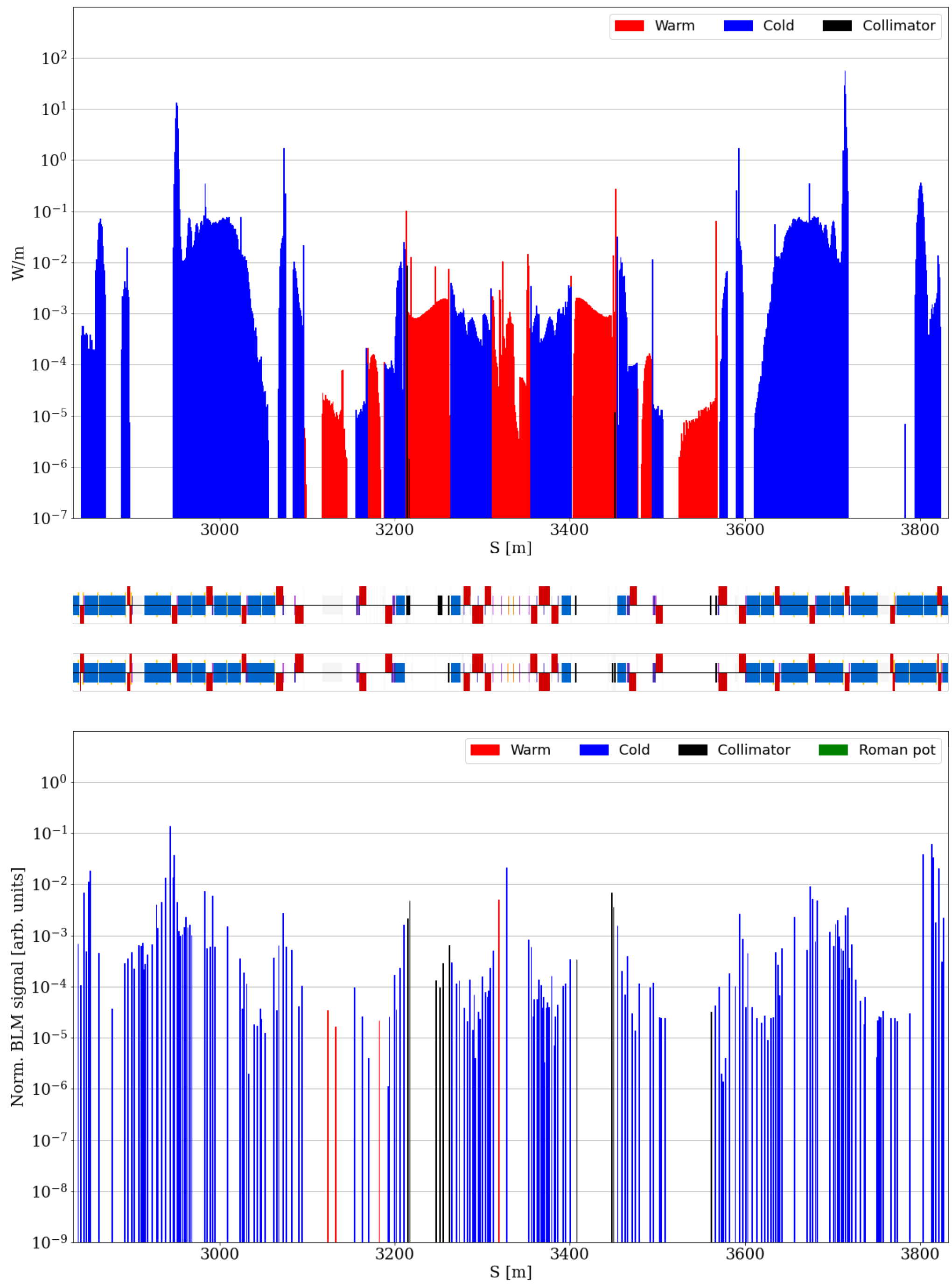

Figure A.1: Comparison between simulated (top) and measured (bottom) 2018 Pb-Pb collisional losses around IP2. The measured lossmap reports the normalized BLM signals (originally in Gy/s). A schematic of the lattices for B1 and B2 is shown in between the lossmaps.

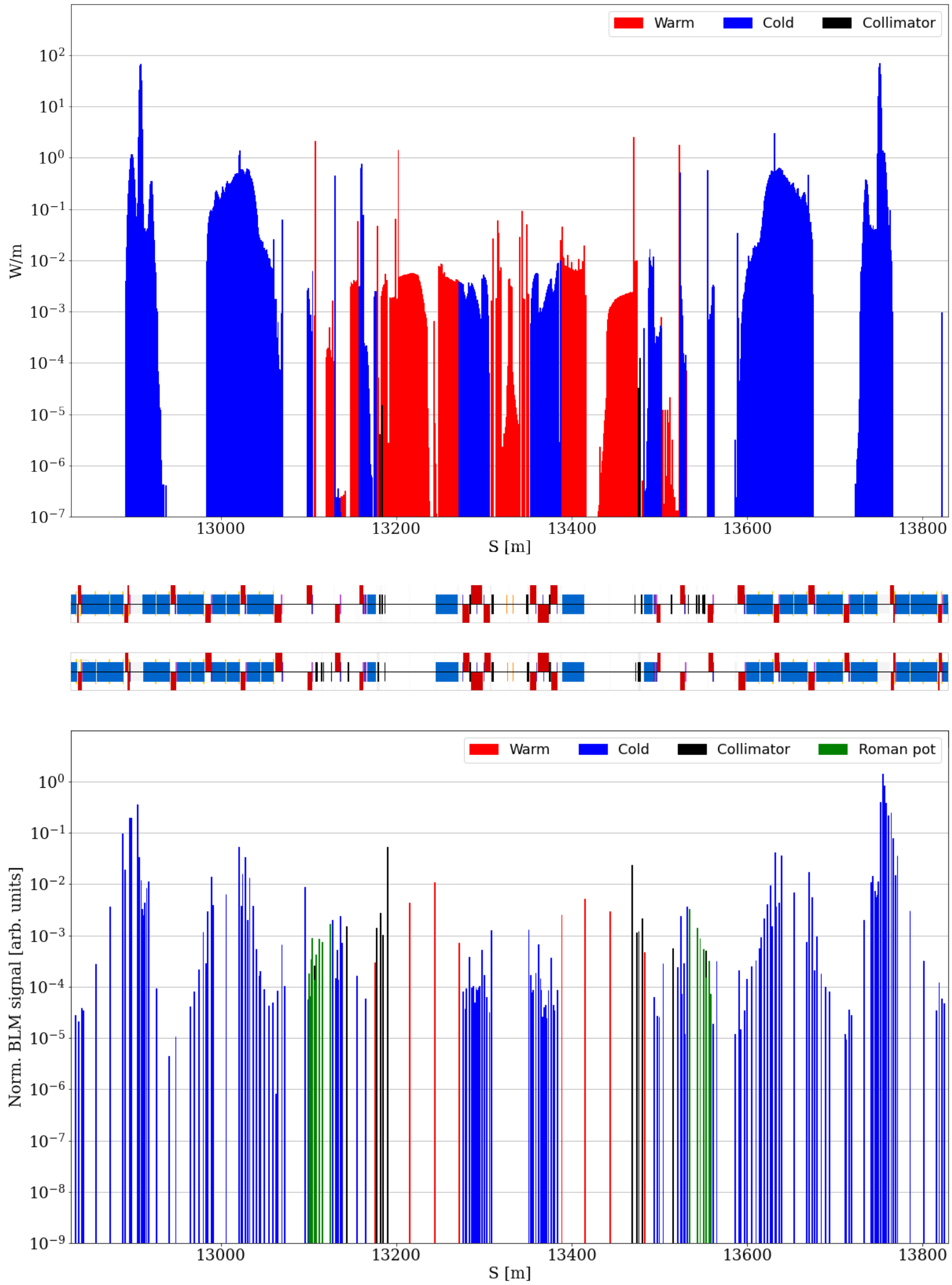

Figure A.2: Comparison between simulated (top) and measured (bottom) 2018 Pb-Pb collisional losses around IP5. The measured lossmap reports the normalized BLM signals (originally in Gy/s). A schematic of the lattices for B1 and B2 is shown in between the lossmaps.

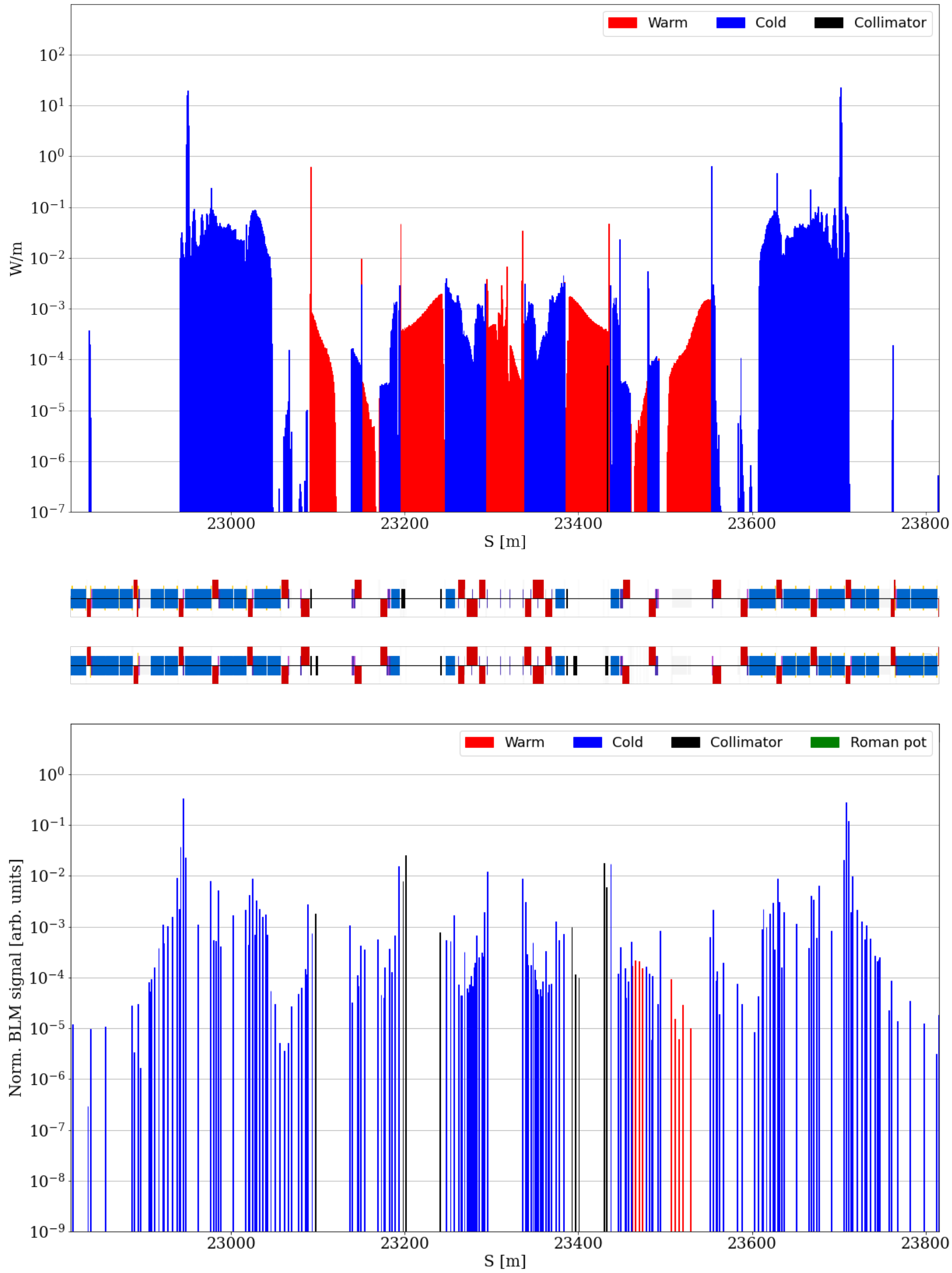

Figure A.3: Comparison between simulated (top) and measured (bottom) 2018 Pb-Pb collisional losses around IP8. The measured lossmap reports the normalized BLM signals (originally in Gy/s). A schematic of the lattices for B1 and B2 is shown in between the lossmaps.

B | Appendix B

This appendix contains the distributions related to the Pb beam products from p-Pb collisions simulated in IP1, as well as the losses they give rise to. The simulation setup is discussed in Sec. 5.1.

B.1. EMD

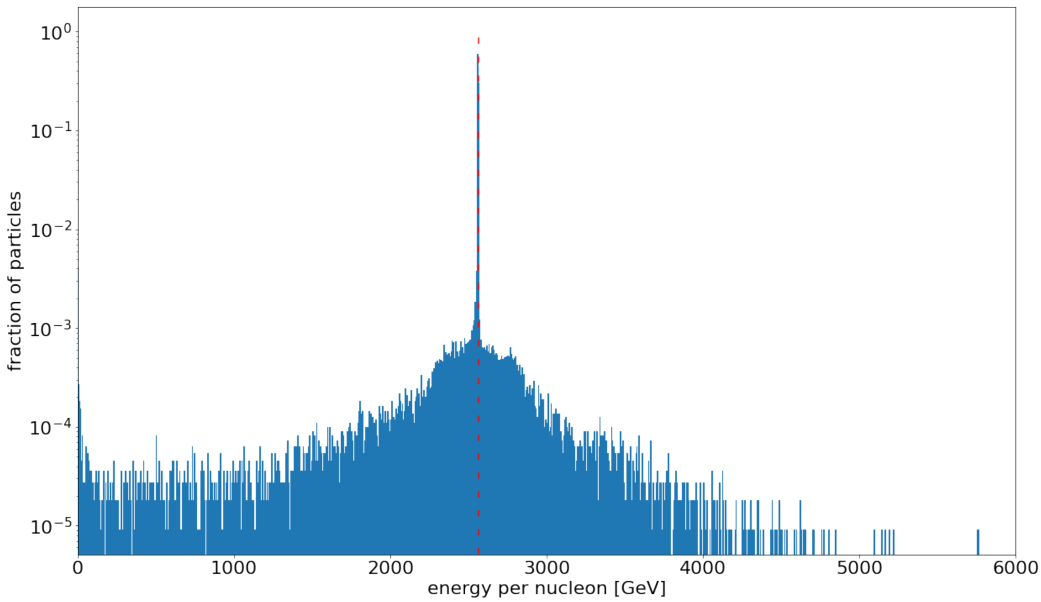

Figure B.1: Distributions of energy per nucleon for EMD products from p-Pb collisions simulated with 6.5 Z TeV beam energy. The interactions have been simulated by FLUKA DMPJET3 event generator.

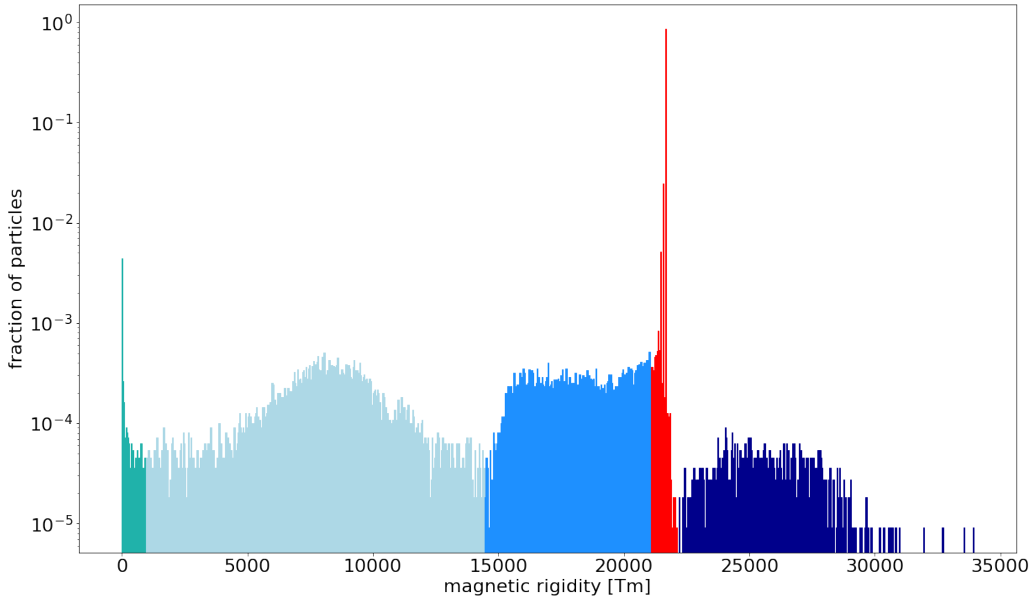

(a) Distribution of magnetic rigidity. The portion in red indicates a range around the original magnetic rigidity of 21681.66±500 Tm.

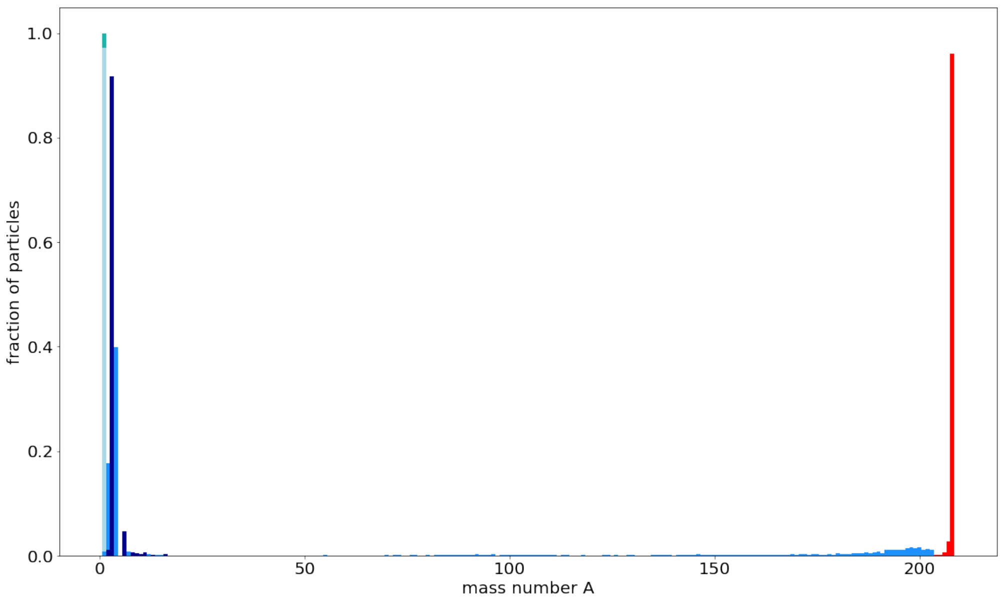

(b) Distribution of nuclide mass number for each portion of the magnetic rigidity distribution.

Figure B.2: Distributions of magnetic rigidity (a) and contributing-particle mass number (b) for EMD products from p-Pb collisions simulated with 6.5 Z TeV beam energy. The interactions have been simulated by FLUKA DMPJET3 event generator.

B.2. Inelastic interactions

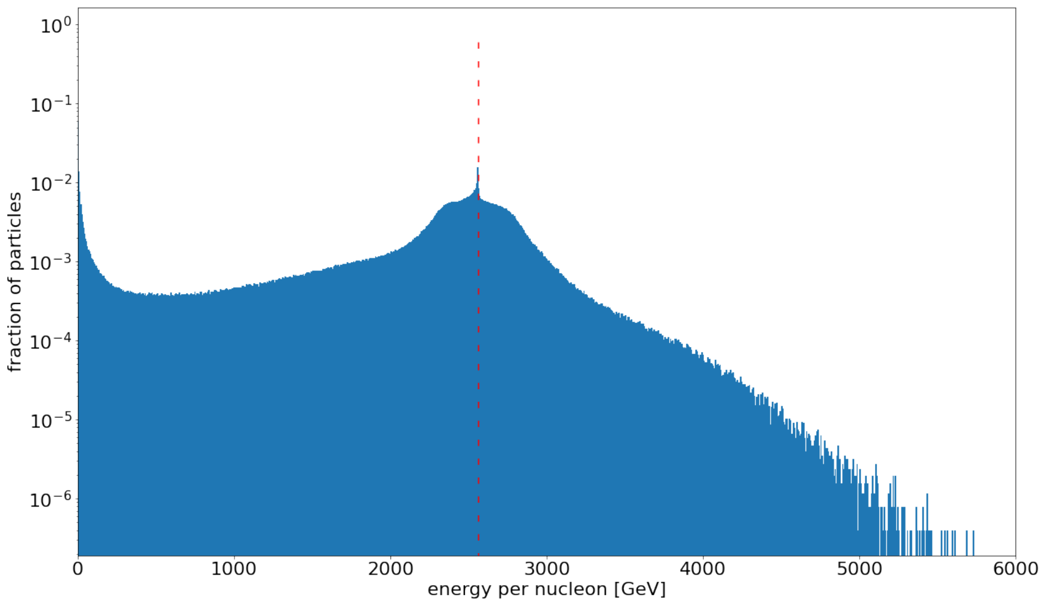

Figure B.3: Distributions of energy per nucleon for inelastic interaction products from p-Pb collisions simulated with 6.5 Z TeV beam energy. The interactions have been simulated by FLUKA DMPJET3 event generator.

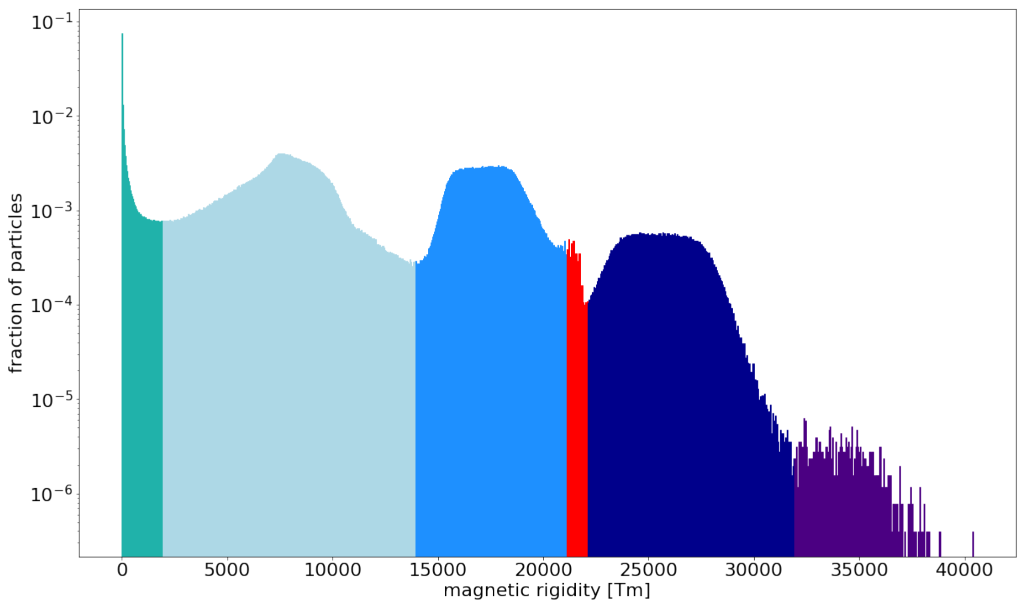

(a) Distribution of magnetic rigidity. The portion in red indicates a range around the original magnetic rigidity of 21681.66±500 Tm.

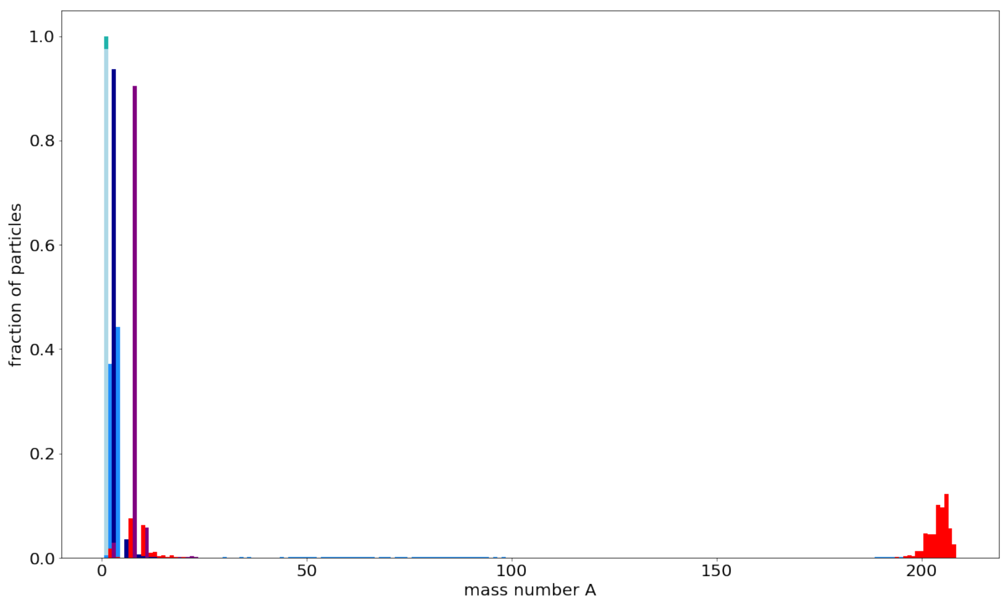

(b) Distribution of nuclide mass number for each portion of the magnetic rigidity distribution.

Figure B.4: Distributions of magnetic rigidity (a) and contributing-particle mass number (b) for inelastic interaction products from p-Pb collisions simulated with 6.5 Z TeV beam energy. The interactions have been simulated by FLUKA DMPJET3 event generator.

B.3. Losses

This appendix section contains three zooms of the lossmap in Fig. 5.6, on IP1 right side and at the beginning of the two cleaning regions, together with a colour code displaying the contributions from the different particles to the respective losses. Each loss bar has been coloured proportionally to the fraction of ions lost in the corresponding bin, using a different colour for each of the main nuclides (the logarithmic scale in the y-scale does not apply to these fractional losses).

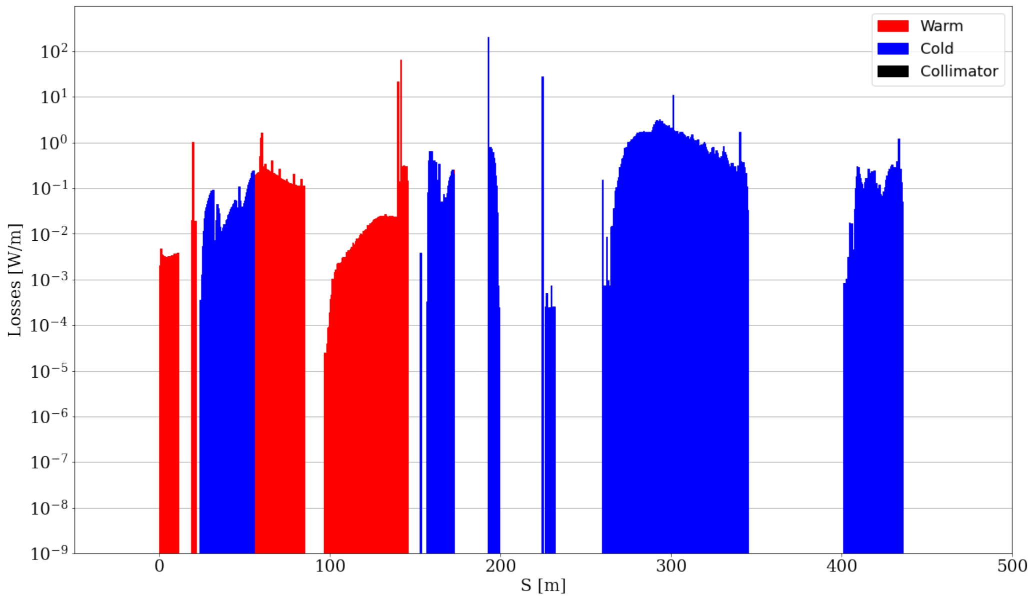

(a) Zoom on IP1 right side.

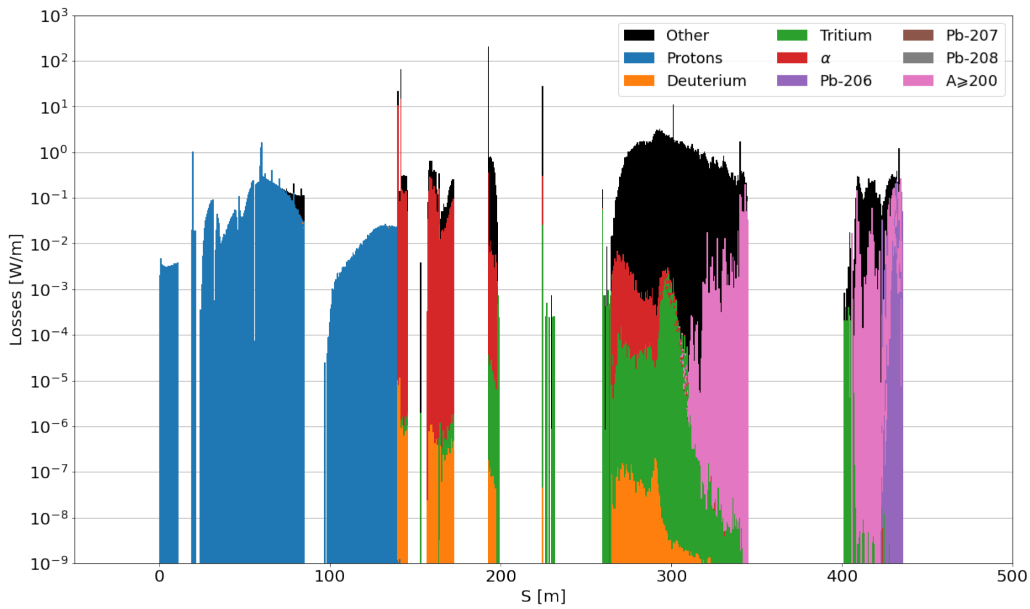

(b) Contribution from main ions to losses.

Figure B.5: Zoom of the lossmap in Fig. 5.6 on the right side of IP1 (a) and mask showing the contribution from main nuclides (b). The contributions are shown in terms of fractional number of particle lost in a bin (the logarithmic scale in the y-scale does not apply to these fractional losses).

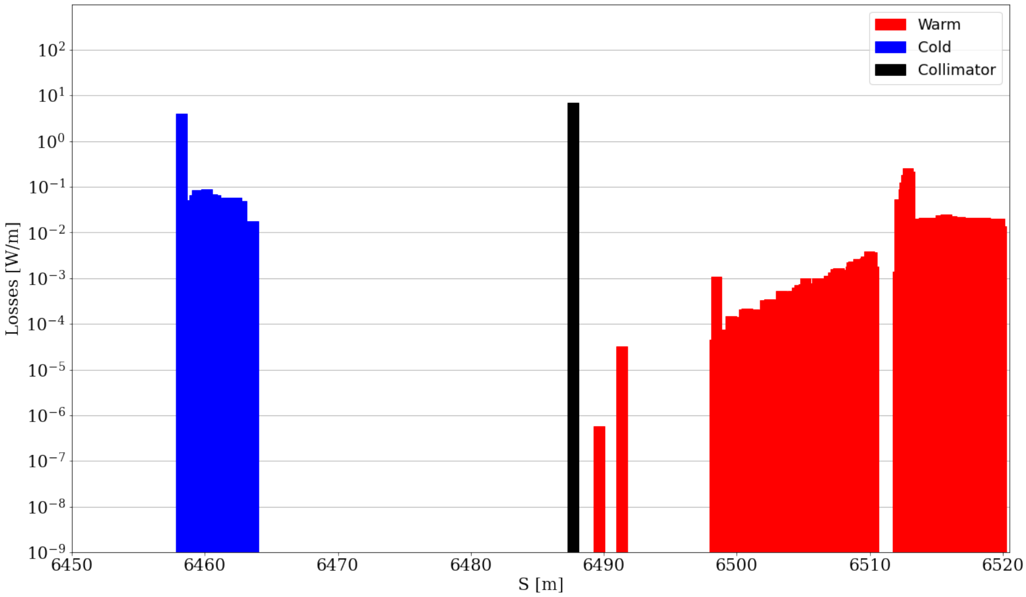

(a) Zoom at the beginning of IR3.

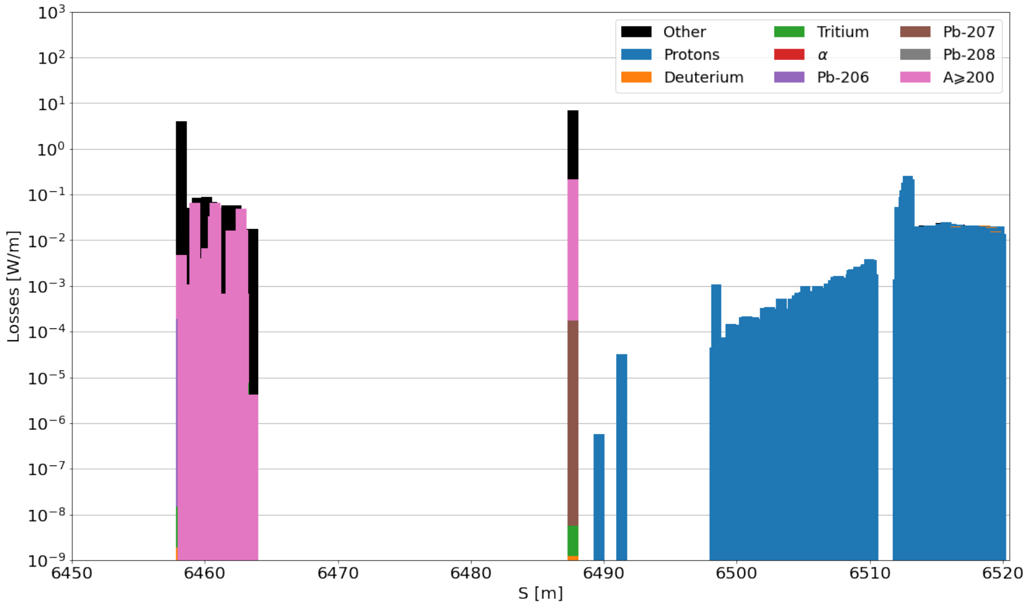

(b) Contribution from main ions to losses.

Figure B.6: Zoom of the lossmap in Fig. 5.6 at the beginning of IR3 (a) and mask showing the contribution from main nuclides (b). The contributions are shown in terms of fractional number of particle lost in a bin (the logarithmic scale in the y-scale does not apply to these fractional losses).

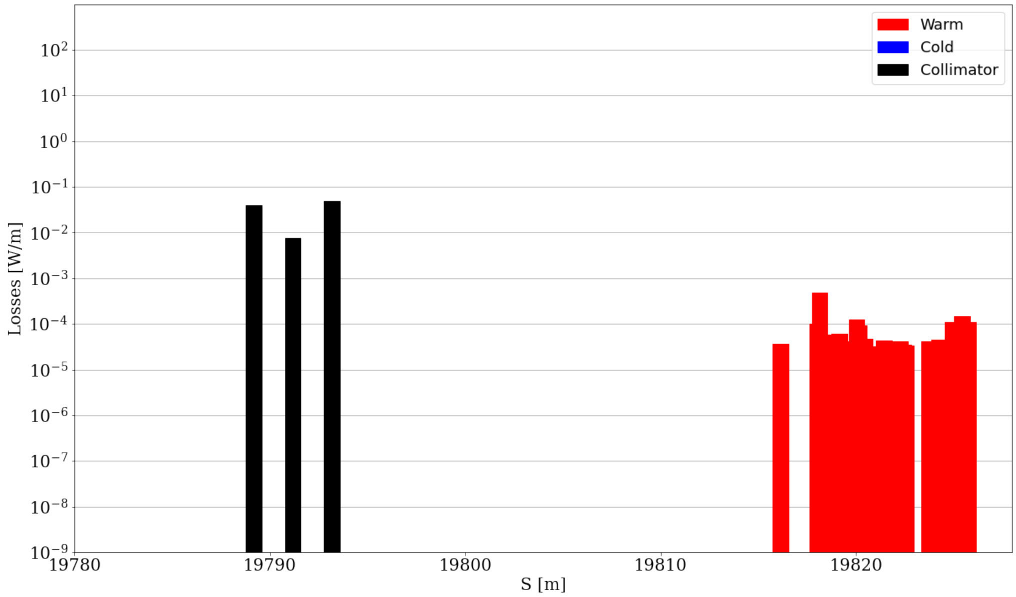

(a) Zoom at the beginning of IR7.

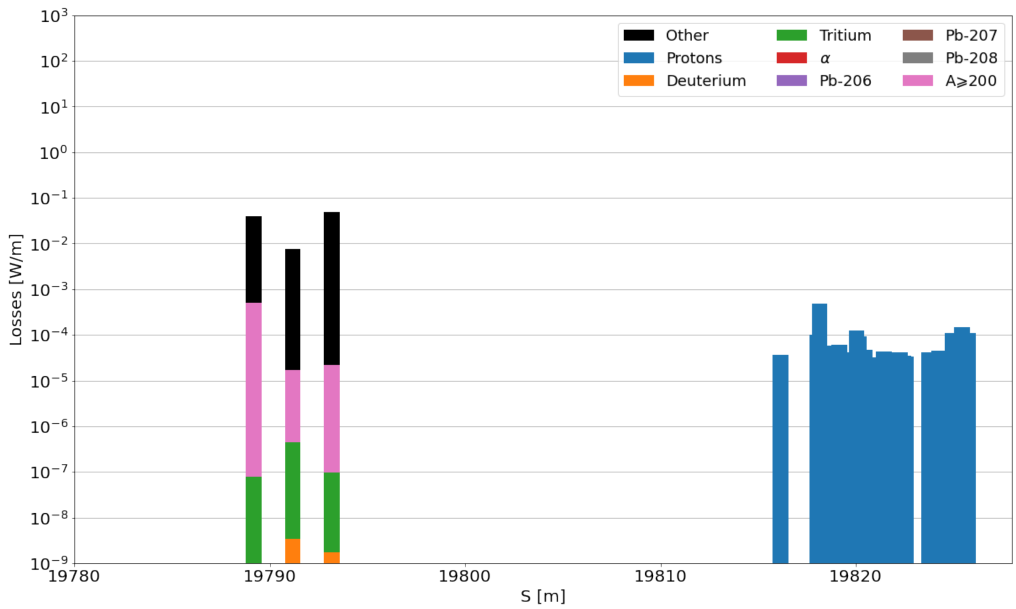

(b) Contribution from main ions to losses.

Figure B.7: Zoom of the lossmap in Fig. 5.6 at the beginning of IR7 (a) and mask showing the contribution from main nuclides (b). The contributions are shown in terms of fractional number of particle lost in a bin (the logarithmic scale in the y-scale does not apply to these fractional losses).

C | Appendix C

This appendix contains detailed comparisons of simulated and measured losses around IP2, IP5 and IP8 for 2016 p-Pb run. The simulation setup is discussed in Sec. 5.2.

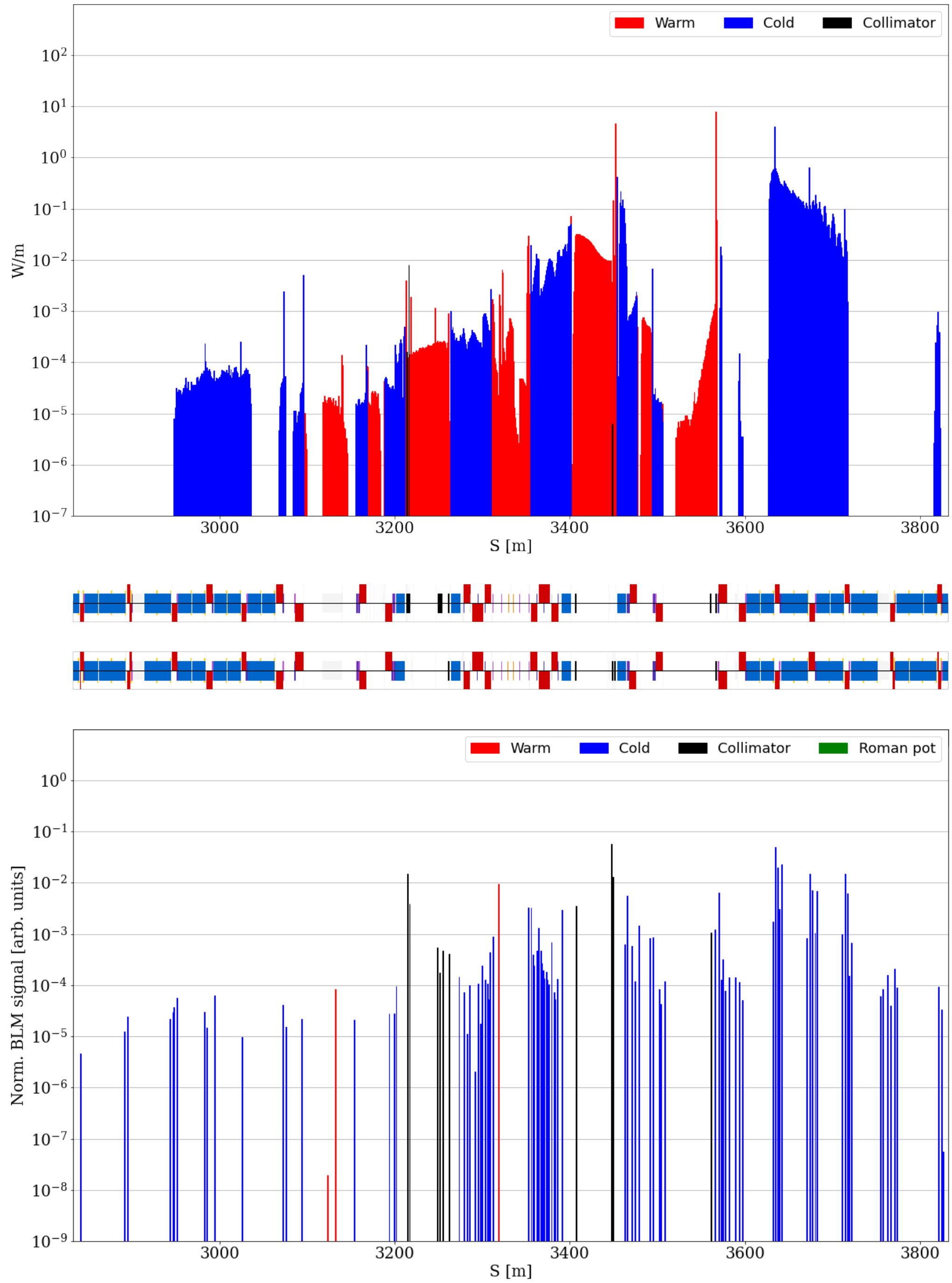

Figure C.1: Comparison between simulated (top) and measured (bottom) 2016 p-Pb collisional losses around IP2. The measured lossmap reports the normalized BLM signals (originally in Gy/s). A schematic of the lattices for B1 and B2 is shown in between the lossmaps.

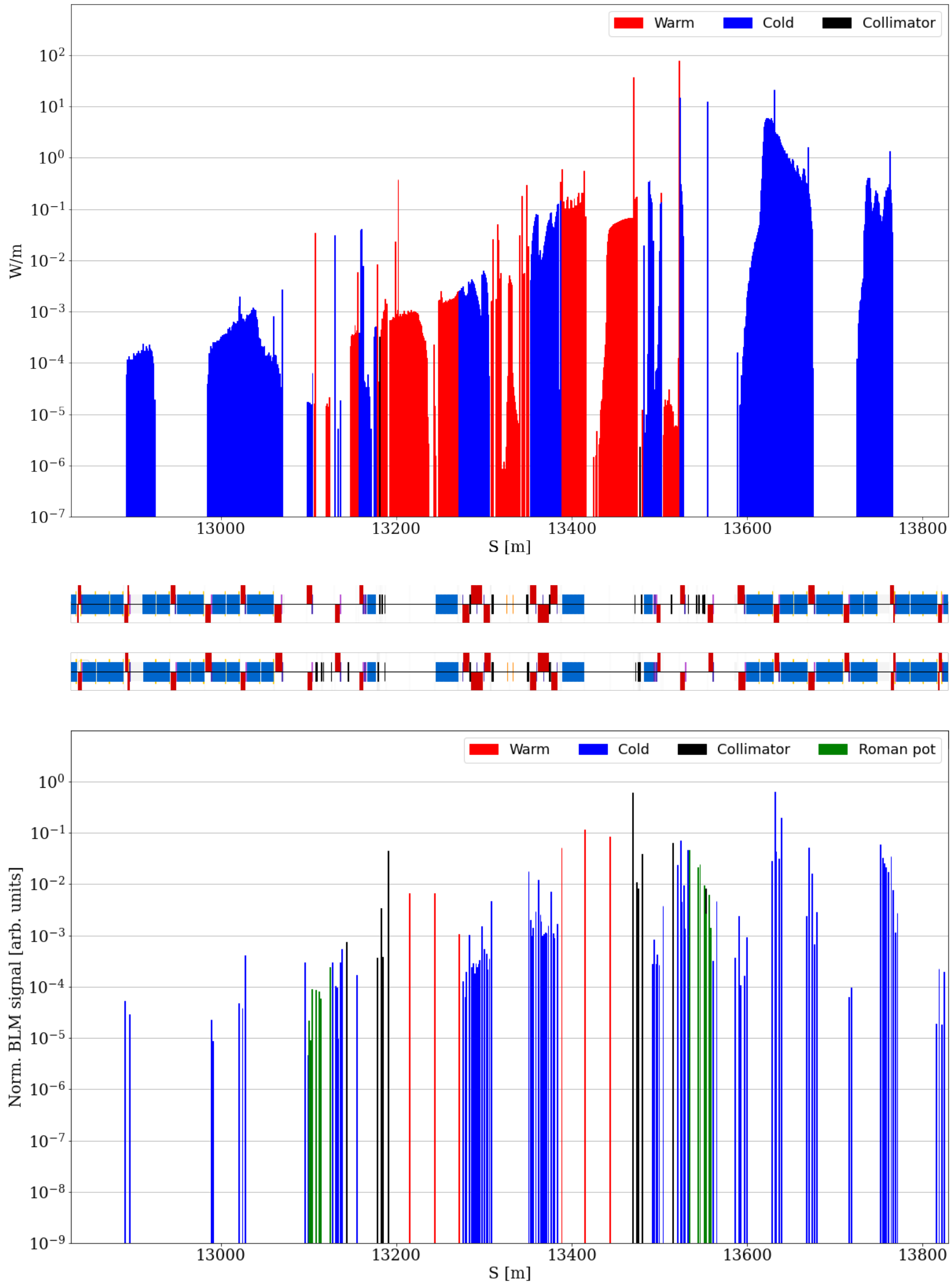

Figure C.2: Comparison between simulated (top) and measured (bottom) 2016 p-Pb collisional losses around IP5. The measured lossmap reports the normalized BLM signals (originally in Gy/s). A schematic of the lattices for B1 and B2 is shown in between the lossmaps.

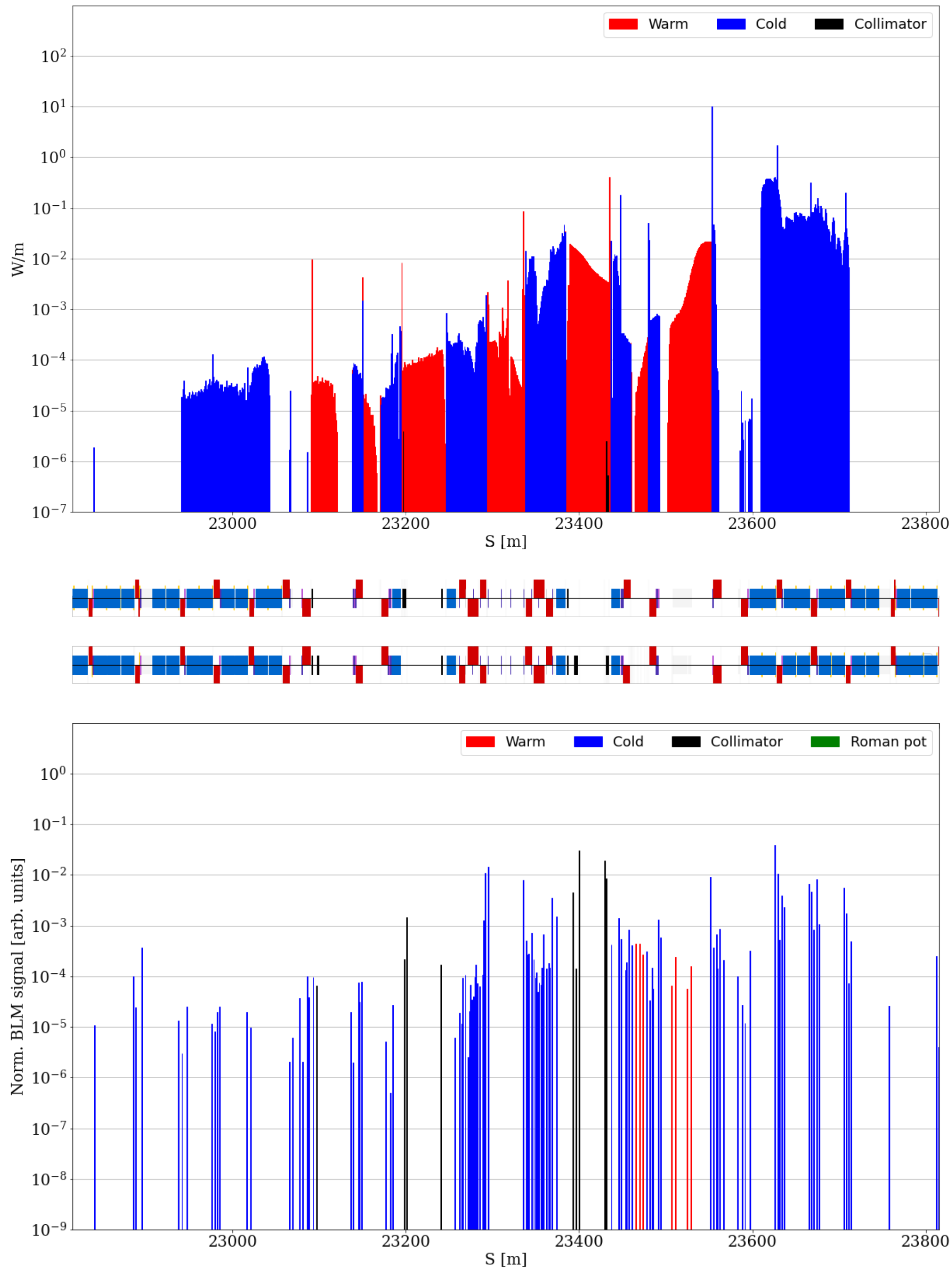

Figure C.3: Comparison between simulated (top) and measured (bottom) 2016 p-Pb collisional losses around IP8. The measured lossmap reports the normalized BLM signals (originally in Gy/s). A schematic of the lattices for B1 and B2 is shown in between the lossmaps.

List of Figures

List of Tables

List of Symbols

Variable	Description	SI unit
$\boldsymbol{A}$	mass number	–
$\boldsymbol{Z}$	atomic number	–
$\boldsymbol{m}$	particle mass	kg
$\boldsymbol{q}$	particle charge	C
$\boldsymbol{p}$	particle momentum	kg m s^{-1}
$\boldsymbol{E}$	particle energy	J
$\boldsymbol{B}$	magnetic field	T
$\boldsymbol{c}$	speed of light	m s^{-1}
$\boldsymbol{\sigma_{event}}$	event cross section	m^2
$\boldsymbol{\mathcal{L}}$	luminosity	m^{-2} s^{-1}
$\boldsymbol{\rho}$	radius of curvature	m
$\boldsymbol{R}$	average orbit radius	m
$\boldsymbol{C}$	orbit circumference	m
$\boldsymbol{s}$	orbit longitudinal coordinate	m
$\boldsymbol{x}$	particle horizontal coordinate	m
$\boldsymbol{x'}$	particle horizontal angle	rad
$\boldsymbol{y}$	particle vertical coordinate	m
$\boldsymbol{y'}$	particle vertical angle	rad
$\boldsymbol{\delta}$	fractional momentum offset	–
$\boldsymbol{\beta}$	betatron function	m
$\boldsymbol{\beta^*}$	betatron function at the IP	m
$\boldsymbol{Q}$	betatron tune	–
$\boldsymbol{D}$	dispersion	m
$\boldsymbol{\epsilon}$	emittance	m
$\boldsymbol{\epsilon_n}$	normalized emittance	m

$\boldsymbol{\sigma}$	transverse beam envelope	m
$\boldsymbol{V}$	RF accelerating voltage	kg m^2 A^{-1} s^{-3}
$\boldsymbol{f_{RF}}$	RF frequency	s^{-1}
$\boldsymbol{f_{rev}}$	revolution frequency	s^{-1}
$\boldsymbol{h}$	harmonic number	–
$\boldsymbol{\alpha_c}$	momentum compaction factor	–
$\boldsymbol{\eta}$	slip factor	–
$\boldsymbol{\eta_c}$	cleaning inefficiency	–
$\boldsymbol{\tilde{\eta}_c}$	local cleaning inefficiency	m^{-1}

Acknowledgements

Before starting to thank all the people who helped me in this journey and without whom this would not have been possible, I apologize for falling into the temptation to use Italian here and there.

Thank you Roderik, I knew from the very first time I met you that you are not only a great supervisor, but a great person. Your big mind and your dedication deserve most of the merit of this work. I really hope the next supervisors I will meet will have as much professionalism, efficiency and kindness as you. For sure our collaboration did not end here!

A big thank you to all the guys from the best section of CERN, the collimation section. Andrey, Bjorn, Frederik, Pascal, Maria, Marco, you were always there when I needed technical support, ready to help me as soon as possible. Many thanks to Stefano, who runs this amazing section arranging from time to time important meetings to drink a sip of grappa.

Un sentito ringraziamento a chi la grappa l'ha portata. Grazie Filippo, non dimenticherò mai quel pomeriggio passato insieme ad implementare su Python la funzione che ha generato i migliori plot di questo lavoro. Vecchio, grazie davvero per la completa disponibilità. Ci vediamo a Bassano!

Coffee had an important role as well, so many thanks to the young force who shared with me many cups of coffee everyday, Enrico, Phani and Despina. Despina, you won the award for the only CERN person who came along with me to skateboard.

Grazie mille al professor Marco Beghi per aver accettato di seguire il mio lavoro dal Politecnico di Milano. Un grande grazie anche a chi mi ha indicato la via insegnandomi le basi, il professor Lucio Rossi.

Many thanks to Luigi and Francesco from the FLUKA team, who always assisted me in my simulations.

I ringraziamenti che seguono sono invece più intimi, e non sono che un lieve riflesso del vero riconoscimento che queste persone meritano.

Grazie a mio fratello Fabrizio, il mio orgoglio e la mia casa in giro per il mondo. Ti ringrazio e ti ammiro per aver tracciato sempre il cammino di fronte a me. Insieme faremo grandi cose.
Un ringraziamento speciale a voi che avete sempre saputo tutto e non avete mai esitato di me, grazie mamma e papà. Siete la mia casa fissa che non mi ha fatto mai mancare un sostegno solido.
Grazie a chi è stata casa qui, durante questo anno difficile. Francesca, hai portato il sole in questo posto nuvoloso e non hai smesso di splendere neanche nei miei momenti più bui. Grazie compagna di viaggio (e di tutto il resto)!
Nonna Maria, ti porterò la tesi e ti farò sorridere, perché anche tu mi hai aiutato settimana dopo settimana, grazie.
Bisogna anche ringraziare i miei grandi amici di una vita per stare aspettando una festa di laurea ormai da anni. Gabri e Pietro, vi ringrazio per avermi fatto ridere tutti i giorni anche a centinaia di chilometri di distanza, vi meritate la festa più bella del mondo.
E infine grazie a tutti i ragazzi di Camp1us Lambrate per gli anni che hanno preceduto questa esperienza. Con le innumerevoli occasioni di festa (quotidiane), mi avete dato la carica per affrontare tutto ciò. Marcolino, grazie a te in particolare, sarebbe stato davvero bello condividere una doppia con te qui a Saint-Genis. Aspetto che mi porti alle Olimpiadi!

Thank you all from the bottom of my heart!